Kasahara, J., Stephen, R.A., Acton, G.D., and Frey, F.A. (Eds.)
*Proceedings of the Ocean Drilling Program, Scientific Results* Volume 200

# 5. Data Report: Broadband Seismic Observations at the Hawaii-2 Observatory, ODP Leg 200[1]

R.A. Stephen,[2] F.K. Duennebier,[3] D. Harris,[3] J. Jolly,[3] S.T. Bolmer,[2] and P.D. Bromirski[4]

## INTRODUCTION

Leg 200 was the first leg in deep sea and ocean drilling history to conduct operations in the vicinity of a continuously operating broadband seafloor seismometer (Stephen, Kasahara, Acton, et al., 2003). In September 1998, scientists from the University of Hawaii installed a broadband, shallow buried seismometer at the Hawaii-2 Observatory (H2O) site (Duennebier et al., 2002), and data continued to be acquired in real time in Oahu over the Hawaii-2 transoceanic cable until May 2003. Noise from the *JOIDES Resolution* as it approached and left the site as well as that from on-site operations was acquired continuously in Oahu in real time. In addition, shots from the 80-in$^3$ water guns during single-channel seismic tests and the 1000-in$^3$ gun during vertical seismic profile tests were also recorded. The purpose of this data report is to display in a variety of formats all of the seismic data acquired at H2O during Leg 200 (16 December 2001 [Julian day (JD)350/2001] to 27 January 2002 [JD27/2002]). Although this is an arbitrary time interval, it is long enough to record activities typical of the site, including events such as T-phases from distant earthquakes, local earthquakes, whales, shipping, and all of the *JOIDES Resolution*–related activities, including the water gun shots. Recorded activities at the beginning and end of this interval give some idea of background seismic activity when the drillship is not on site.

A complete description of drillship operations at Site 1224 is given in the "Operations" section of the site chapter (Shipboard Scientific Party, 2003). Operations for Site 1224 started at 0900 Universal Time Coordi-

[1]Stephen, R.A., Duennebier, F.K., Harris, D., Jolly, J., Bolmer, S.T., and Bromirski, P.D., 2006. Data report: Broadband seismic observations at the Hawaii-2 observatory, ODP Leg 200. *In* Kasahara, J., Stephen, R.A., Acton, G.D., and Frey, F.A. (Eds.), *Proc. ODP, Sci. Results,* 200, 1–63 [Online]. Available from World Wide Web: <http://www-odp.tamu.edu/publications/200_SR/VOLUME/CHAPTERS/003.PDF>. [Cited YYYY-MM-DD]
[2]Department of Geology and Geophysics, Woods Hole Oceanographic Institution, 360 Woods Hole Road, Woods Hole MA 02543-1542, USA. Correspondence author: **rstephen@whoi.edu**
[3]Department of Geology and Geophysics, University of Hawaii, 2525 Correa Road, Honolulu Hawaii 96822, USA.
[4]Center for Coastal Studies, Scripps Institution of Oceanography, 9500 Gilman Drive, La Jolla California, 92093-0209 USA.

Initial receipt: 21 May 2004
Acceptance: 13 December 2005
Web publication: 26 June 2006
Ms 200SR-003

nated (UTC) on 26 December 2001 (JD360) when the drillship arrived at waypoint 1 (27°32.787′N, 142°33.036′W), ~36 nmi southwest of the H2O junction box (27°52.916′N, 141°59.504′W). (Note that all times in the Operations report are given in local ship time, which is UTC – 9 hr at Site 1224.) From waypoint 1, we approached H2O on a course of 56° at 6 kt while firing the water gun every 10 s as part of a seismic refraction survey (see "Seismic Results from Hawaii-2 Observatory" in the site chapter in Shipboard Scientific Party, 2003) (Fig. F1). The survey was completed at waypoint 2 (27°54.426′N, 141°56.985′W) at ~1645 UTC on 26 December, and the *JOIDES Resolution* returned and was positioned at Site 1224 (27°53.363′N, 141°58.758′W) at 1745 UTC on 26 December. At the site, drilling operations were interrupted six times, for a total of 6.11 days, while we waited on weather because of high seas (up to 7.7 m of heave) and strong winds (up to 44 kt). These storm periods correlate well with seismic noise in the microseism band as discussed by Bromirski et al. (2005). Site 1224 operations ended at 0930 UTC on 22 January 2002 (JD22), and the drillship departed the site on a bearing of 78°.

F1. Drilling activities at the Hawaii-2 Observatory, p. 9.

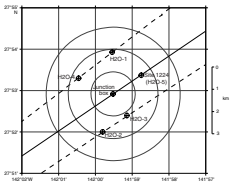


Before presenting the actual data, this report summarizes the seismic data available and the transfer functions used to compute ground motion from the digital counts. The data for the complete interval are then displayed in two formats: spectrograms and root-mean-square (RMS) time series. The analysis and interpretation of features in the seismic data are discussed in a companion paper (Bromirski et al., 2005).

## THE DATA SET

The buried seafloor seismometer at H2O consists of two sensors: a Guralp CMG-3T three-component broadband seismometer and a Geospace HS-1 three-component 4.5-Hz geophone. For each channel, two levels of analog gain are applied (high gain and low gain) prior to digitizing at 160 samples per second (sps) using 16-bit digitizers. The data are available from Incorporated Research Institutions for Seismology Data Management Center (IRIS-DMC) in standard for exchange of earthquake data (SEED) format at a variety of sampling rates. All of the results displayed here are based on the 12 160-sps data sets. Table T1 gives a summary of the channel identifiers. It is important to note that the gain was changed during the experiment for the vertical component of the Guralp sensor on JD360/2001 at 14:40:15 hr UTC. The data and transfer functions were updated at the IRIS-DMC in November 2002, the high-gain data displayed here were downloaded in January 2003, and the low-gain data displayed here were downloaded in February 2004.

T1. Channel identifiers, p. 63.

## TRANSFER FUNCTIONS

The data are acquired and stored in units of digital counts. The transfer functions of the sensors are given in "Response" files that are downloaded from the DMC at the same time as the data. (There is an option to apply the transfer function to the data while downloading the data from the DMC, but we chose not to do this. Instead, we used the IRIS-supplied function "evalresp" to compute the transfer functions and applied the transfer functions directly to the spectra.) Spectra in counts are converted to spectra in ground motion units (for example, accelera-

tion in units of nanometers per second squared) by multiplying by the inverse transfer function. Figure F2 summarizes the inverse transfer functions for the 12 channels of data discussed in this report. The Guralp channels are "flat to acceleration" from ~10 mHz to the low-pass antialiasing filters at ~8 Hz. Geophones are designed to be "flat to velocity" at frequencies above their natural frequency, which in this case is 4.5 Hz. Because the antialiasing filters are applied at ~8 Hz, these geophones are not being used in this "flat to velocity" band. The gains for the vertical channels of both the Guralp and geophone were originally set 6 dB higher than for the horizontals. The gain for the vertical Guralp was decreased by 6 dB on JD360/2001 to reduce the chances of clipping during the water gun shooting as the *JOIDES Resolution* arrived on site. After this time the gains on all three channels of the Guralp were the same.

As a check on the transfer functions, we compared spectra between Guralp and geophone sensors for the same time window. Figure F3 compares vertical channel spectra at 1300 hr UTC on JD360/2001 before the gain change on the vertical Guralp. Within the band 0.1–10 Hz the low- and high-gain channels have identical spectra but the Guralp is ~3 dB (a factor of 2 in power) higher than the geophone. Vertical channel spectra computed just after the gain change show a similar offset between Guralp and geophone data (Fig. F4). It appears as if the gain change on day 360 is being handled correctly but that there is a discrepancy between the Guralp and geophone transfer functions for the vertical component. A similar comparison of horizontal component data shows identical spectra in this band for Guralps and geophones, as expected (Fig. F5). (Note that all spectra have been doubled to allow for energy in the negative frequencies. This is necessary to satisfy Parseval's relation.)

Instrument noise can be inferred from Figures F3, F4, and F5.

1. The geophone curves are much higher than the Guralp curves at low frequency because of the instrument noise in the preamplifiers and Brownian motion in the geophones themselves (e.g., Riedesel et al., 1990; Stephen et al., 1994).
2. The low-gain channel of the vertical Guralps is higher than the high-gain channel at low frequencies because the gain was not enough to raise the signal level above the electronic noise.
3. The increase in noise levels on the Guralp horizontal components below 0.1 Hz is typical of tilt induced noise (Crawford and Webb, 2000; Araki et al. 2004).

## SPECTROGRAMS

All of the data for the 43-day interval of Leg 200 can be summarized in spectrogram displays of the amplitude of the spectra as a function of time. Power spectral density was computed for window lengths of 1,048,576 points (~1.82 hr). Within each window, fast Fourier transforms (ffts) were computed over 262,144 point intervals, with 75% overlap and Hanning tapers. Welch averaging was used to compute the power spectral densities from the 13 ffts. The spectrograms for all six channels are shown in Figures F6, F7, F8, F9, F10, and F11. Spectral amplitudes have been doubled to allow for the power in the negative frequencies.



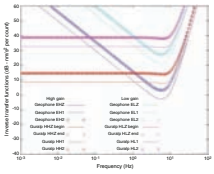



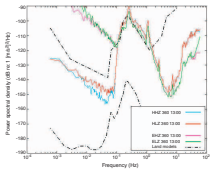



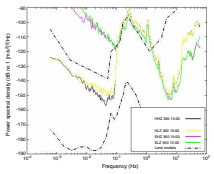



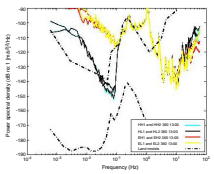



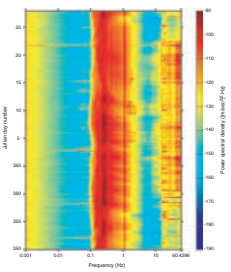



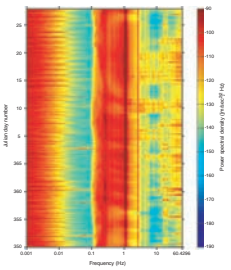

## RMS SUMMARIES

Because it is difficult to resolve some of the high-frequency features in the spectrograms, we also give summaries of the RMS levels of the time series in 1-octave bands from 0.25 to 32 Hz for each day from 16 December 2001 to 27 January 2002. These are shown in Figures **F12, F13, F14, F15, F16, F17, F18, F19, F20, F21, F22, F23, F24, F25, F26, F27, F28, F29, F30, F31, F32, F33, F34, F35, F36, F37, F38, F39, F40, F41, F42, F43, F44, F45, F46, F47, F48, F49, F50, F51, F52, F53,** and **F54** for the vertical component of the Guralp sensor (HHZ) only. The RMS levels are determined by integrating the power spectral density over 1-octave bands centered at the labeled frequencies. Power spectral density was computed for window lengths of 16,384 points (~102.4 s). Within each window, ffts were computed over 4096 point intervals, with 75% overlap and Hanning tapers. Welch averaging was used to compute the power spectral densities from the 13 ffts. These plots are useful for observing high-frequency events in the data such as whales, shipping, drilling noise, and so on. To observe low-frequency effects at the microseism peak and below, see the spectrograms.

## ACKNOWLEDGMENTS

This research used samples and/or data supplied by the Ocean Drilling Program (ODP). ODP is sponsored by the U.S. National Science Foundation (NSF) and participating countries under management of Joint Oceanographic Institutions (JOI), Inc. This work was supported by the U.S. Science Support Program (user reference: 418920-BA372; task order F001602). Support for P. Bromirski was also provided by the California Department of Boating and Waterways and the California Energy Commission PIER Program through the California Climate Change Center at SIO.



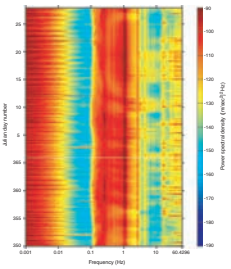



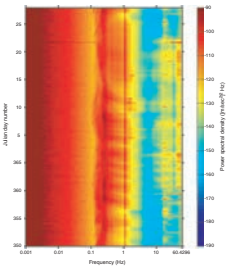



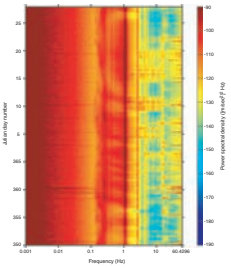



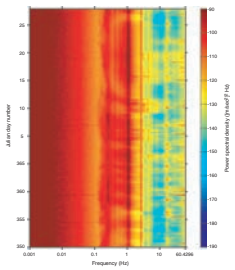



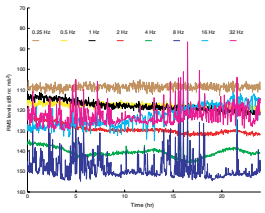

**F13.** Day 351, p. 21.

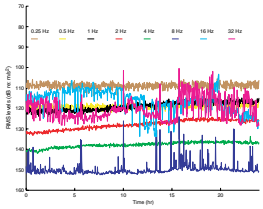

**F14.** Day 352, p. 22.

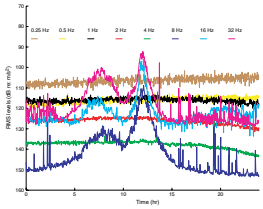

**F15.** Day 353, p. 23.

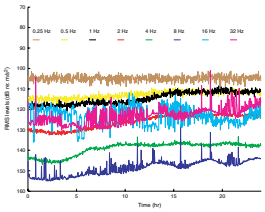

**F16.** Day 354, p. 24.

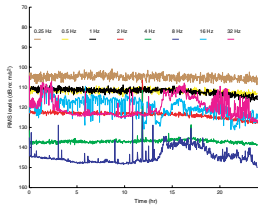

**F17.** Day 355, p. 25.

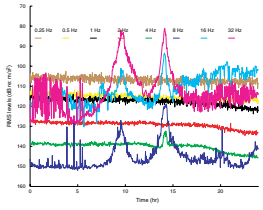

**F18.** Day 356, p. 26.

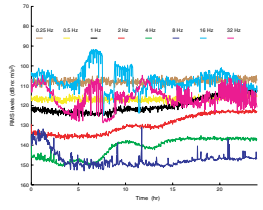

**F19.** Day 357, p. 27.

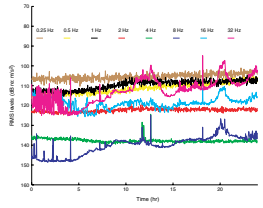

**F20.** Day 358, p. 28.

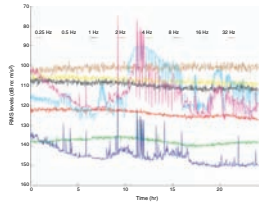

**F21.** Day 359, p. 29.

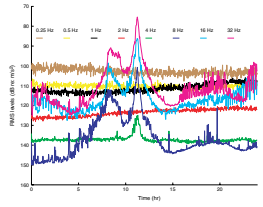

**F22.** Day 360, p. 30.

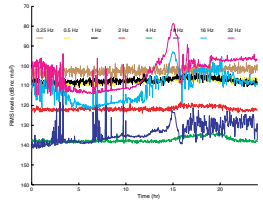

**F23.** Day 361, p. 31.

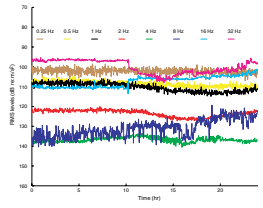

**F24.** Day 362, p. 32.

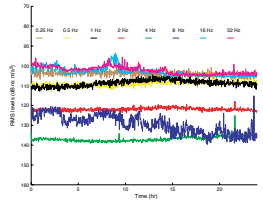

**F25.** Day 363, p. 33.

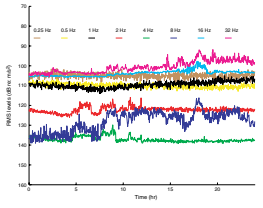

**F26.** Day 364, p. 34.

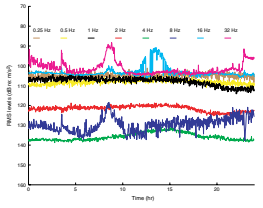

**F27.** Day 365, p. 35.

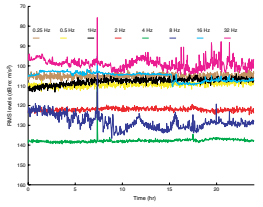

**F28.** Day 1, p. 36.

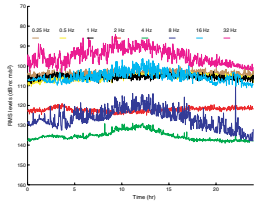

**F29.** Day 2, p. 37.

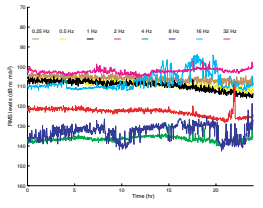

**F30.** Day 3, p. 38.

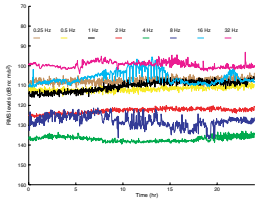

**F31.** Day 4, p. 39.

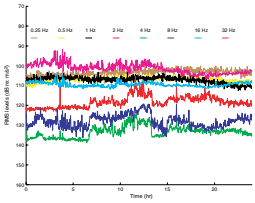

**F32.** Day 5, p. 40.

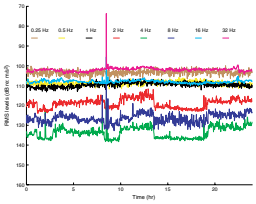

**F33.** Day 6, p. 41.

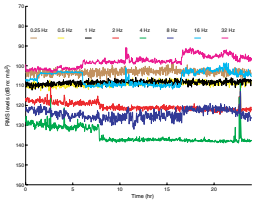

**F34.** Day 7, p. 42.

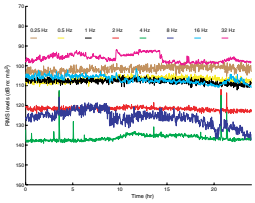

**F35.** Day 8, p. 43.

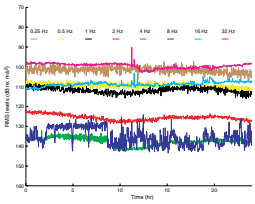

**F36.** Day 9, p. 44.

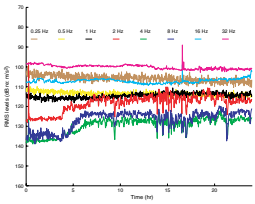

**F37.** Day 10, p. 45.

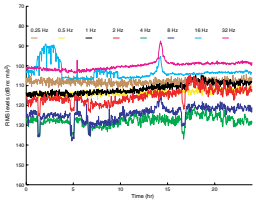

**F38.** Day 11, p. 46.

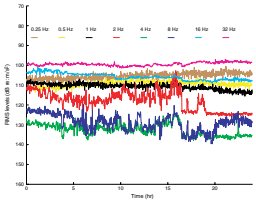

**F39.** Day 12, p. 47.

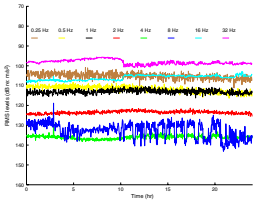

**F40.** Day 13, p. 48.

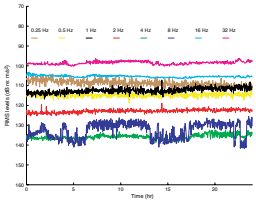

**F41.** Day 14, p. 49.

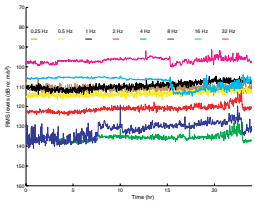

**F42.** Day 15, p. 50.

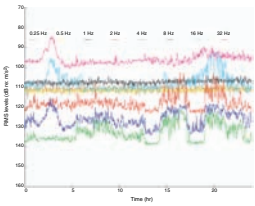

**F43.** Day 16, p. 51.

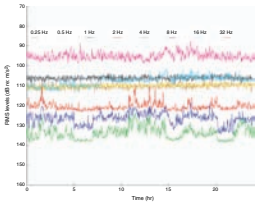

**F44.** Day 17, p. 52.

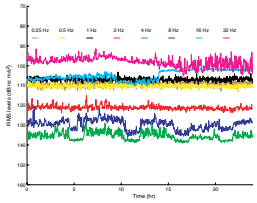

**F45.** Day 18, p. 53.

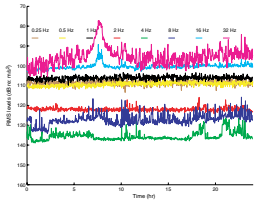

**F46.** Day 19, p. 54.

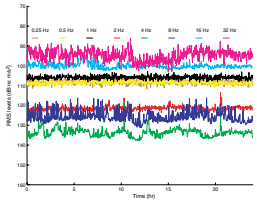

**F47.** Day 20, p. 55.

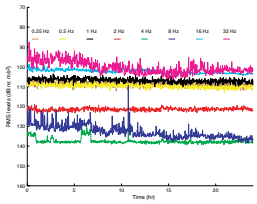

**F48.** Day 21, p. 56.

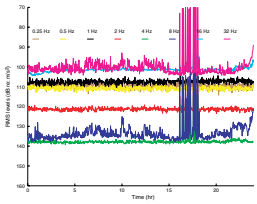

**F49.** Day 22, p. 57.

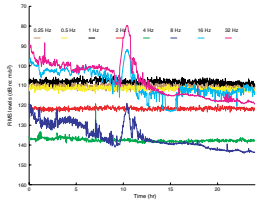

**F50.** Day 23, p. 58.

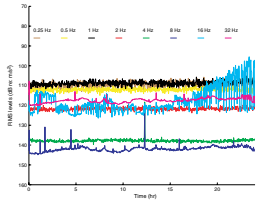

**F51.** Day 24, p. 59.

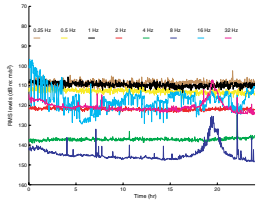

**F52.** Day 25, p. 60.

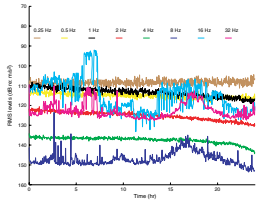

**F53.** Day 26, p. 61.

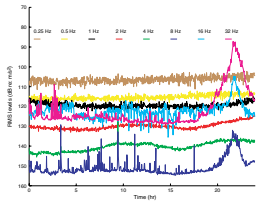

**F54.** Day 27, p. 62.

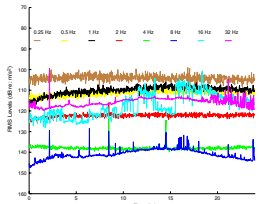

## REFERENCES

Araki, E., Shinohara, M., Sacks, S., Linde, A., Kanazawa, T., Shiobara, H., Mikada, H., and Suyehiro, K., 2004. Improvement of seismic observation in the ocean by use of seafloor boreholes. *Bull. Seismol. Soc. Am.,* 94(2):678–690.

Bromirski, P.D., Duennebier, F.K., Stephen, R.A., 2005. Mid-ocean microseisms. *Geochem, Geophys, Geosys.,* 6. **doi:10.1029/2004GC000768**

Crawford, W.C., and Webb, S.C., 2000. Identifying and removing tilt noise from low frequency (<0.1 Hz) seafloor vertical seismic data. *Bull. Seismol. Soc. Am.,* 90:952–963. **doi:10.1785/0119990121**

Duennebier, F.K., Harris, D.W., Jolly, J., Babinec, J., Copson, D., and Stiffel, K., 2002. The Hawaii-2 Observatory seismic system. *IEEE J. Oceanic Eng.,* 27:212–217. **doi:10.1109/JOE.2002.1002475**

Riedesel, M.A., Moore, R.D., and Orcutt, J.A., 1990. Limits of sensitivity of inertial seismometers with velocity transducers and electronic amplifiers. *Bull. Seismol. Soc. Am.,* 80:1725-1752.

Shipboard Scientific Party, 2003. Site 1224. *In* Stephen, R.A., Kasahara, J., Acton, G.D., et al., *Proc. ODP, Init. Repts.,* 200, 1–178 [CD-ROM]. Available from: Ocean Drilling Program, Texas A&M University, College Station TX 77845-9547, USA. [**HTML**]

Stephen, R.A., Kasahara, J., Acton, G.D., et al., 2003. *Proc. ODP, Init. Repts.,* 200 [Online]. Available from World Wide Web: <**http://www-odp.tamu.edu/publications/200_IR/200ir.htm**>. [Cited 2004-05-21]

Stephen, R.A., Koelsch, D.E., Berteaux, H., Bocconcelli, A., Bolmer, S., Cretin, J., Etourmy, N., Fabre, A., Goldsborough, R., Goulds, M., Kery, S., Laurent, J., Omnes, G., Peal, K.R., Swift, S.A., Turpening, R., and Zani, C., 1994. The Seafloor Borehole Array Seismic System (SEABASS) and VLF ambient noise. *Mar. Geophys. Res.,* 16:243–286. **doi:10.1007/BF01224745**

Stephen, R.A., Swift, S.A., and Greaves, R.J., 1997. *Bathymetry and Sediment Thickness Survey of the Hawaii-2 Cable,* WHOI-03-97: Woods Hole, MA (Woods Hole Oceanographic Institution).

**Figure F1.** All drilling activities at the Hawaii-2 Observatory (H2O) took place within 20 m of Site 1224 (see Figure F3 of Shipboard Scientific Party, 2003), which is 1.48 km northeast of the broadband seismometer at the H2O junction box. Alternate drilling sites (H2O-1 through H2O-4) discussed in the Leg 200 *Scientific Prospectus* are also shown (circles with crosses). Circles are drawn at 1, 2, and 3 km radii from the H2O junction box. Also shown are the locations of the single-channel seismic lines acquired during the site survey cruise in 1997 (dashed lines) (Stephen et al., 1997) and the track line taken by the *JOIDES Resolution* on 26 December 2001 (solid line).

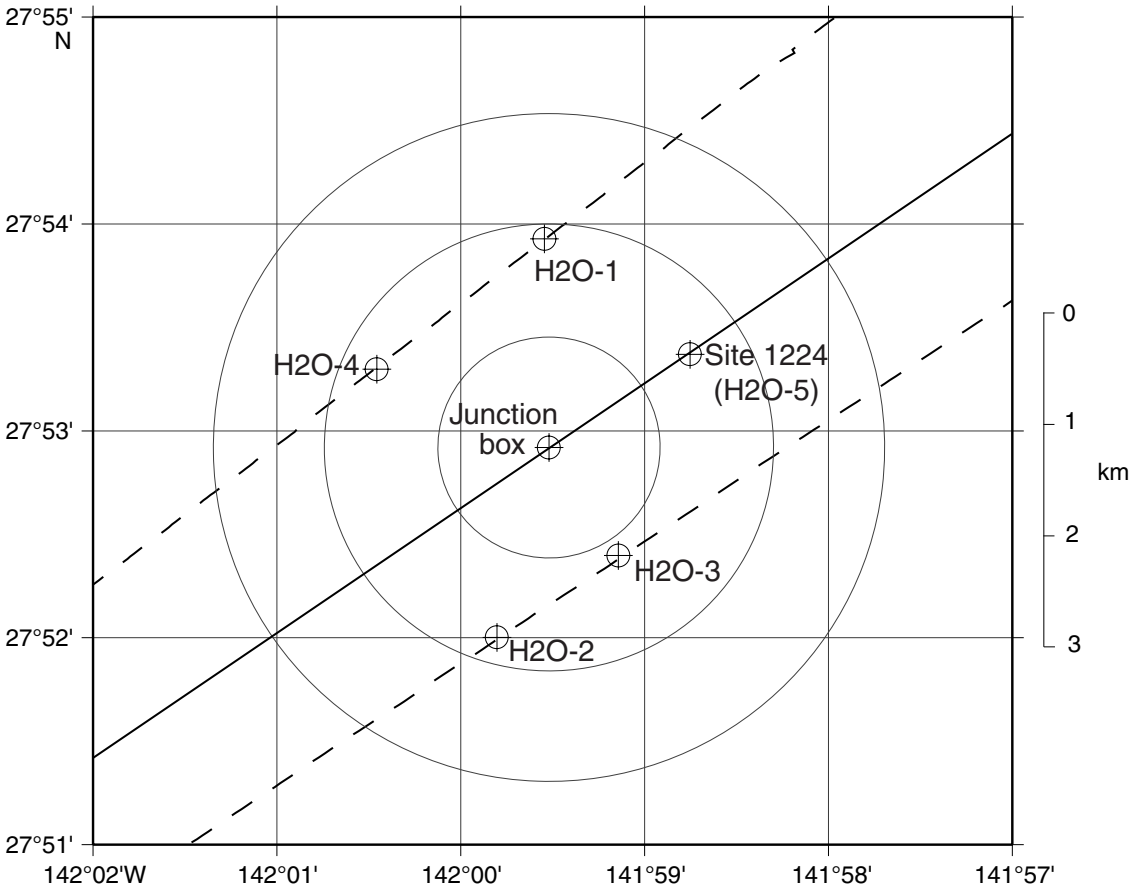

**Figure F2.** Inverse transfer functions for the two seismic sensors at the Hawaii-2 Observatory. These apply to data acquired at 160 sps. For each item listed, the first letter stands for geophone (E) or Guralp (H), the second stands for high (H) or low (L) gain channels, and the third stands for vertical component (Z). Numbers in third position indicate horizontal components.

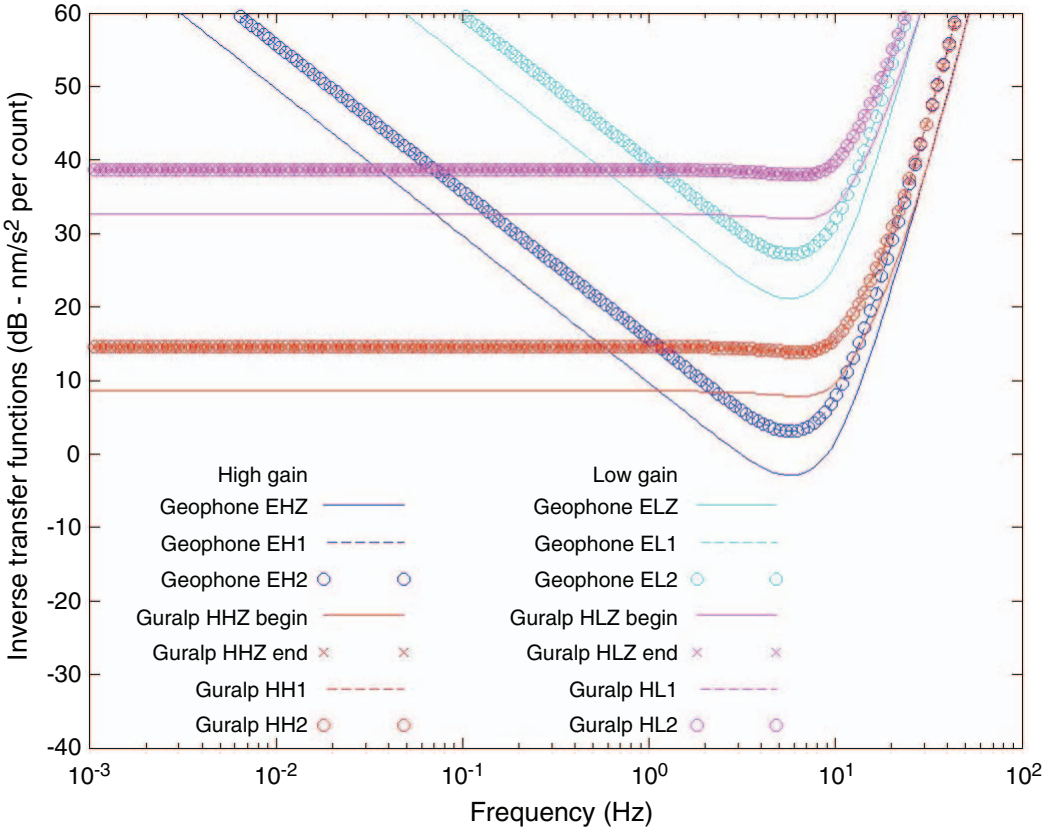

**Figure F3.** Comparison of vertical Guralp and geophone spectra for the same time interval (1300 hr) (high- and low-gain channels) in a window just before the gain change on JD360/2001. The geophone is an inexpensive sensor intended for use above its natural frequency of 4.5 Hz. It is encouraging that it resolves the microseism peak at ~0.25 Hz, but the geophone spectra rise quickly below 0.1 Hz because of instrument noise. Above ~2 Hz the geophone data are quieter than the Guralp. For each item listed, the first letter stands for geophone (E) or Guralp (H), the second stands for high (H) or low (L) gain channels, and the third stands for vertical component (Z). Numbers in third position indicate horizontal components.

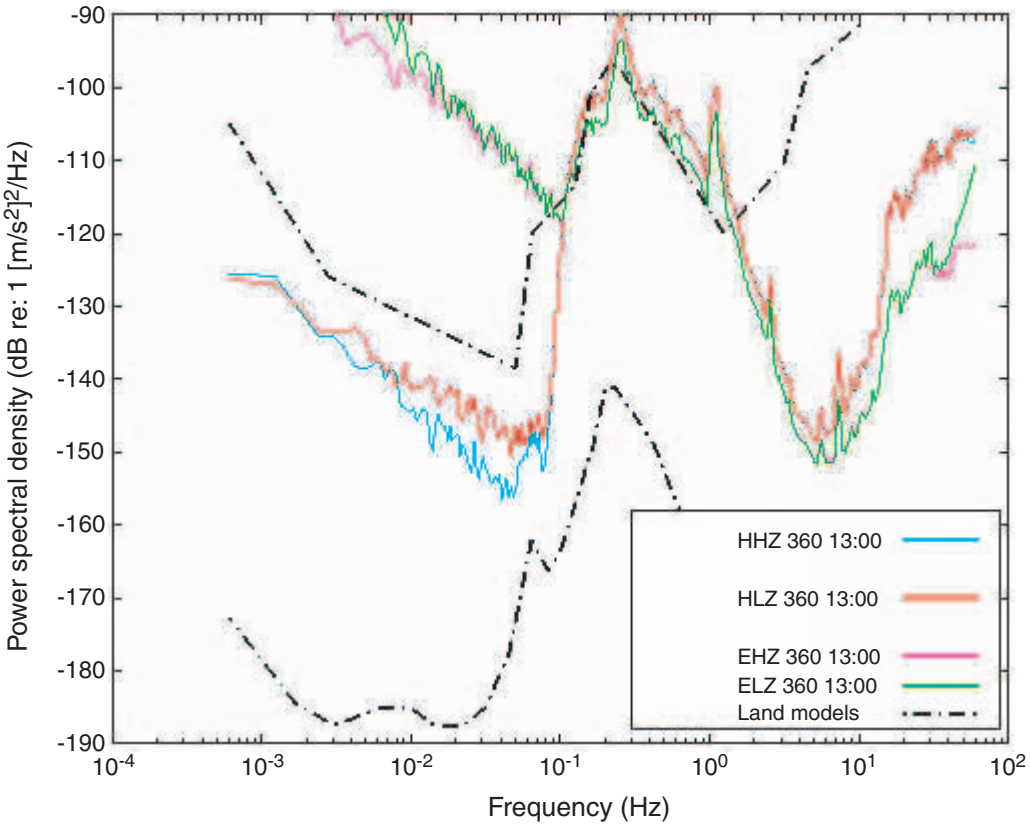

**Figure F4.** Comparison of vertical Guralp and geophone spectra for the same time interval (1500 hr) (high- and low-gain channels) in a window just after the gain change on JD360/2001. Because the Guralp and geophone spectra differ from one another (which is unexpected) but are similar before and after the gain change (compare with Figure F3, which is expected), we suspect that there is a discrepancy between the Guralp and geophone transfer functions for the vertical component. For each item listed, the first letter stands for geophone (E) or Guralp (H), the second stands for high (H) or low (L) gain channels, and the third stands for vertical component (Z). Numbers in the third position indicate horizontal components.

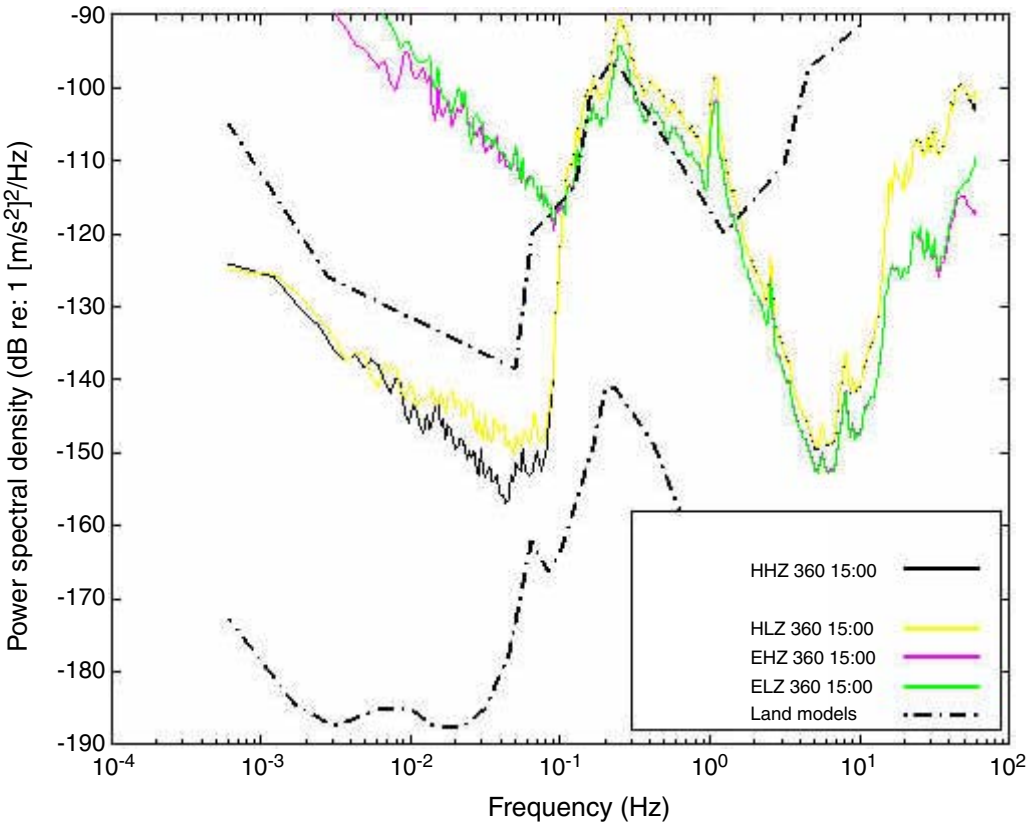

**Figure F5.** Comparison of horizontal Guralp and geophone spectra for the same time interval (1300 hr) (high- and low-gain channels) in a window just before the gain change on JD360/2001. Because the gain change was applied to the vertical Guralp only it is not necessary to check the horizontal spectra after the gain change. Note that the low-gain channel data virtually masks the high-gain channel data. For each item listed, the first letter stands for geophone (E) or Guralp (H), the second stands for high (H) or low (L) gain channels, and numbers in the third position indicate horizontal components.

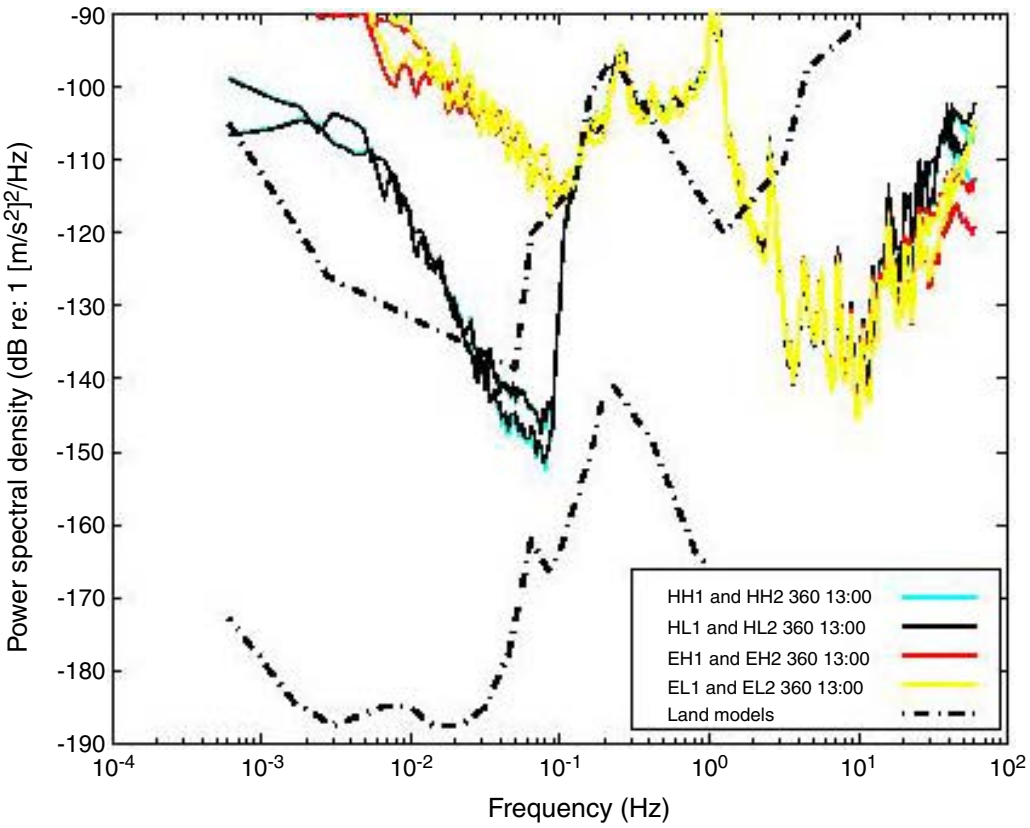

**Figure F6.** Spectrogram from day 350 in 2001 to day 27 in 2002 for the vertical component of the broadband Guralp sensor.

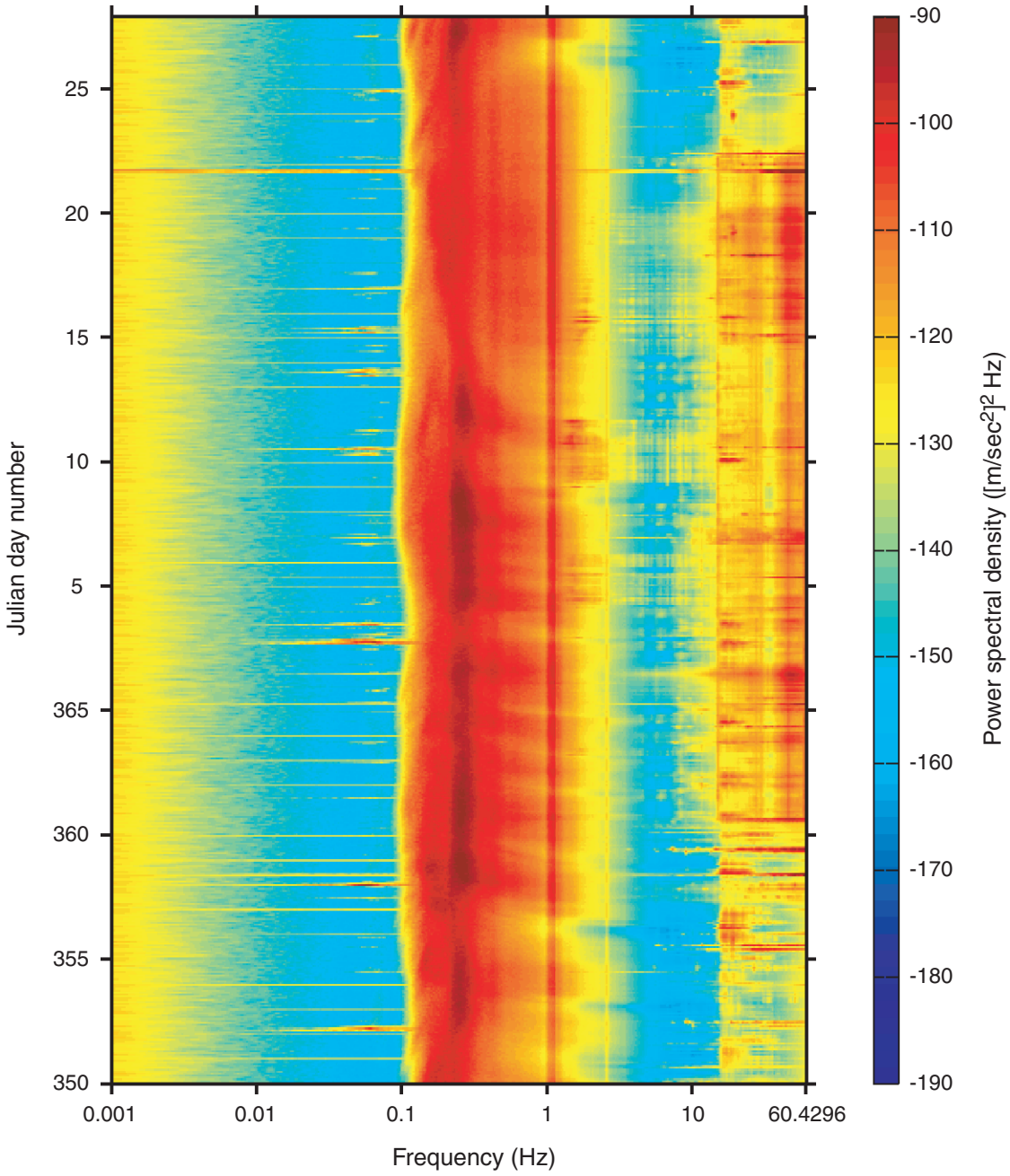

**Figure F7.** Spectrogram from day 350 in 2001 to day 27 in 2002 for the horizontal 1 component of the broadband Guralp sensor.

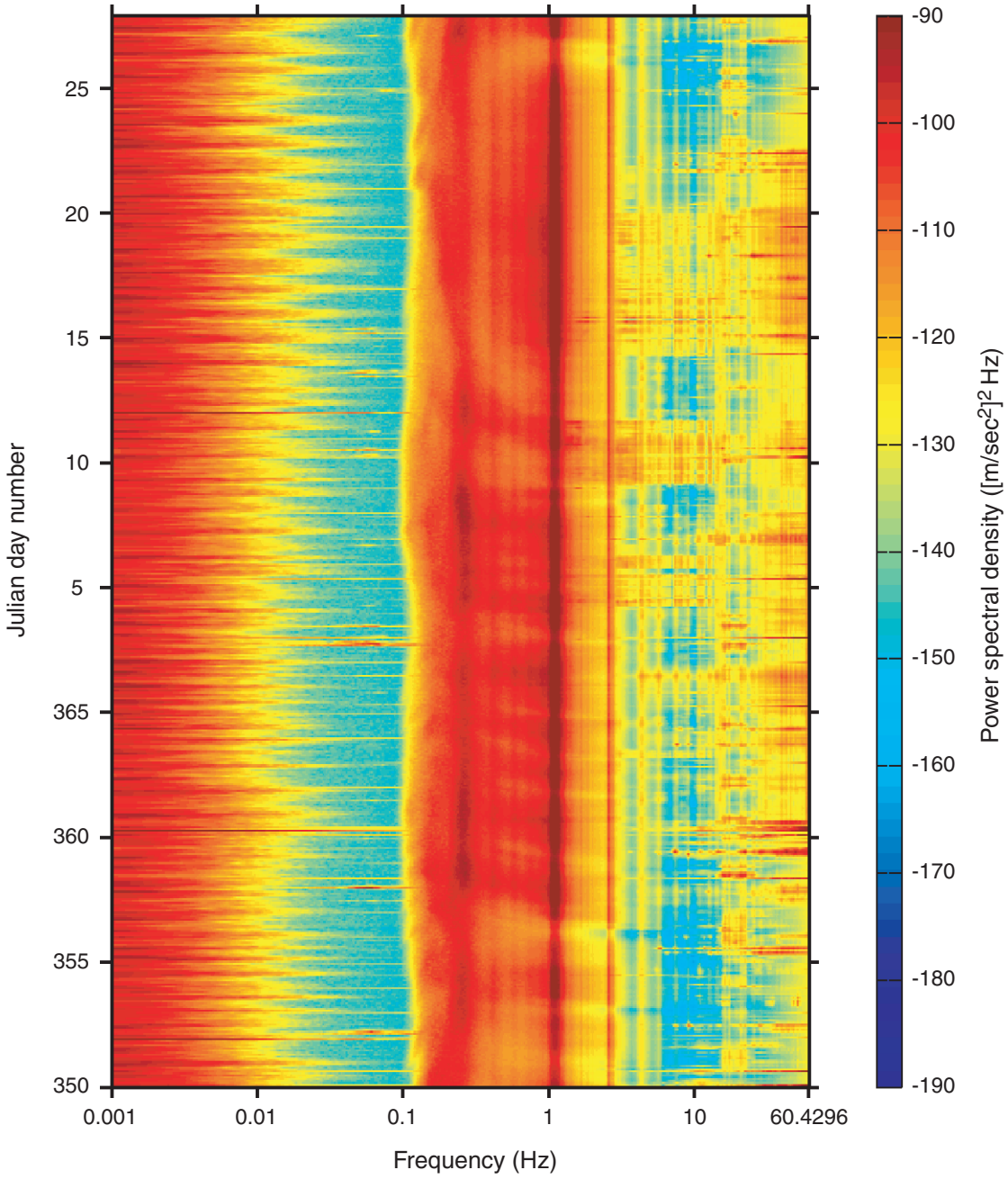

**Figure F8.** Spectrogram from day 350 in 2001 to day 27 in 2002 for the horizontal 2 component of the Guralp sensor.

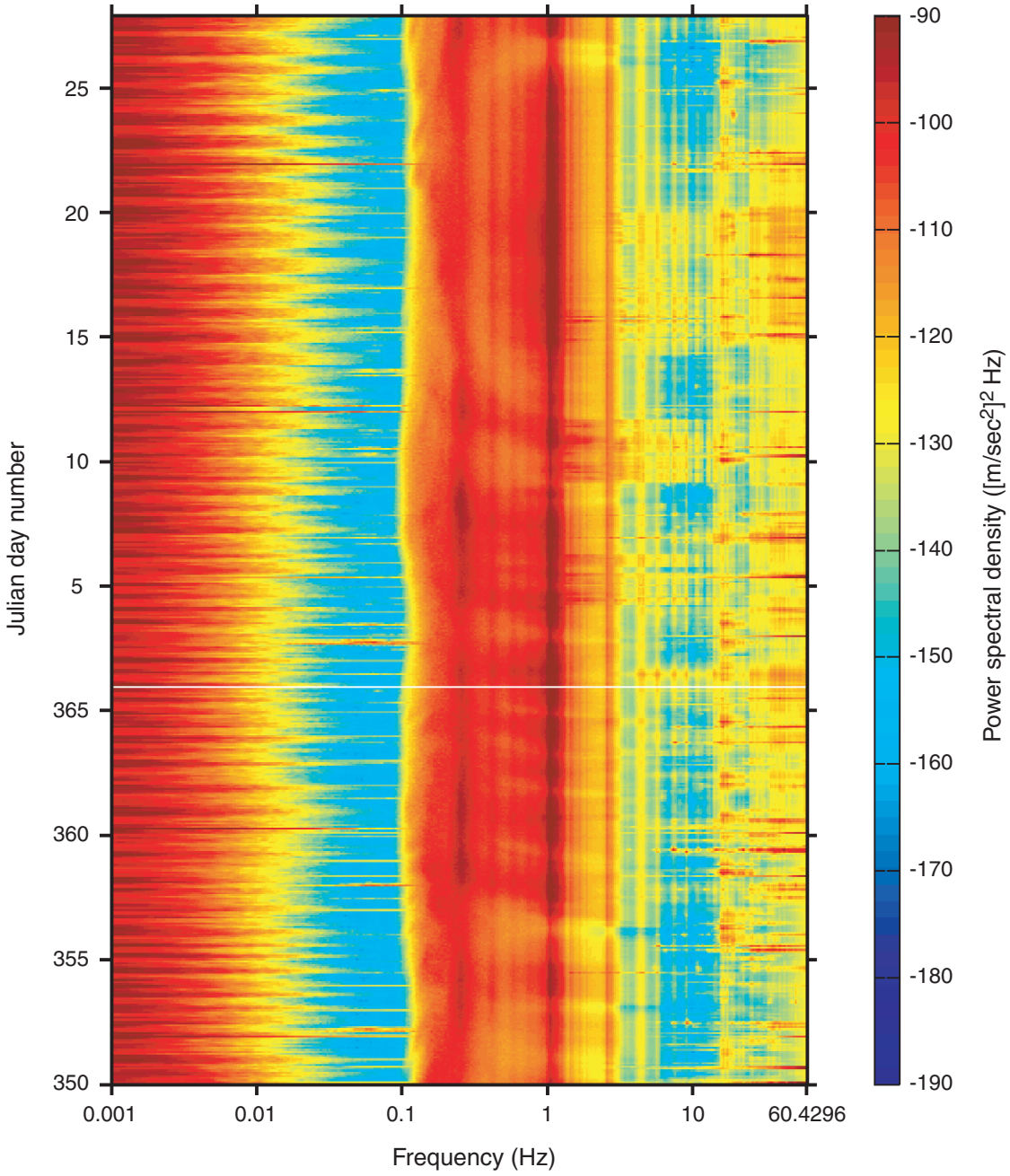

**Figure F9.** Spectrogram from day 350 in 2001 to day 27 in 2002 for the vertical component of the geophone sensor.

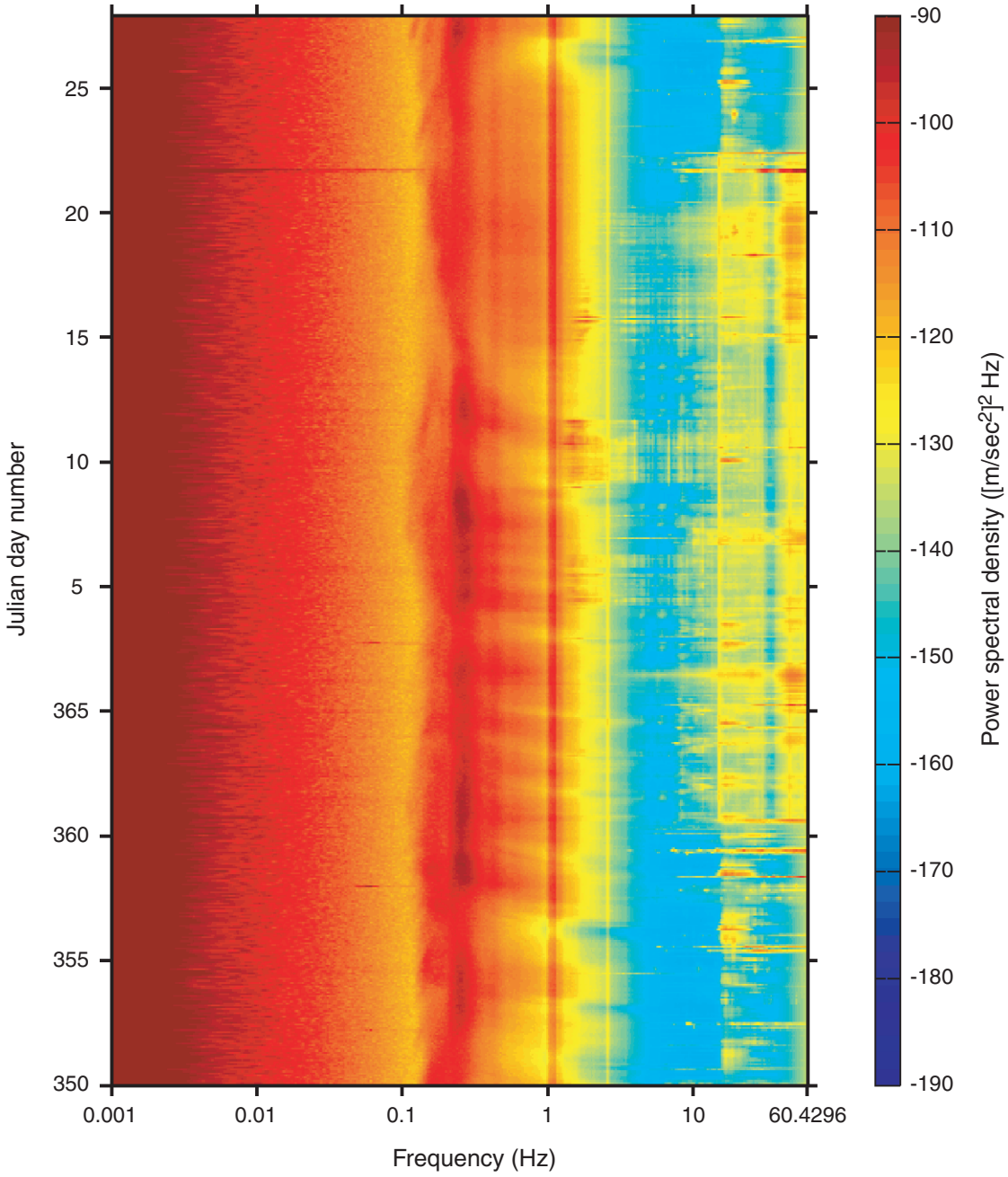

**Figure F10.** Spectrogram from day 350 in 2001 to day 27 in 2002 for the horizontal 1 component of the geophone sensor.

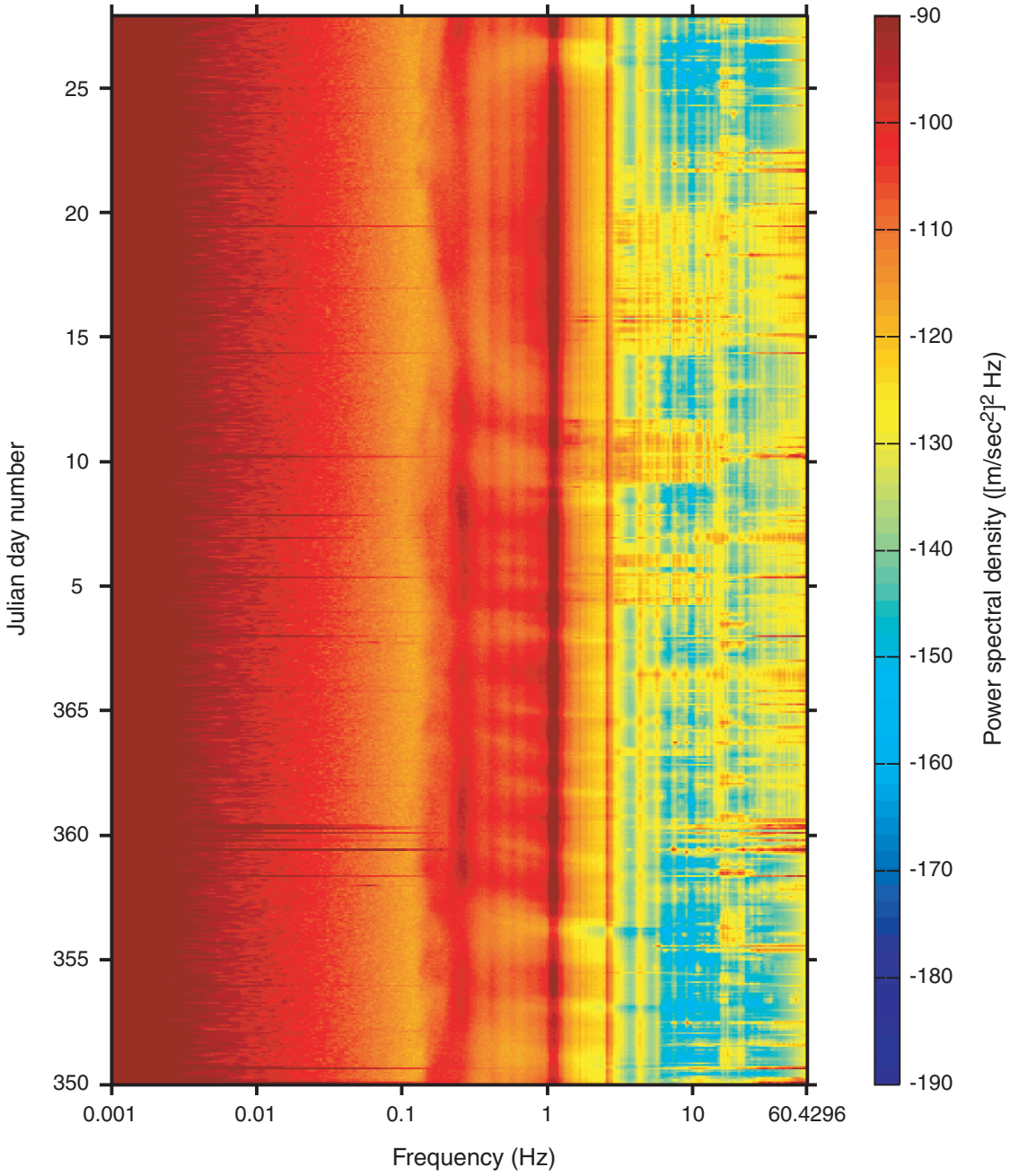

**Figure F11.** Spectrogram from day 350 in 2001 to day 27 in 2002 for the horizontal 2 component of the geophone sensor.

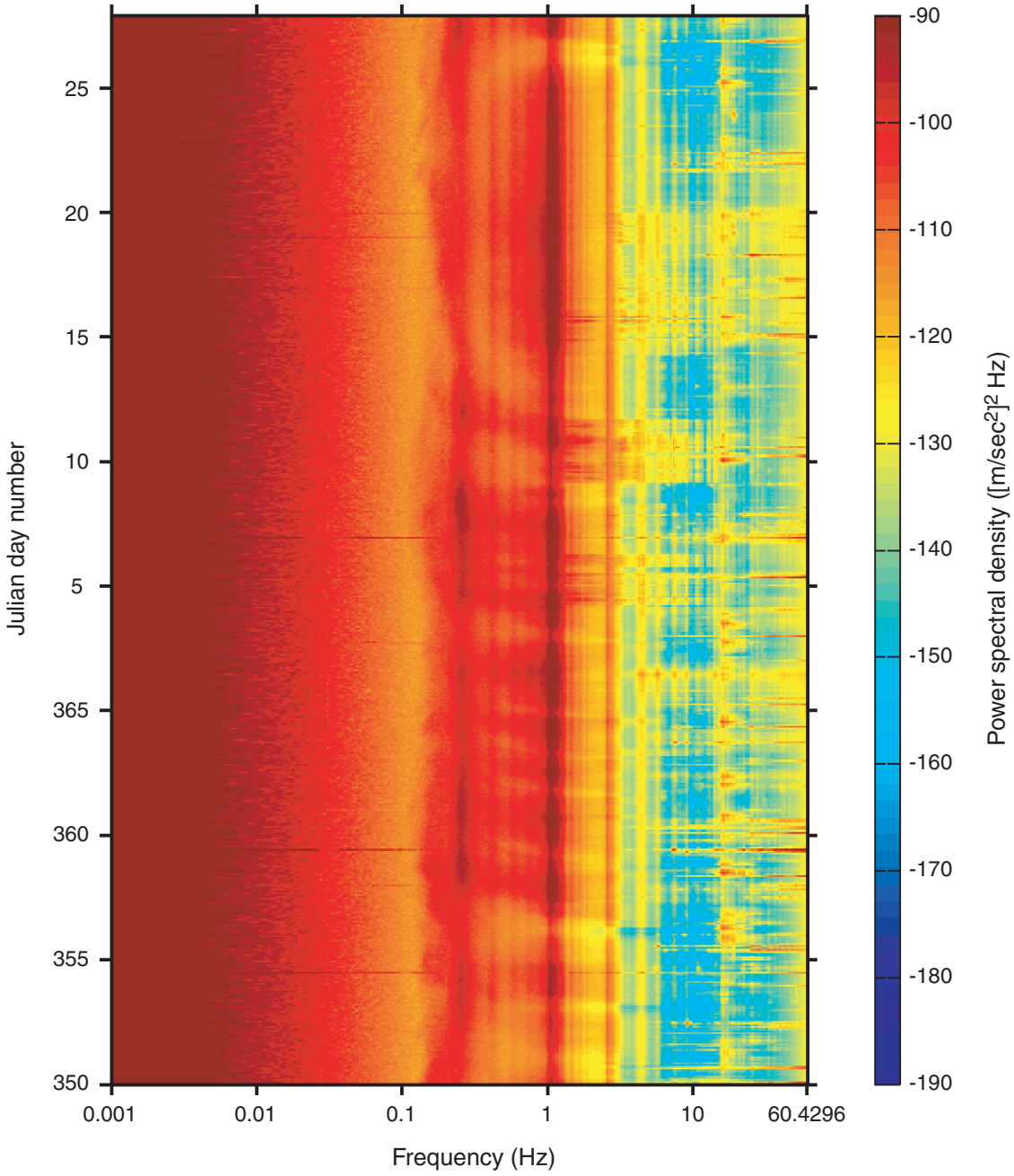

**Figure F12.** RMS energy levels in octave bands centered at the frequencies indicated for day 350 in 2001.

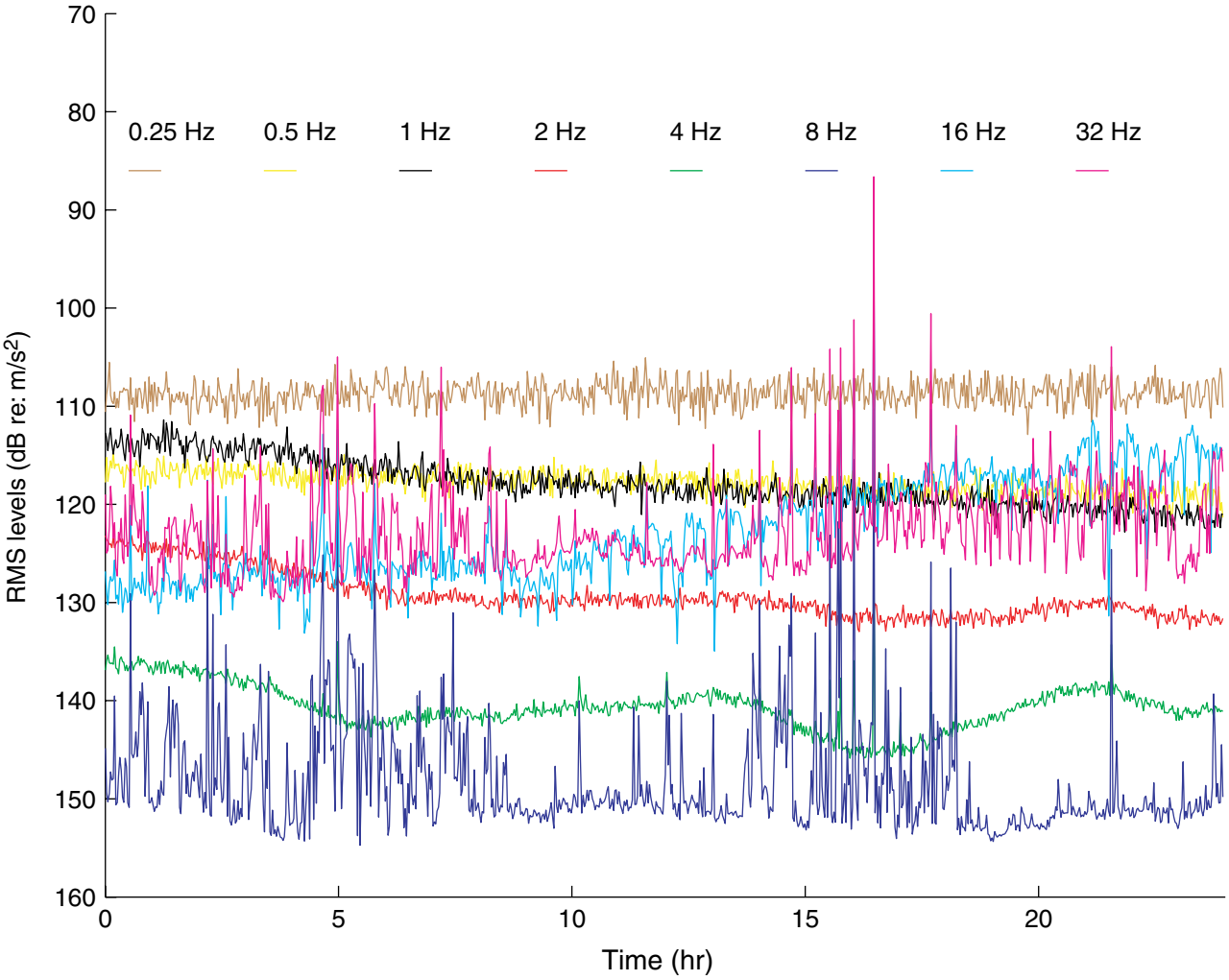

**Figure F13.** RMS energy levels in octave bands centered at the frequencies indicated for day 351 in 2001.

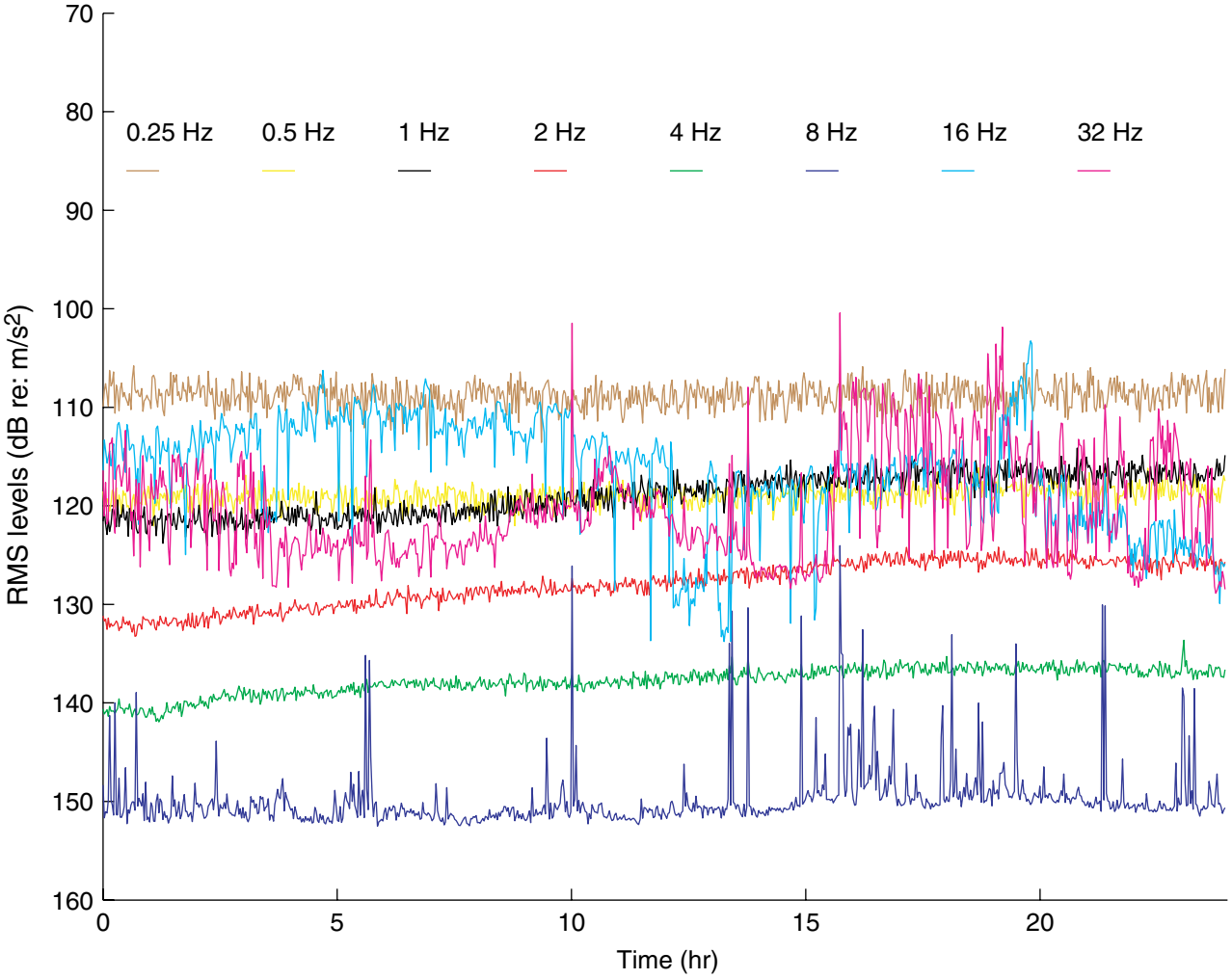

**Figure F14.** RMS energy levels in octave bands centered at the frequencies indicated for day 352 in 2001.

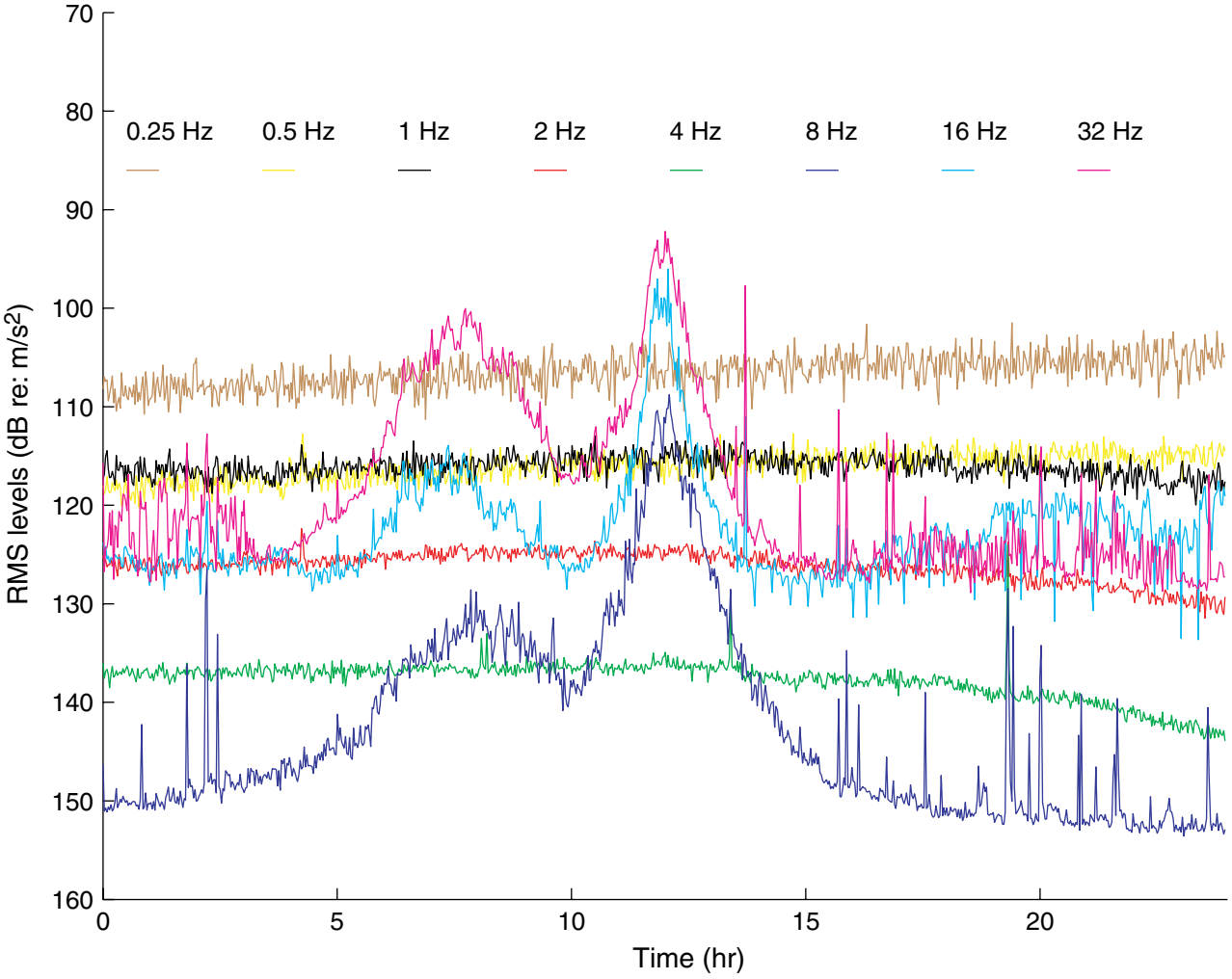

**Figure F15.** RMS energy levels in octave bands centered at the frequencies indicated for day 353 in 2001.

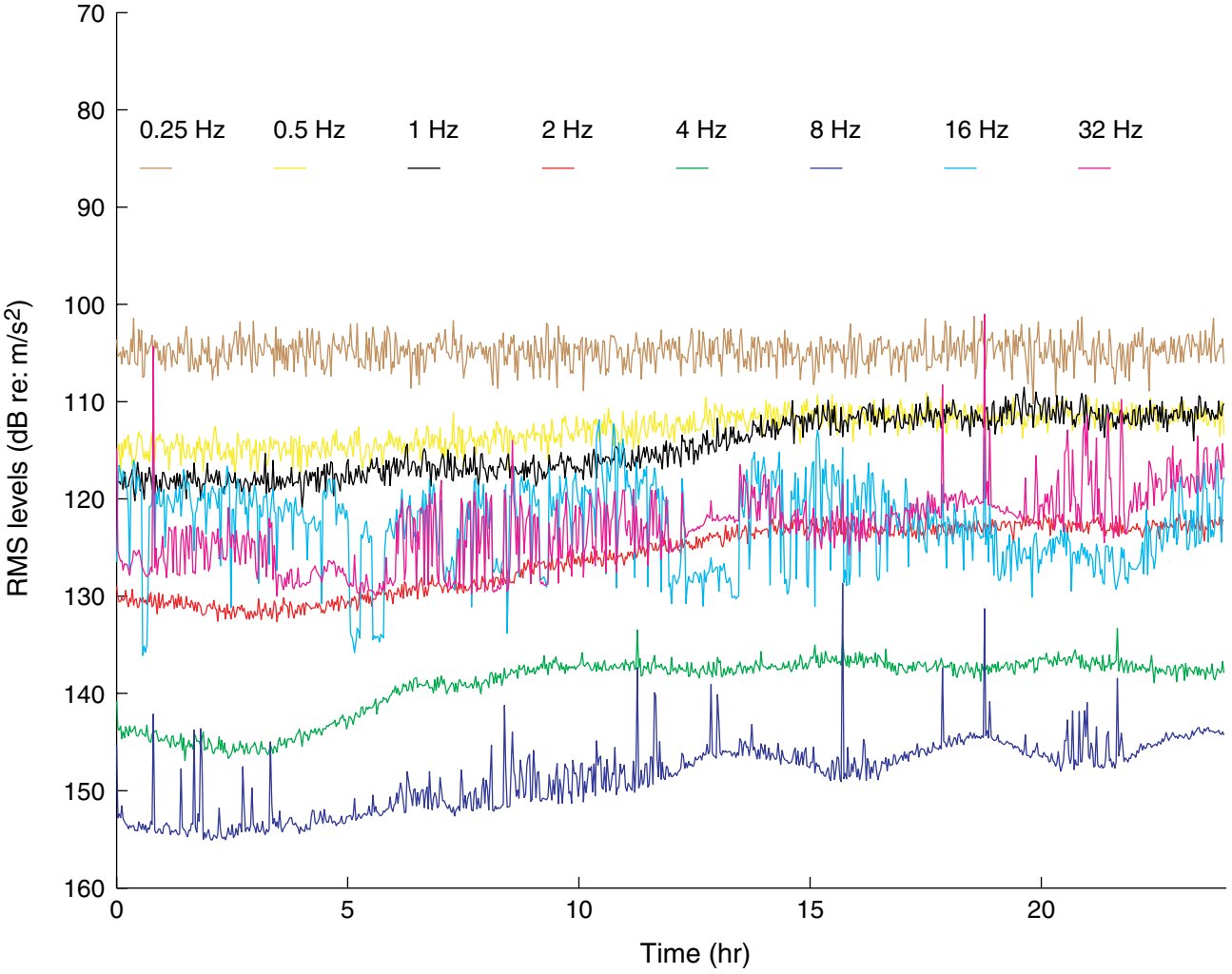

**Figure F16.** RMS energy levels in octave bands centered at the frequencies indicated for day 354 in 2001.

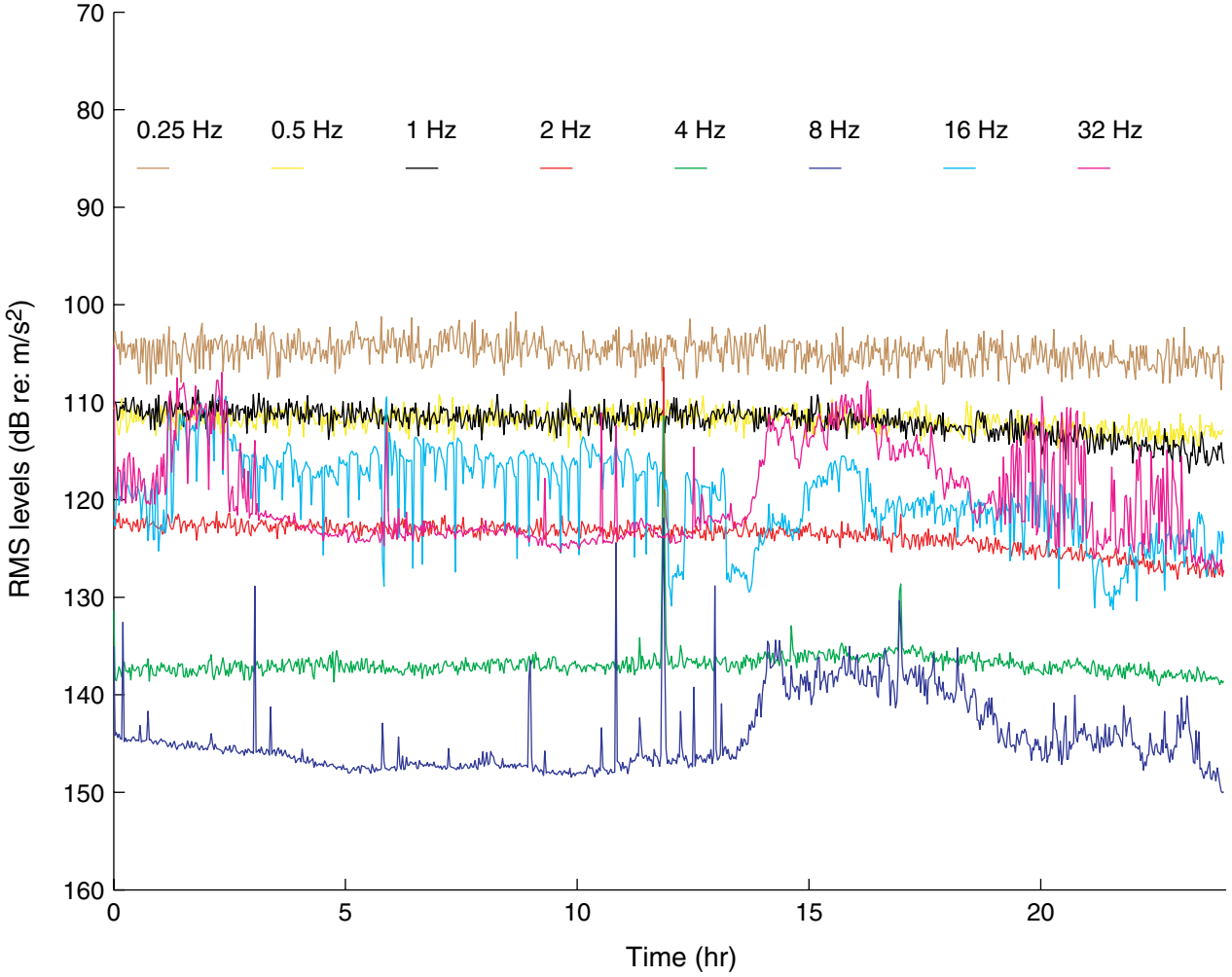

**Figure F17.** RMS energy levels in octave bands centered at the frequencies indicated for day 355 in 2001.

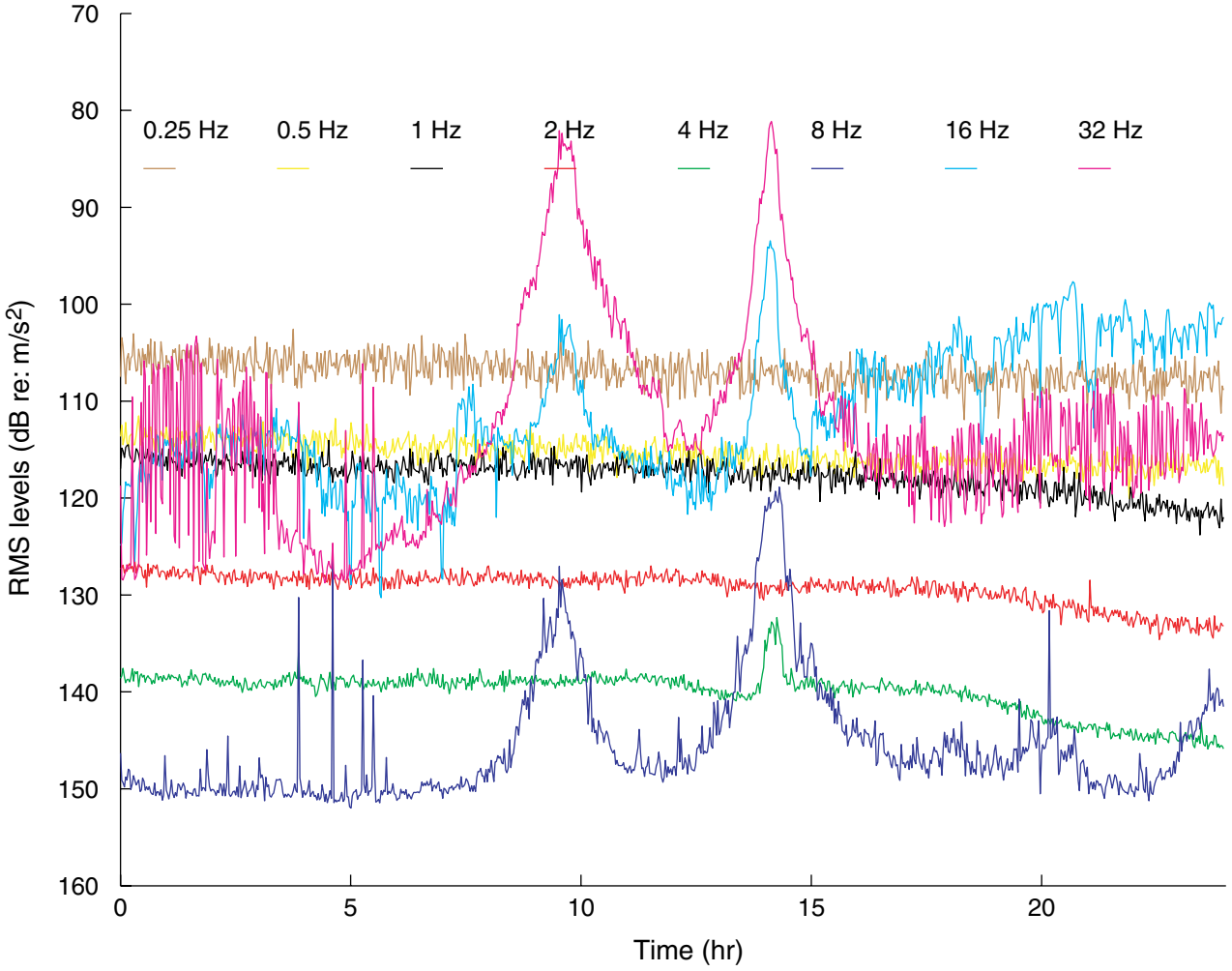

**Figure F18.** RMS energy levels in octave bands centered at the frequencies indicated for day 356 in 2001.

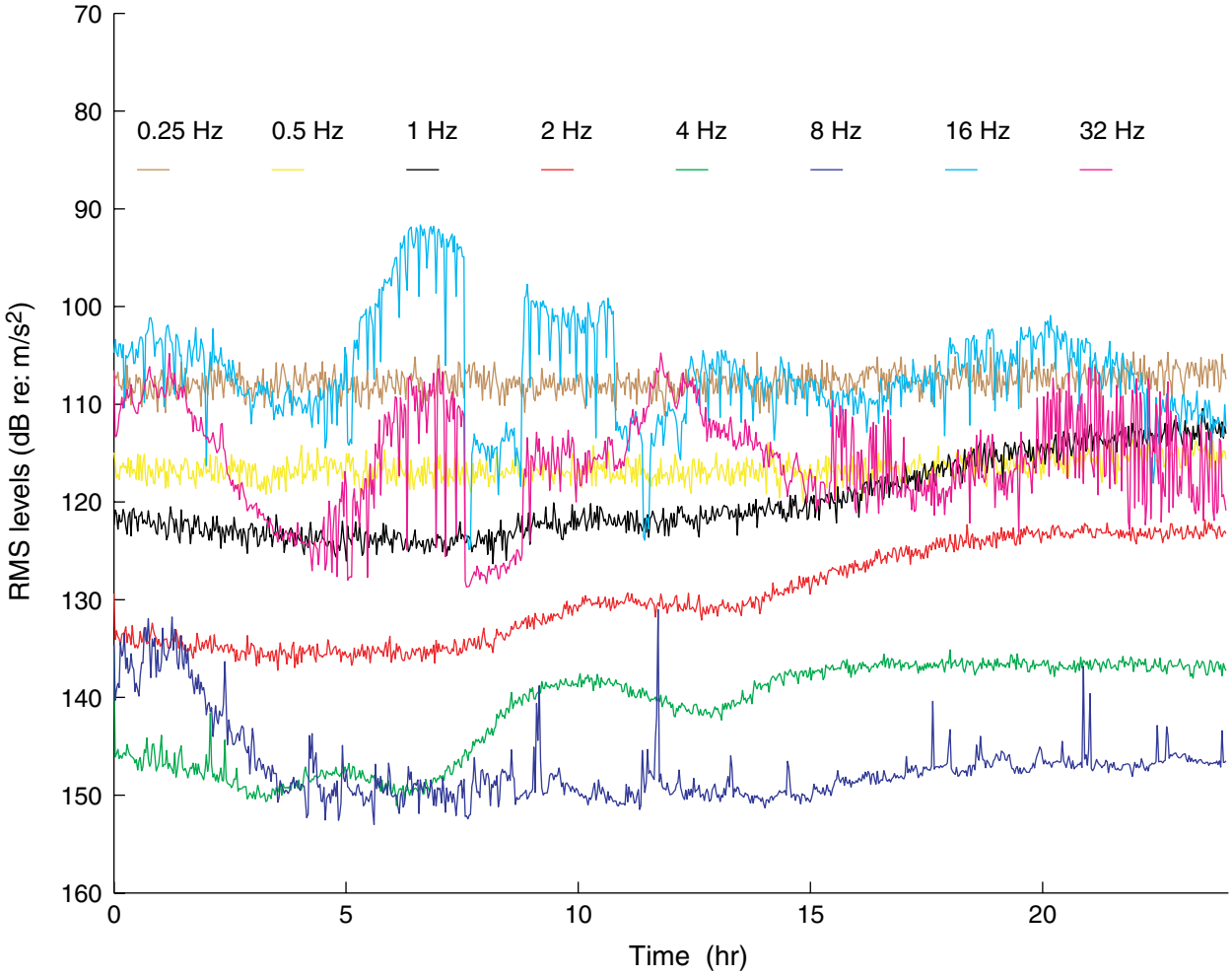

**Figure F19.** RMS energy levels in octave bands centered at the frequencies indicated for day 357 in 2001.

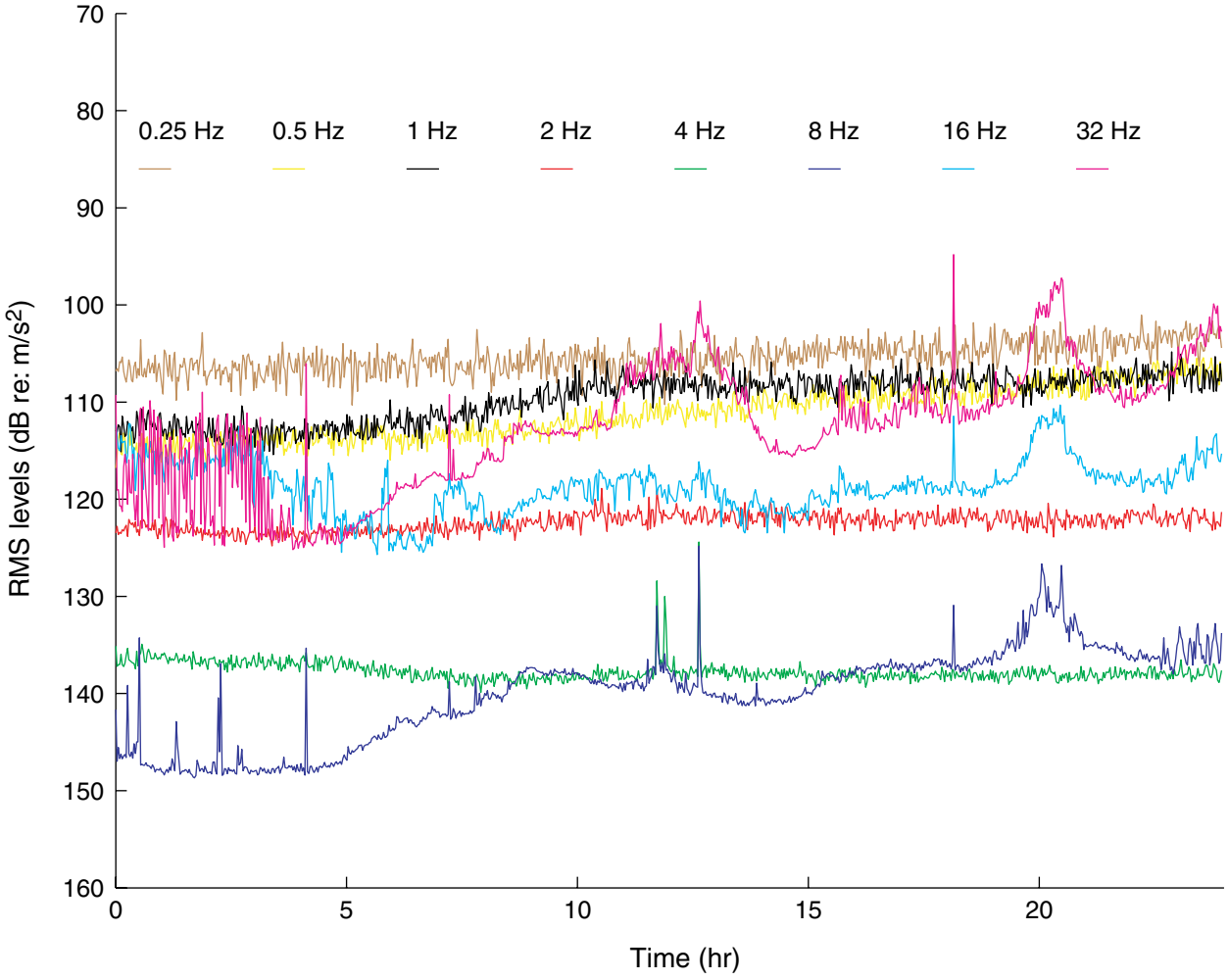

**Figure F20.** RMS energy levels in octave bands centered at the frequencies indicated for day 358 in 2001.

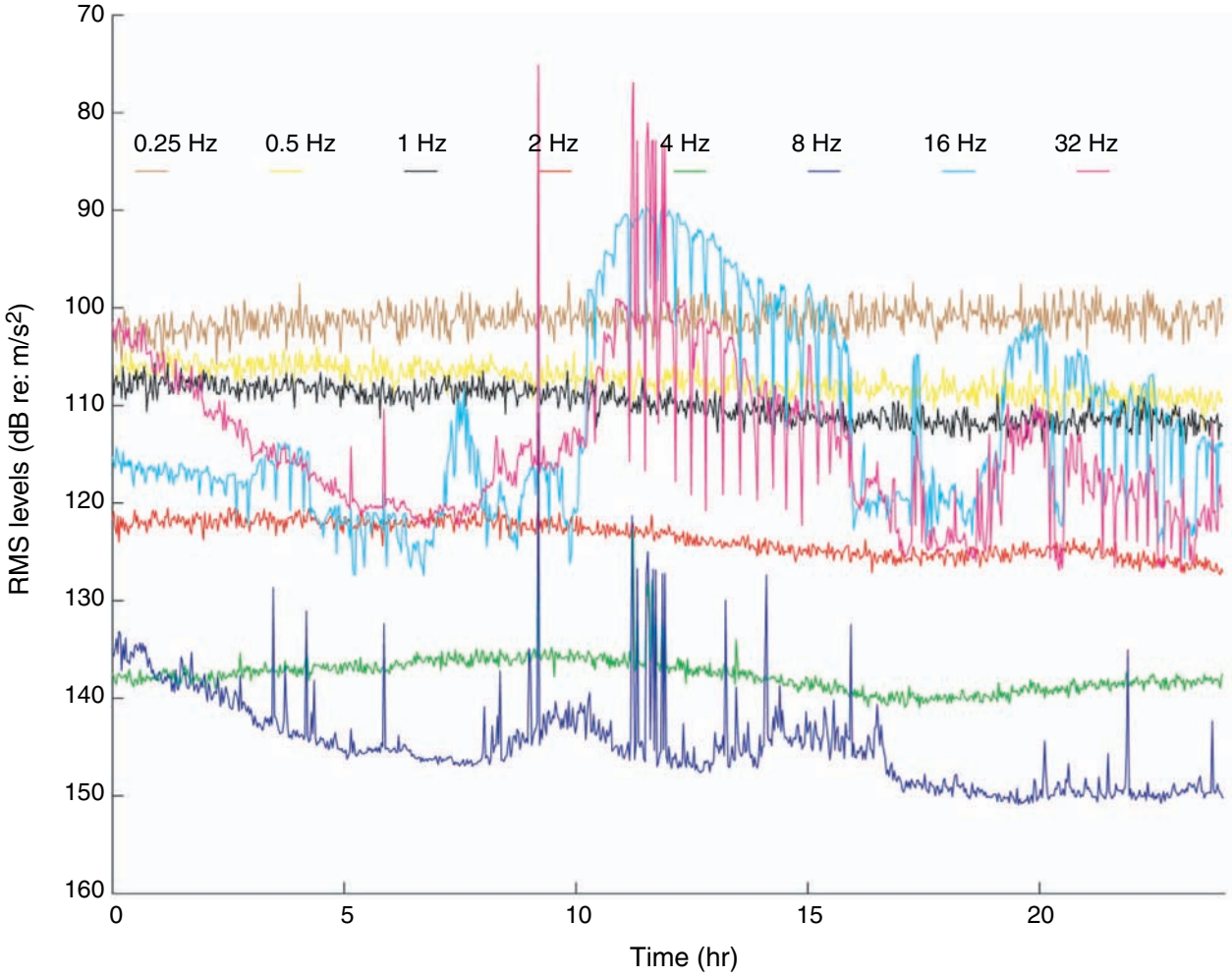

**Figure F21.** RMS energy levels in octave bands centered at the frequencies indicated for day 359 in 2001.

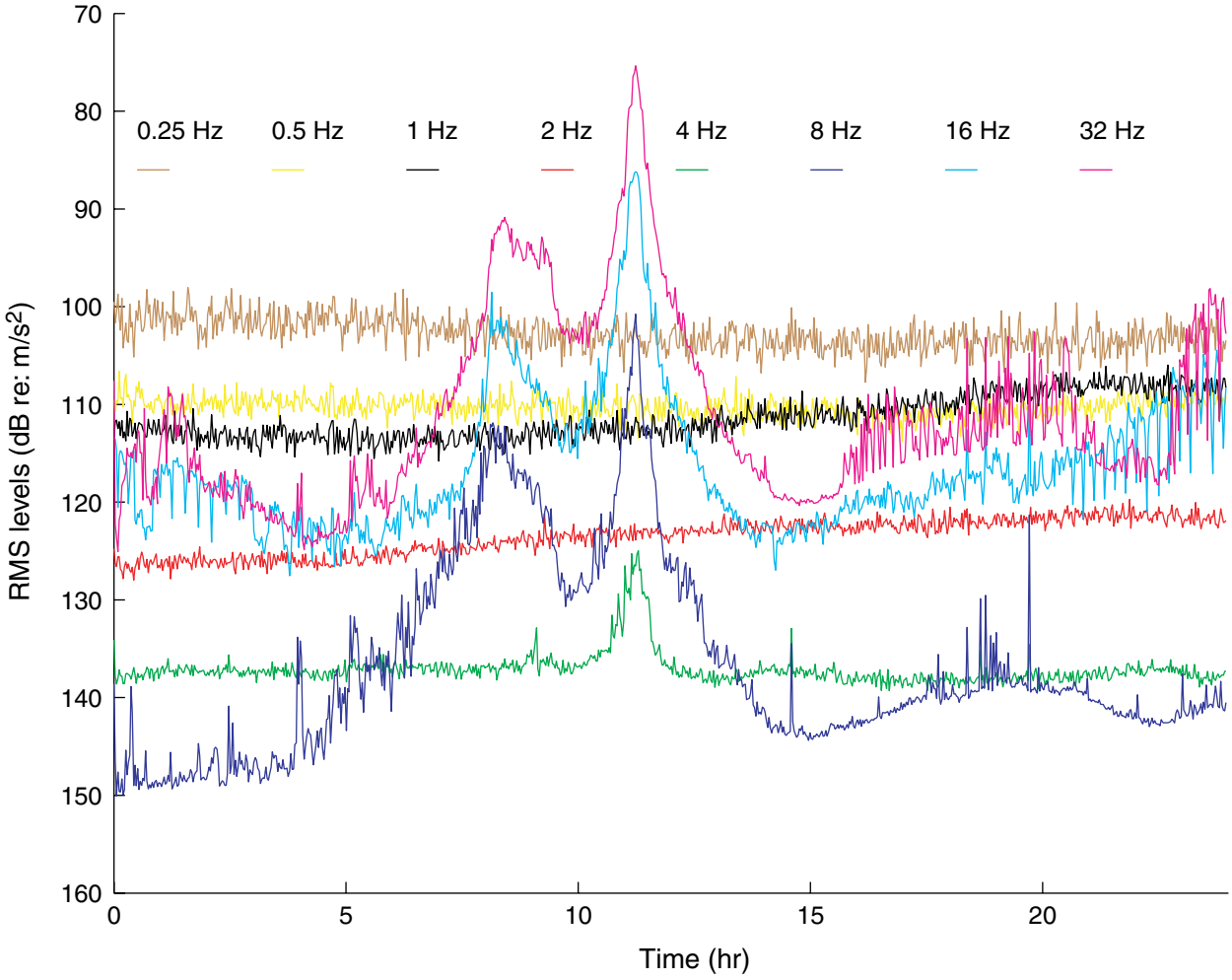

**Figure F22.** RMS energy levels in octave bands centered at the frequencies indicated for day 360 in 2001.

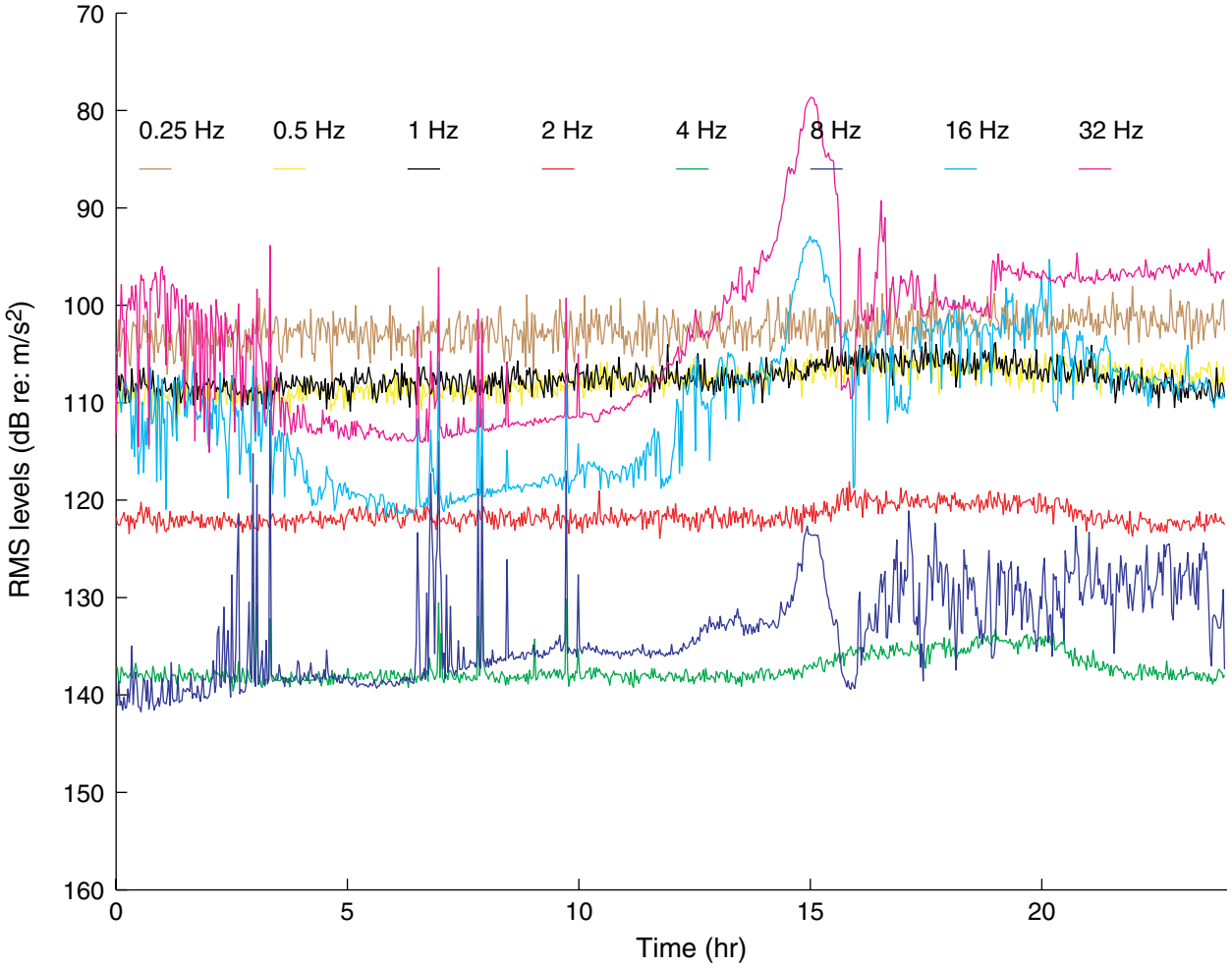

**Figure F23.** RMS energy levels in octave bands centered at the frequencies indicated for day 361 in 2001.

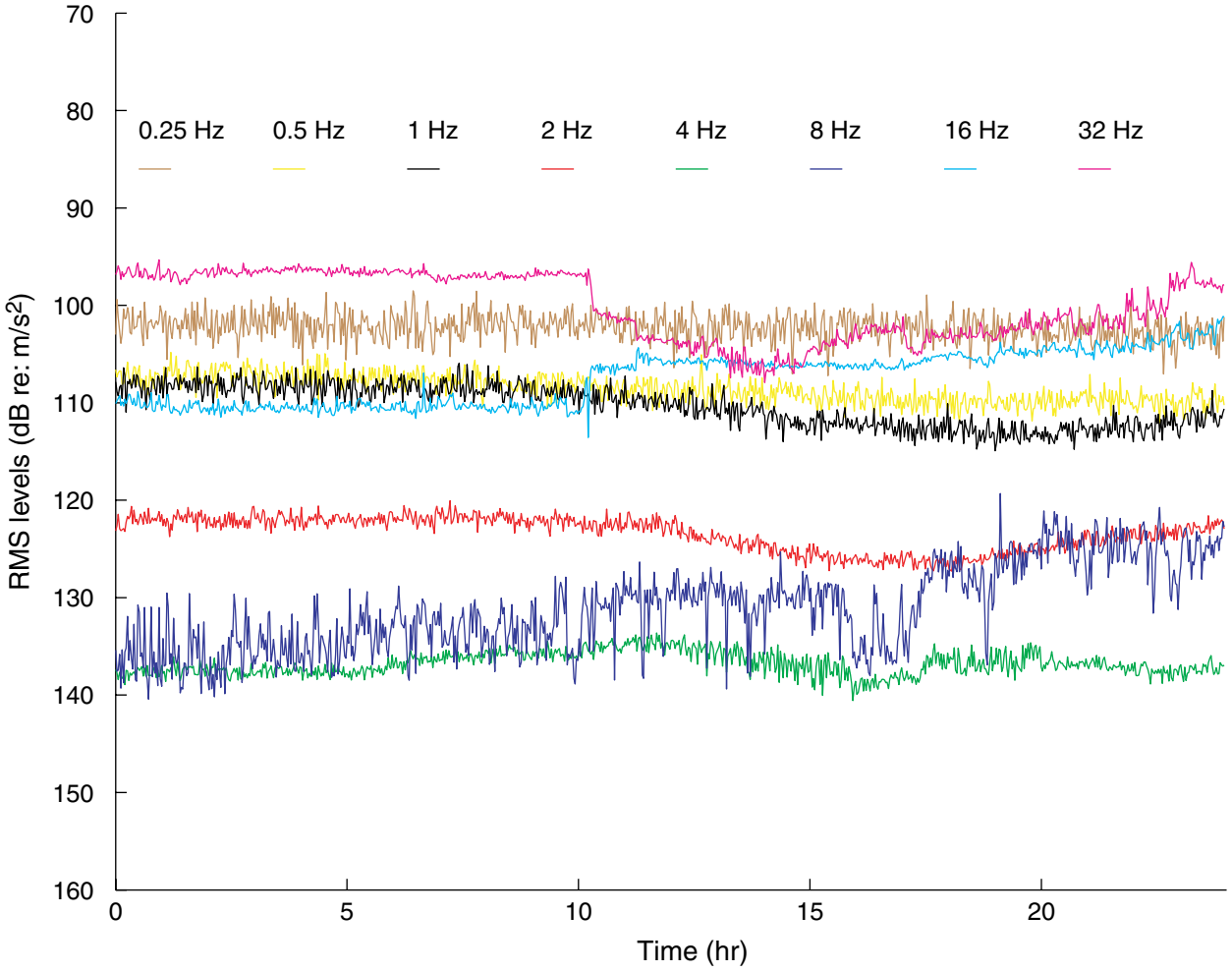

**Figure F24.** RMS energy levels in octave bands centered at the frequencies indicated for day 362 in 2001.

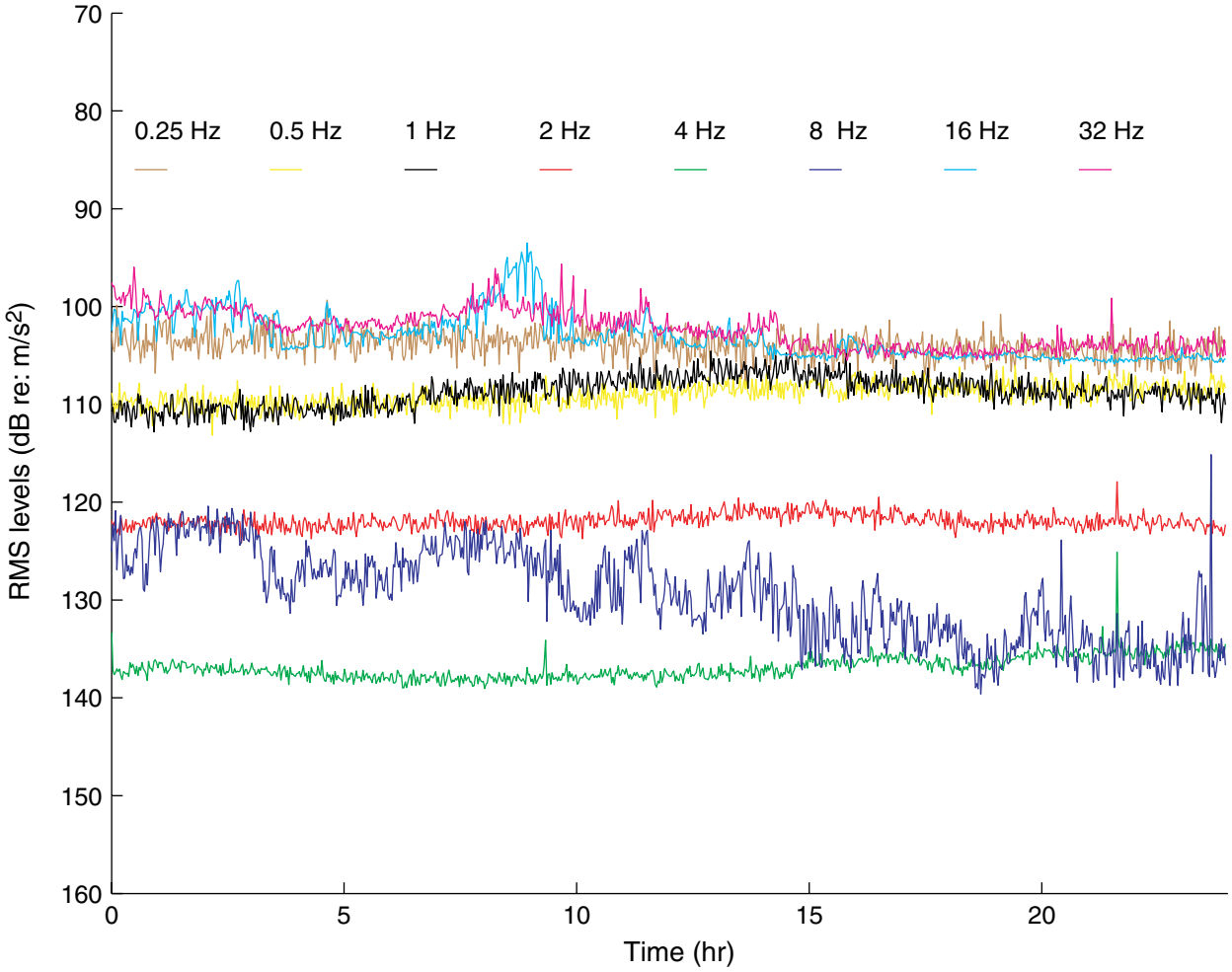

**Figure F25.** RMS energy levels in octave bands centered at the frequencies indicated for day 363 in 2001.

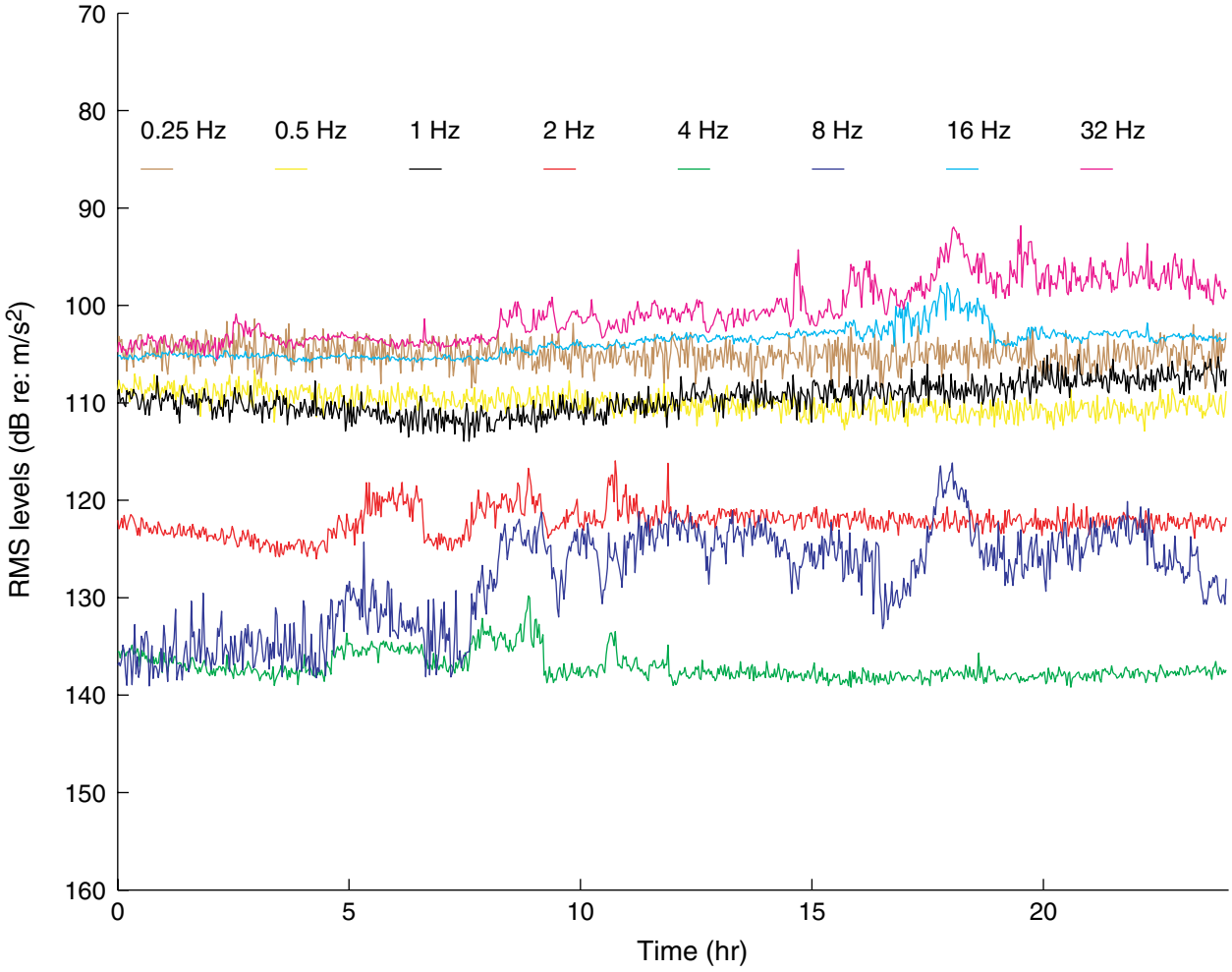

**Figure F26.** RMS energy levels in octave bands centered at the frequencies indicated for day 364 in 2001.

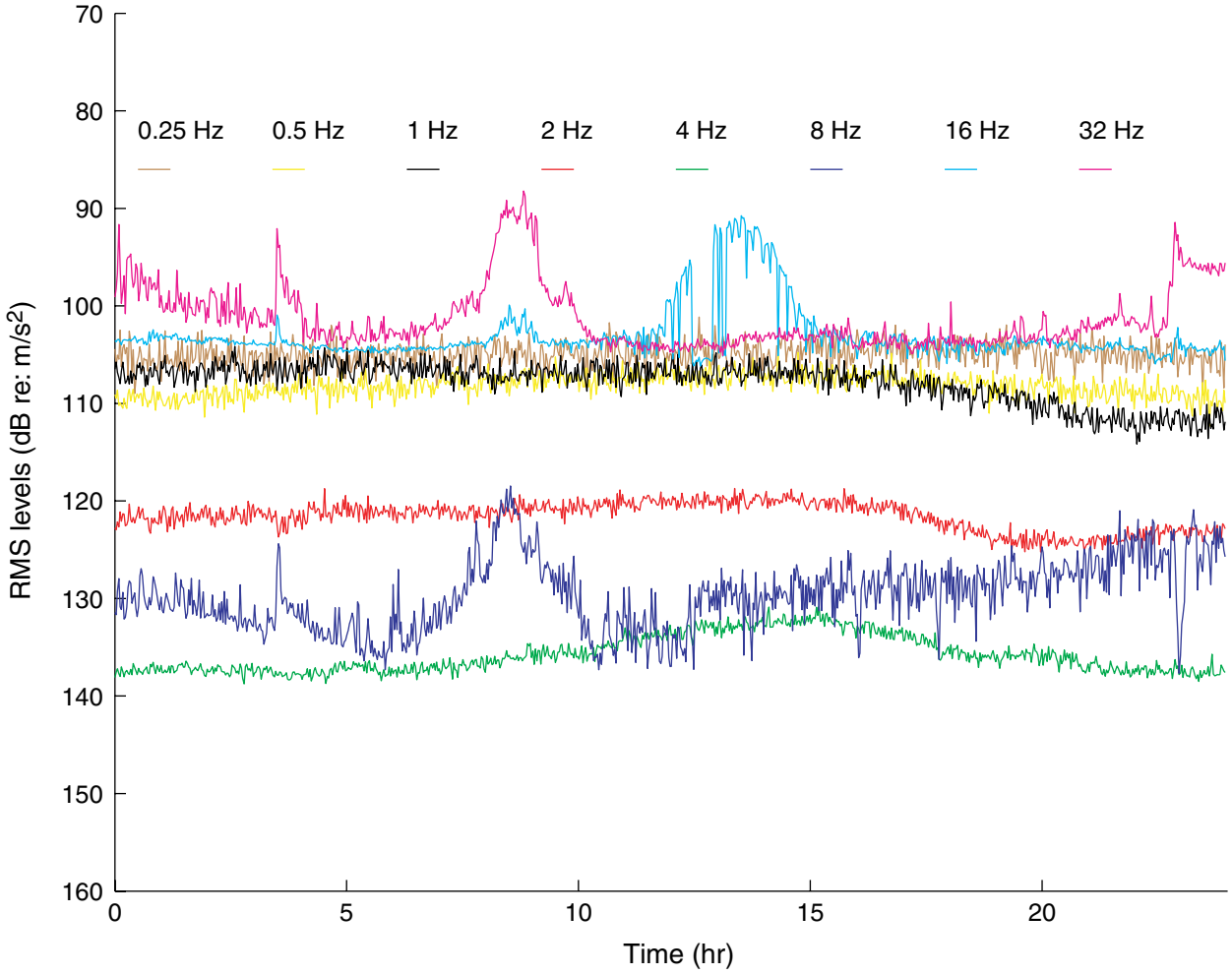

**Figure F27.** RMS energy levels in octave bands centered at the frequencies indicated for day 365 in 2001.

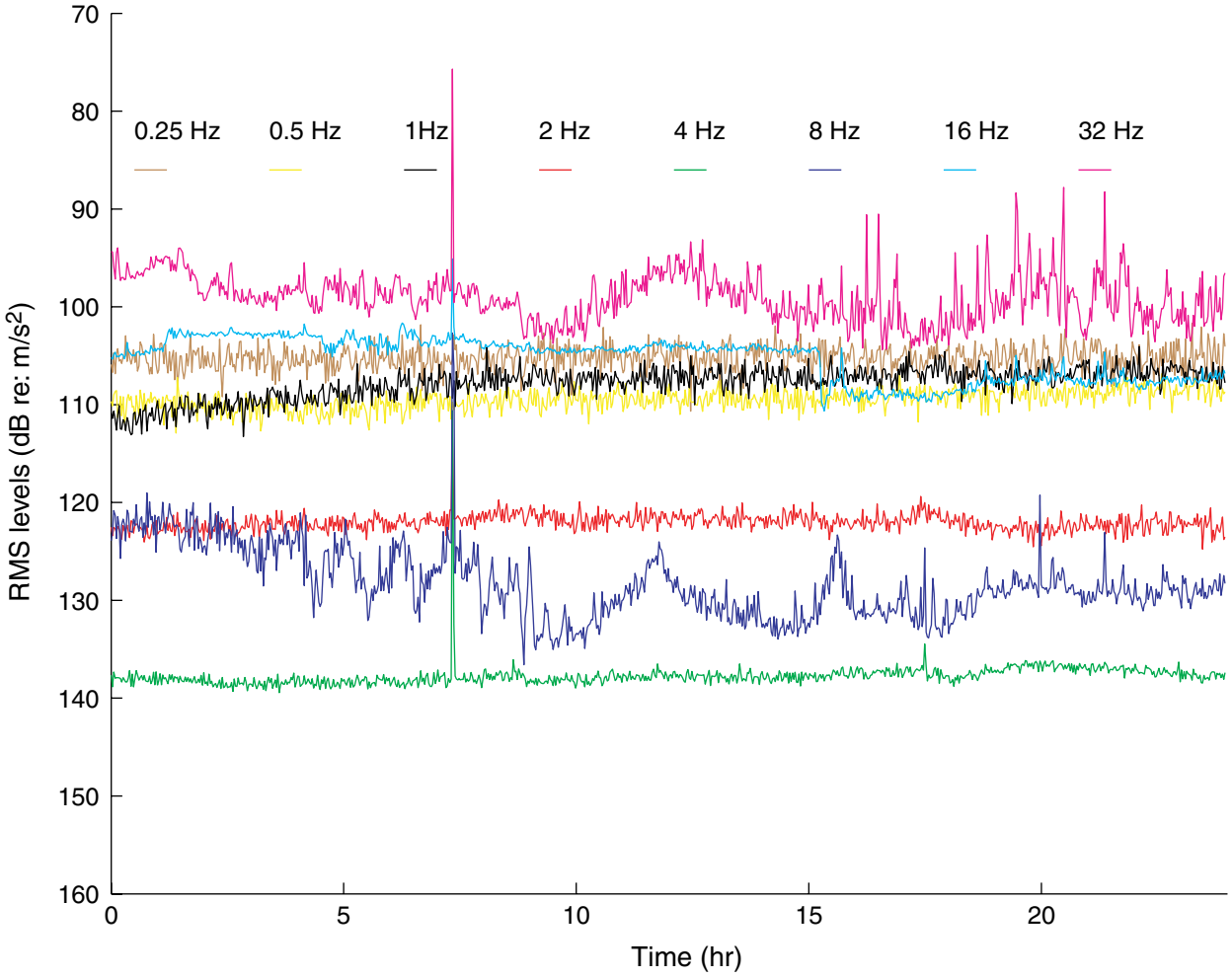

**Figure F28.** RMS energy levels in octave bands centered at the frequencies indicated for day 1 in 2002.

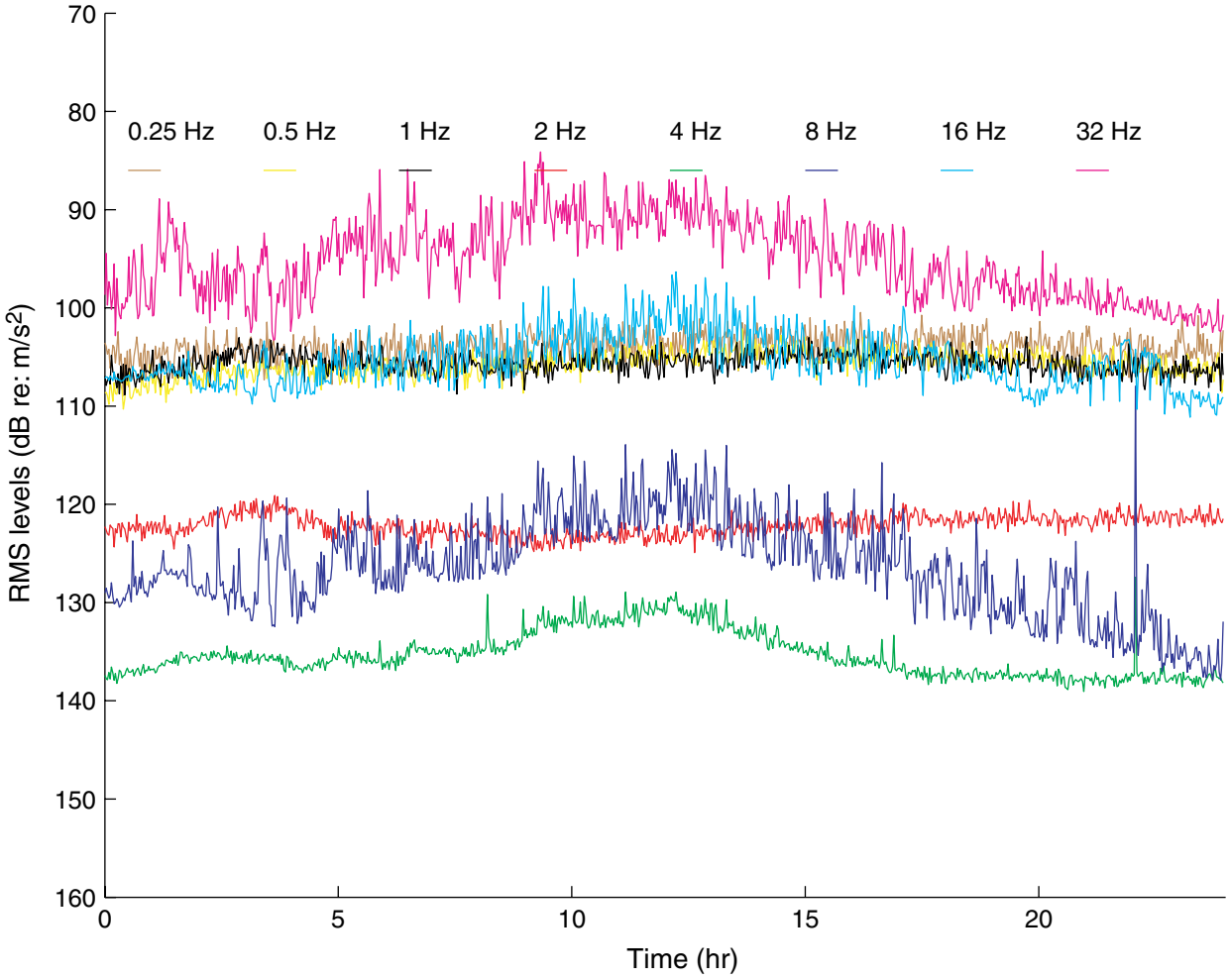

**Figure F29.** RMS energy levels in octave bands centered at the frequencies indicated for day 2 in 2002.

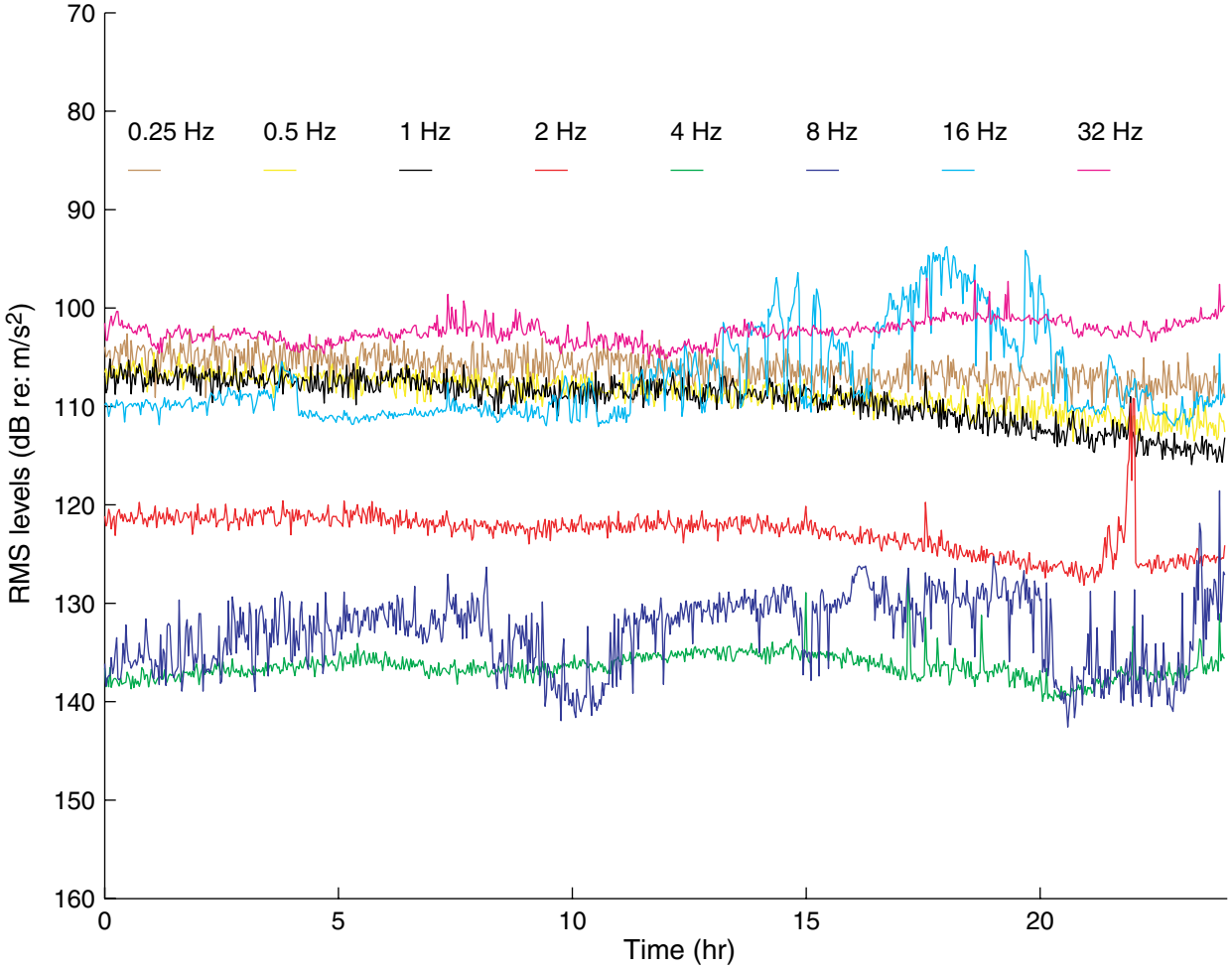

**Figure F30.** RMS energy levels in octave bands centered at the frequencies indicated for day 3 in 2002.

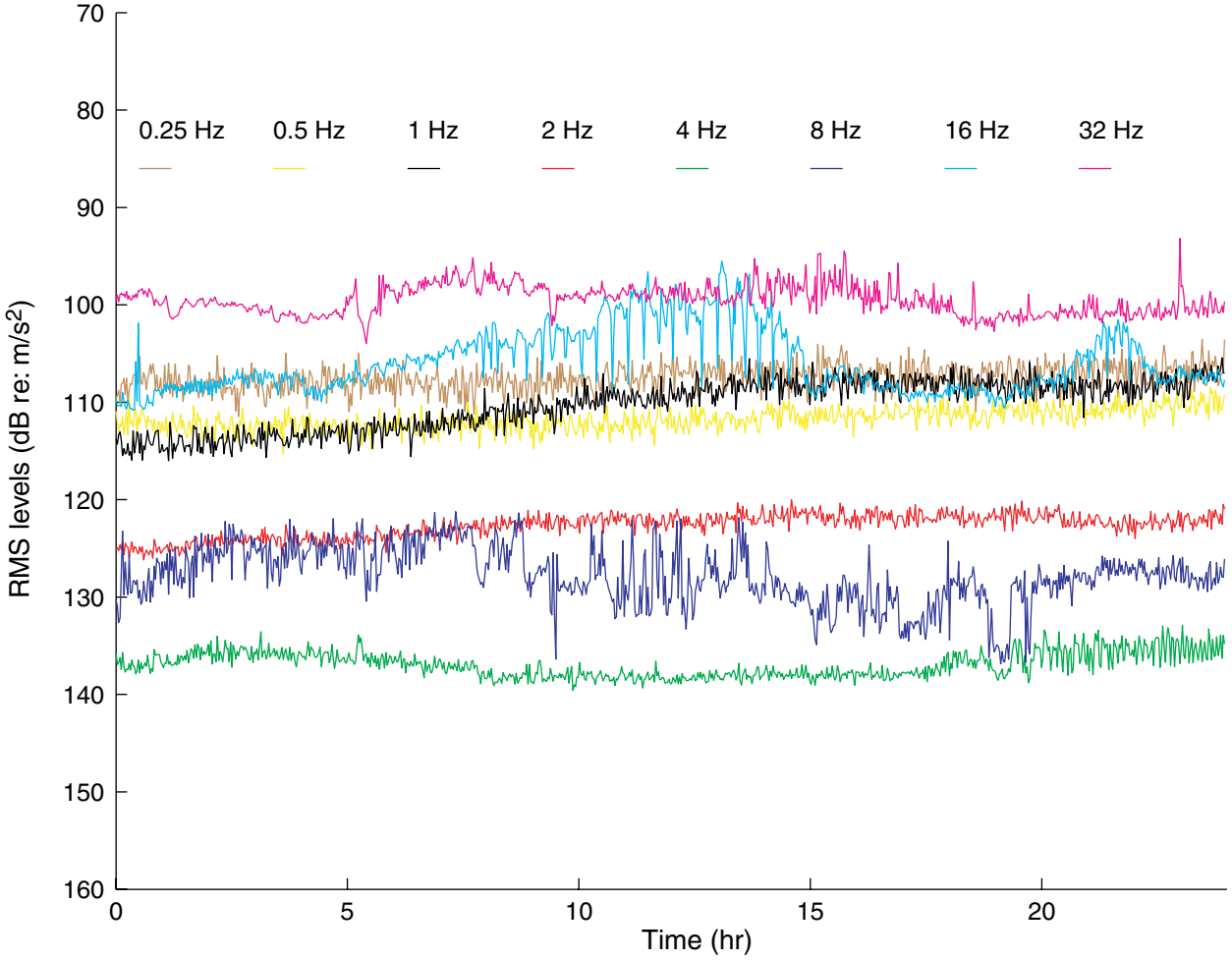

**Figure F31.** RMS energy levels in octave bands centered at the frequencies indicated for day 4 in 2002.

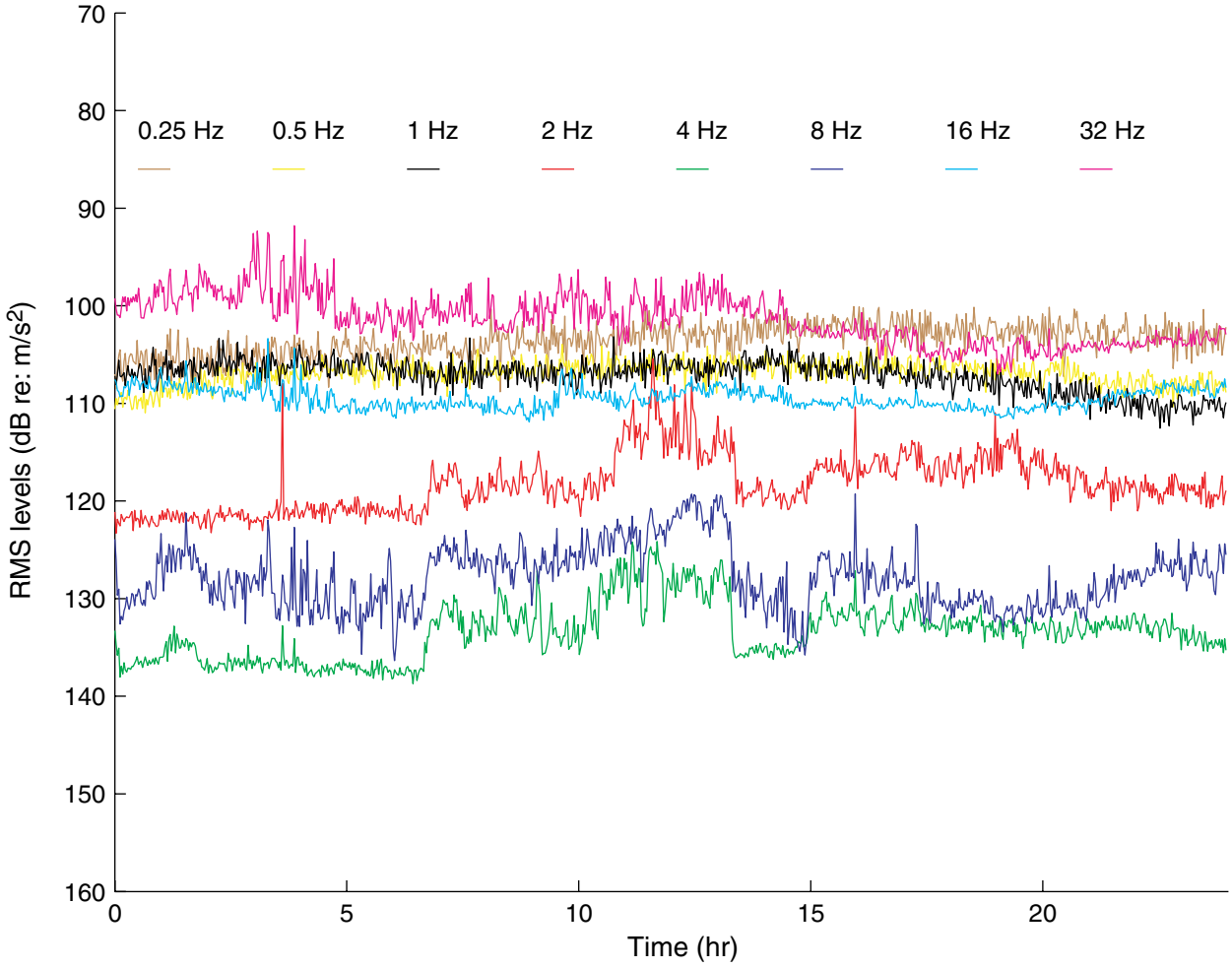

**Figure F32.** RMS energy levels in octave bands centered at the frequencies indicated for day 5 in 2002.

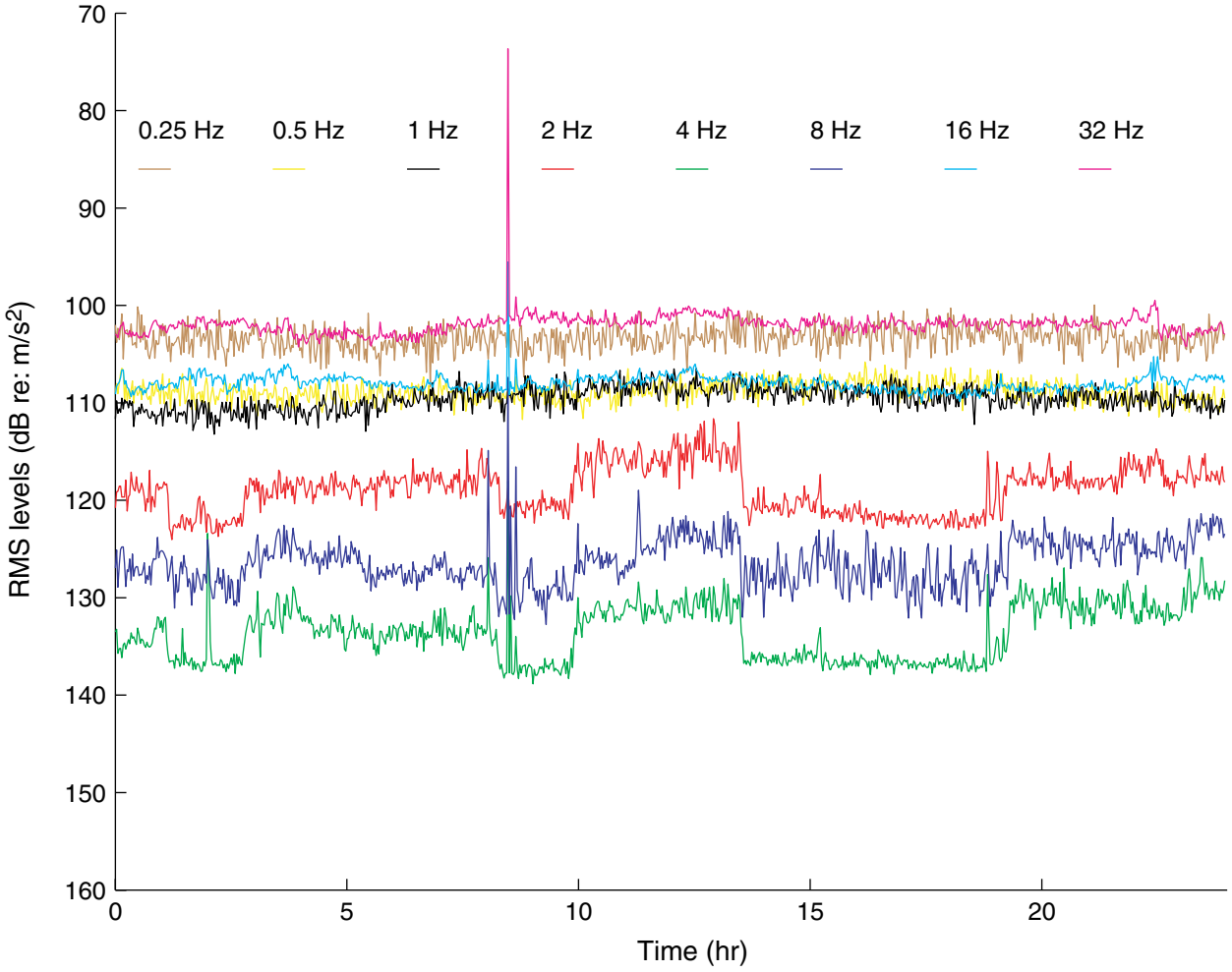

**Figure F33.** RMS energy levels in octave bands centered at the frequencies indicated for day 6 in 2002.

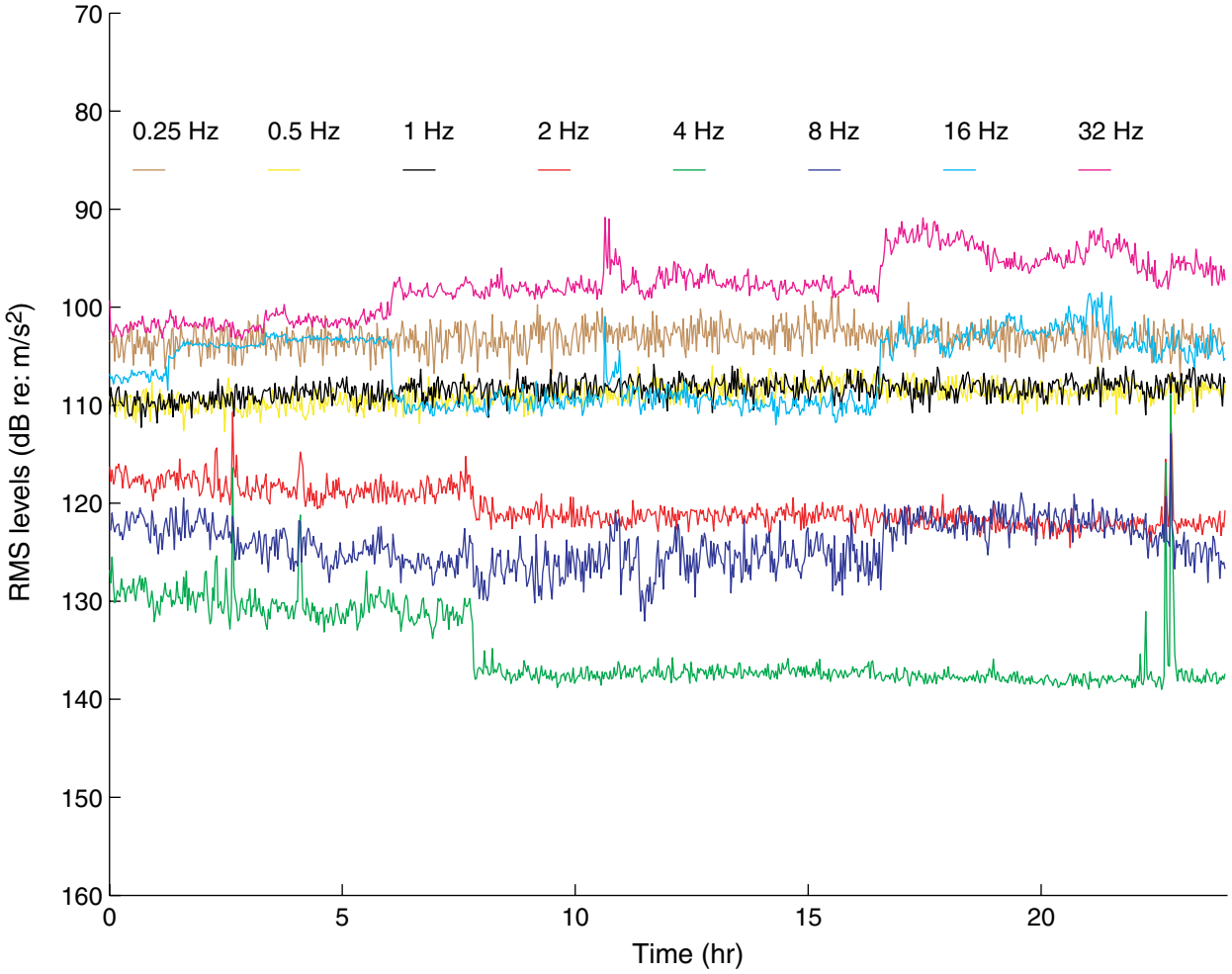

**Figure F34.** RMS energy levels in octave bands centered at the frequencies indicated for day 7 in 2002.

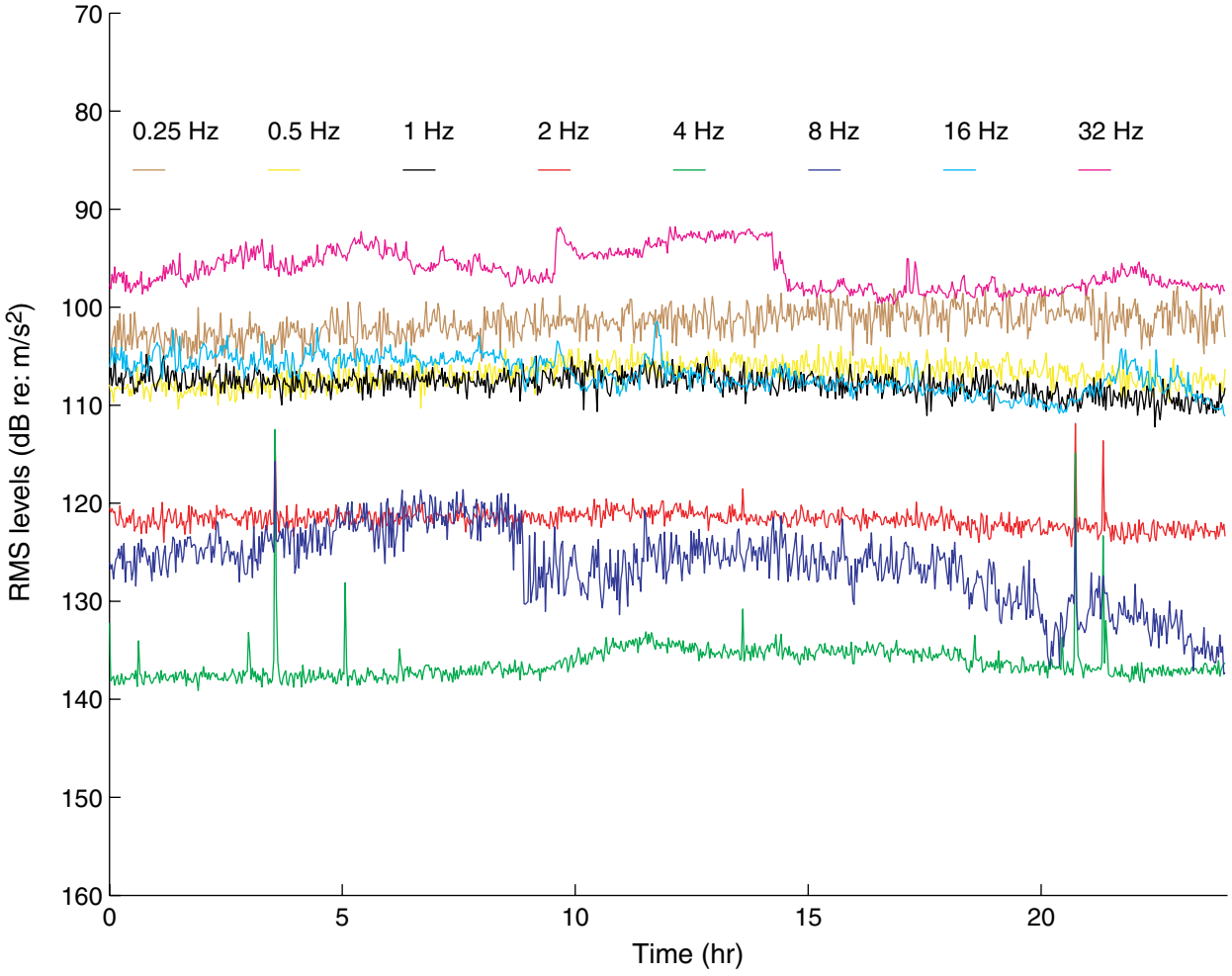

**Figure F35.** RMS energy levels in octave bands centered at the frequencies indicated for day 8 in 2002.

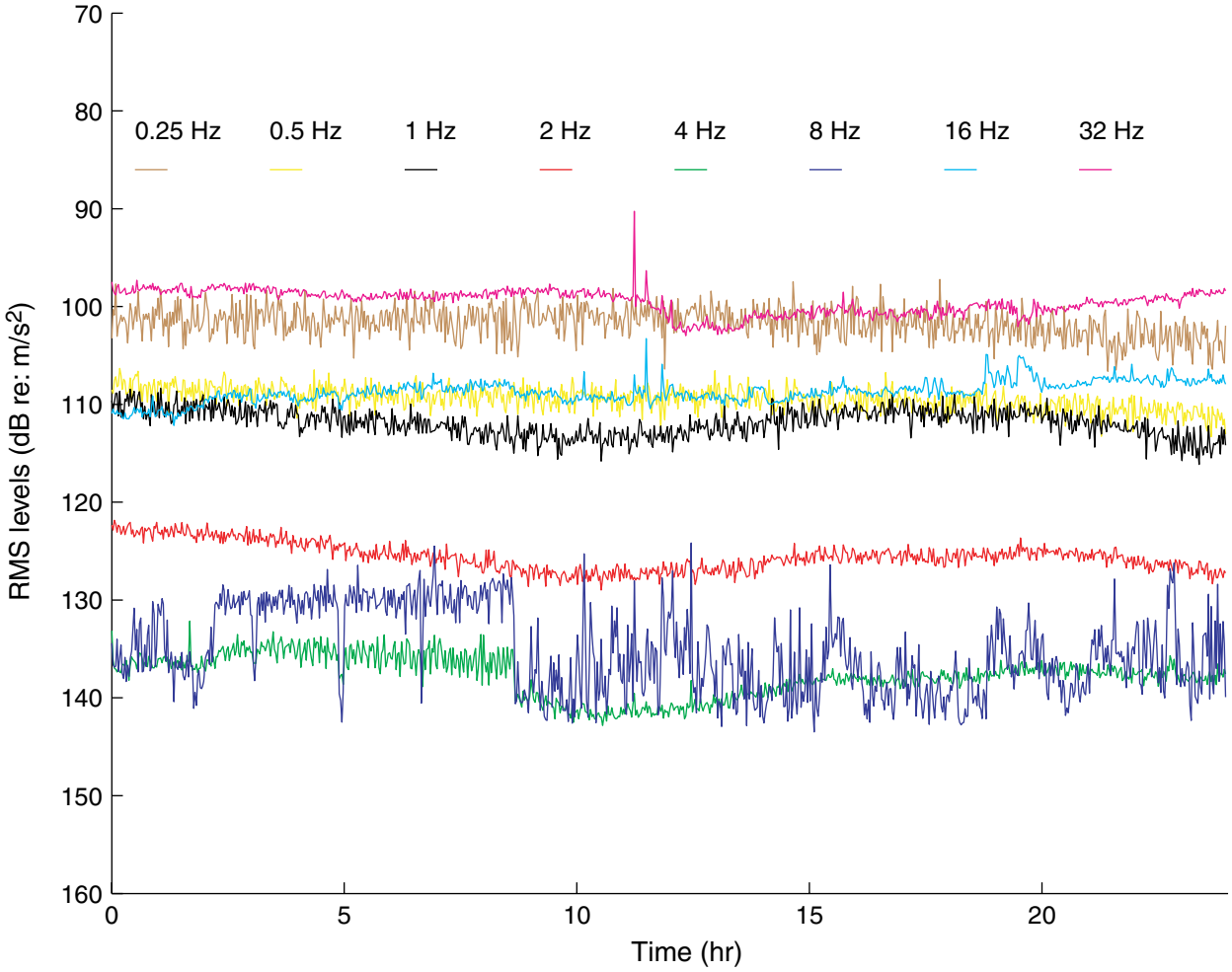

**Figure F36.** RMS energy levels in octave bands centered at the frequencies indicated for day 9 in 2002.

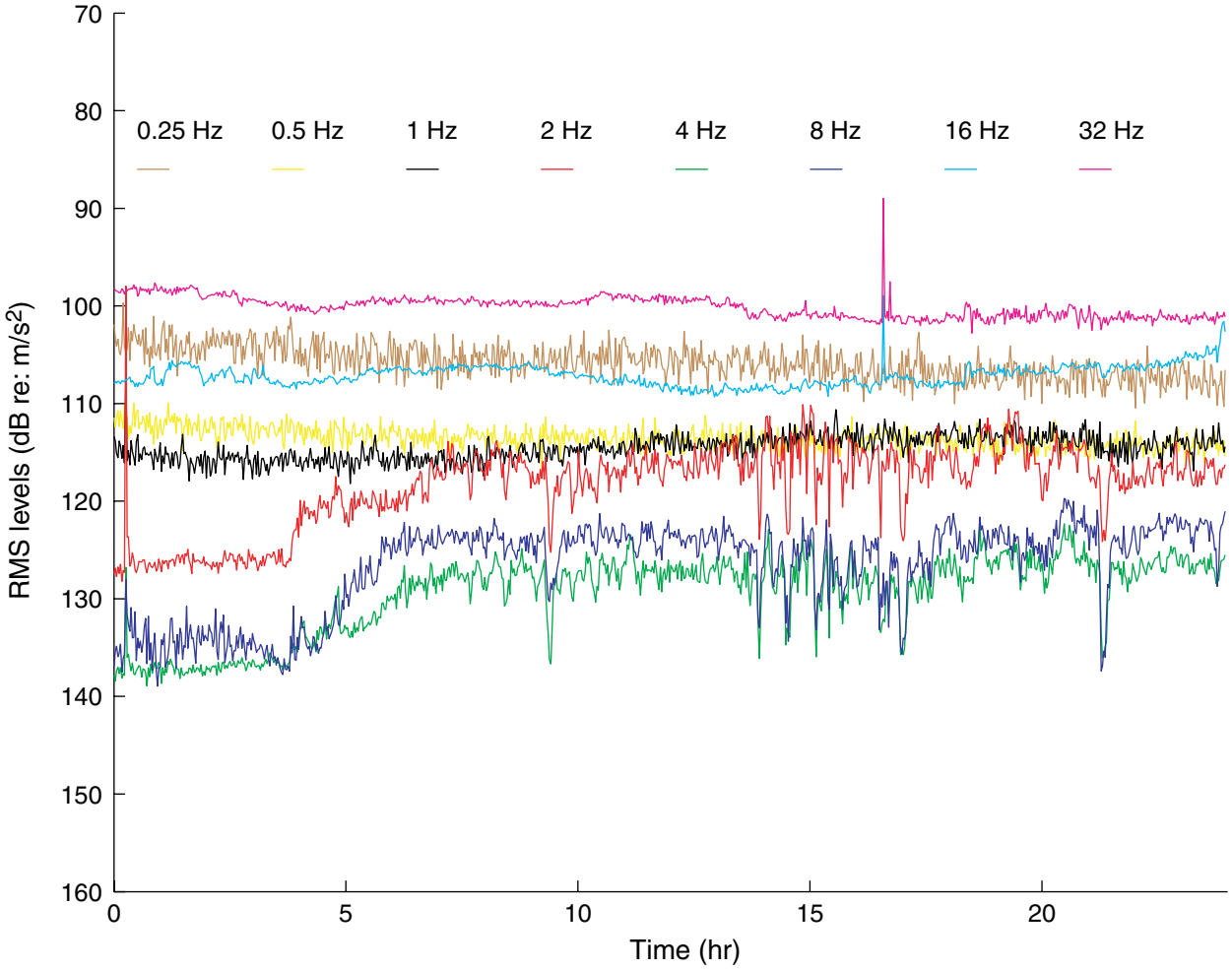

**Figure F37.** RMS energy levels in octave bands centered at the frequencies indicated for day 10 in 2002.

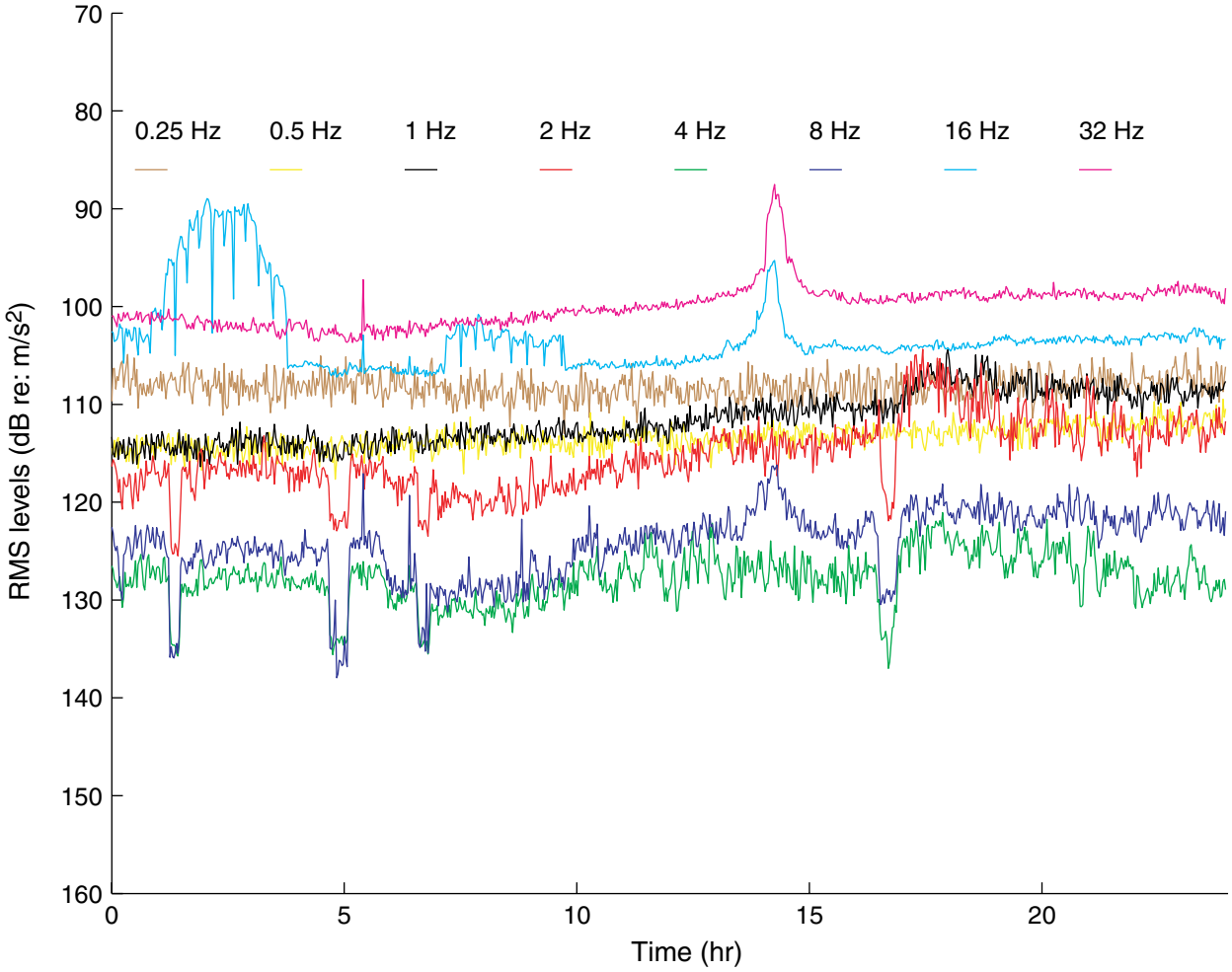

**Figure F38.** RMS energy levels in octave bands centered at the frequencies indicated for day 11 in 2002.

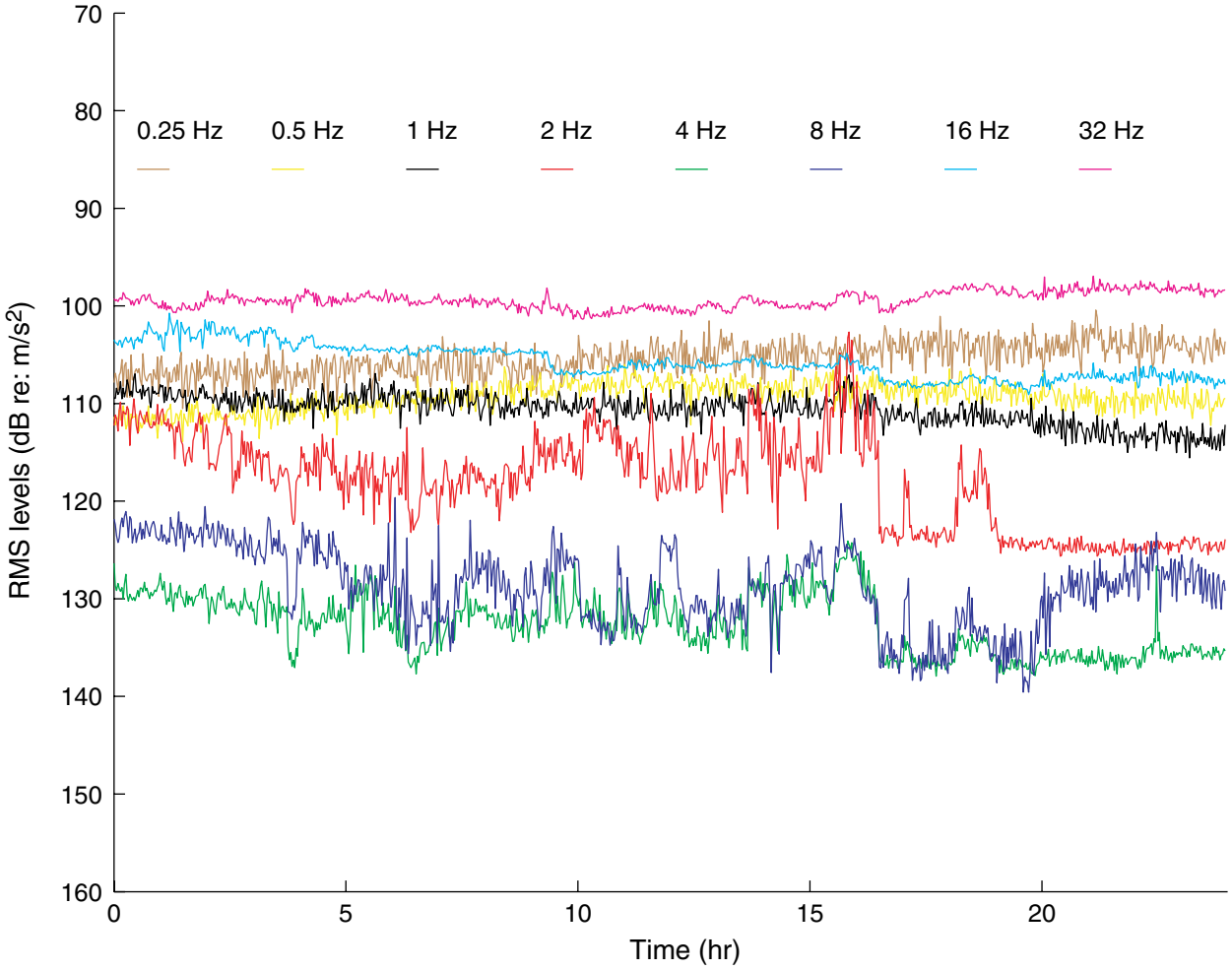

**Figure F39.** RMS energy levels in octave bands centered at the frequencies indicated for day 12 in 2002.

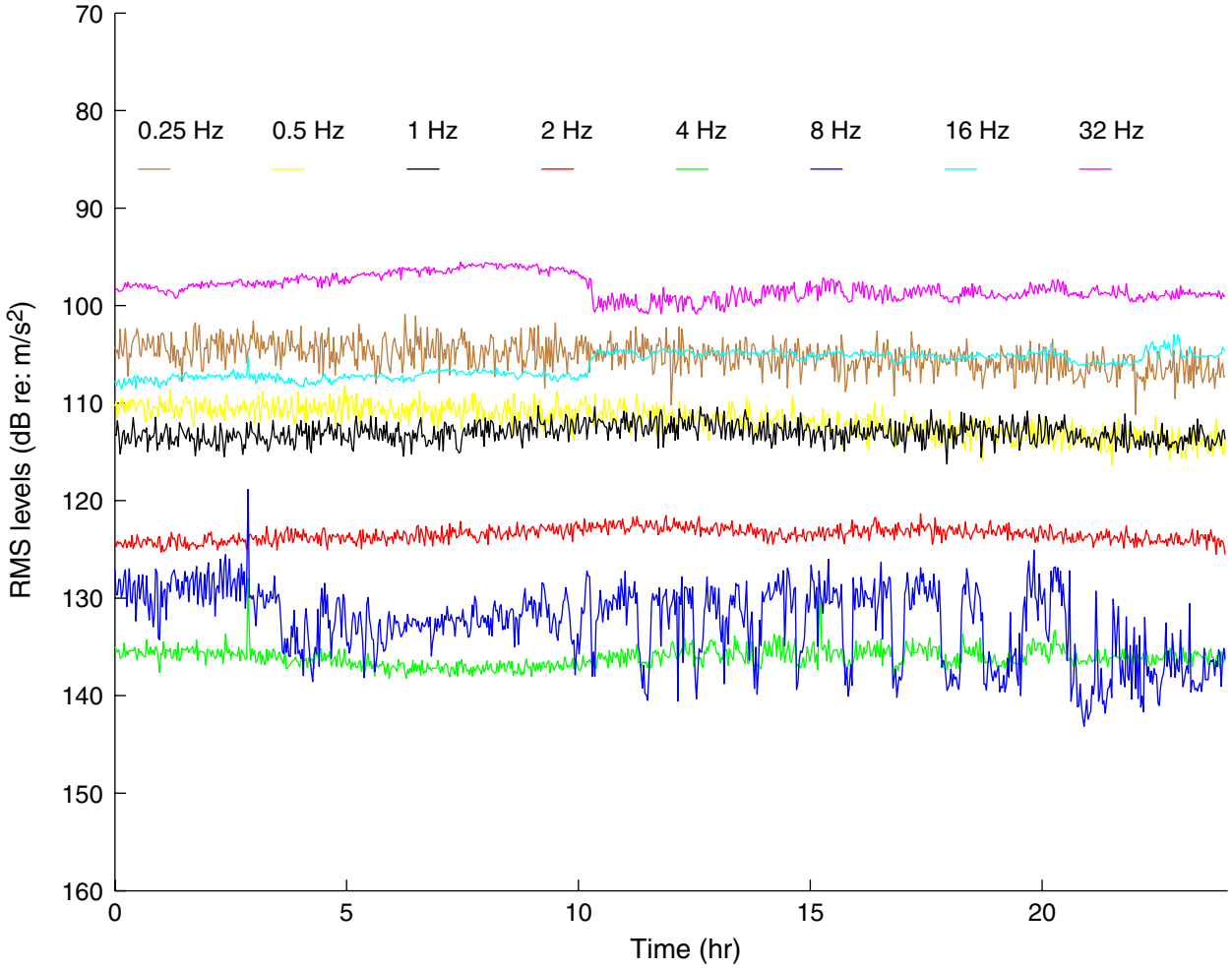

**Figure F40.** RMS energy levels in octave bands centered at the frequencies indicated for day 13 In 2002.

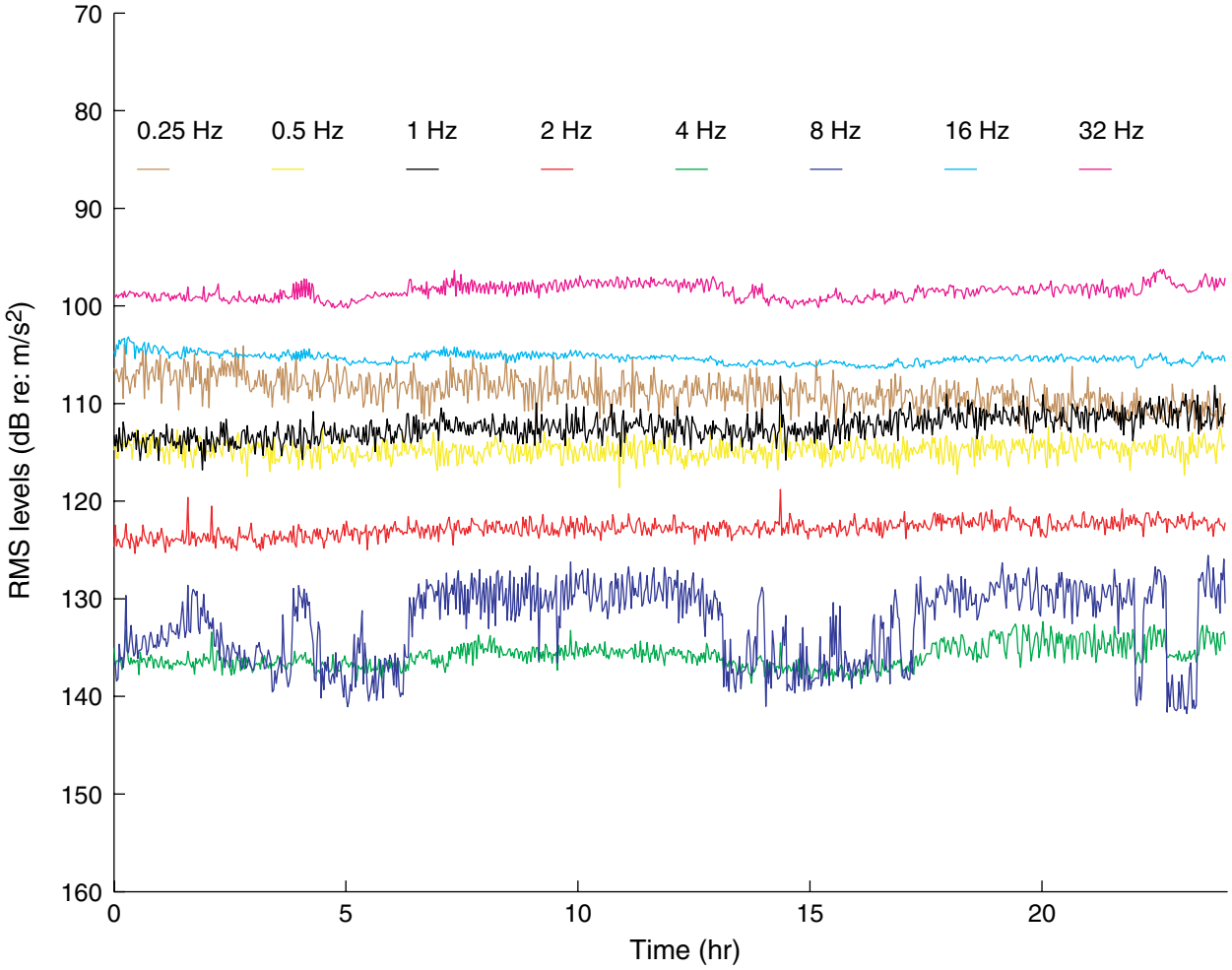

**Figure F41.** RMS energy levels in octave bands centered at the frequencies indicated for day 14 in 2002.

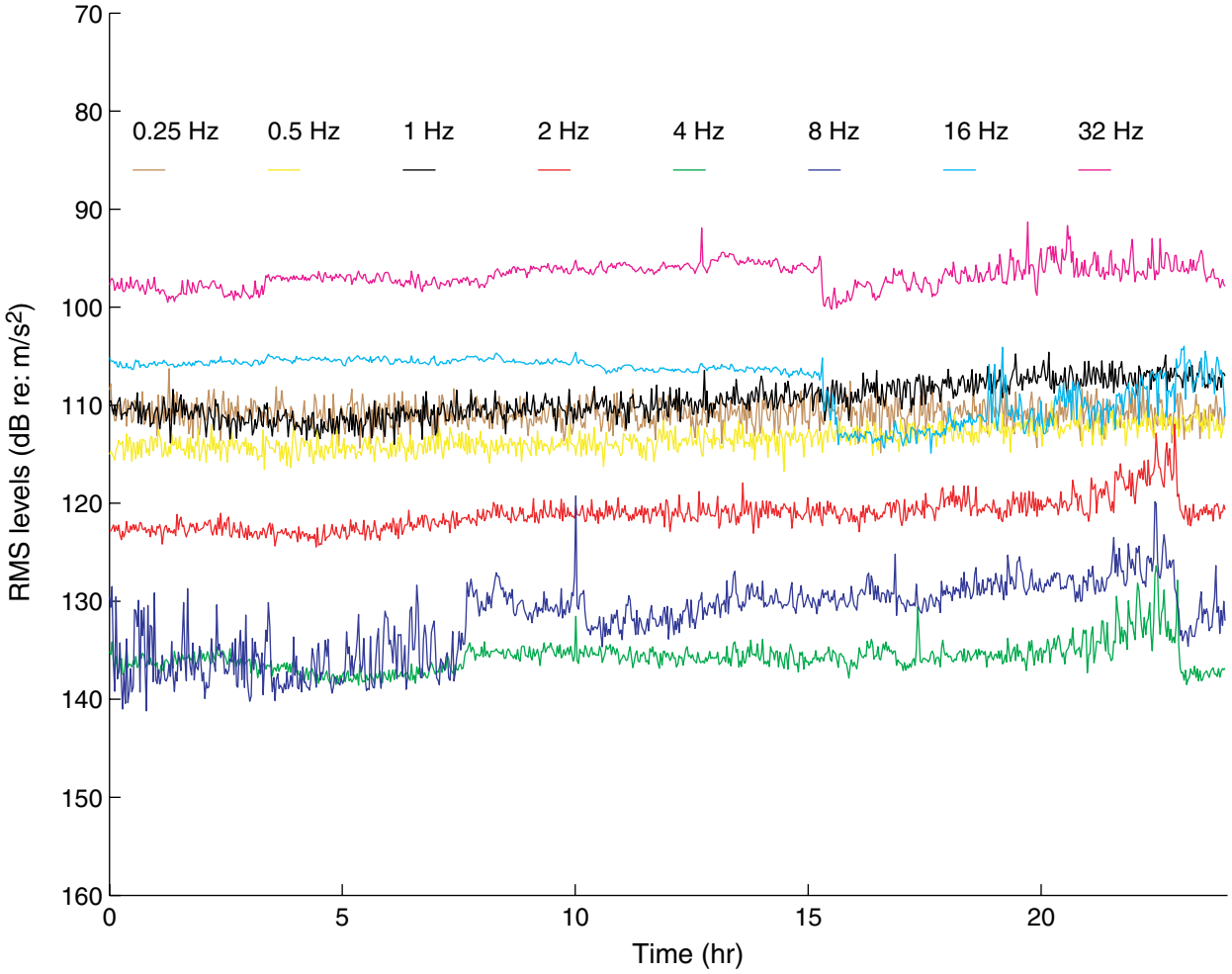

**Figure F42.** RMS energy levels in octave bands centered at the frequencies indicated for day 15 in 2002.

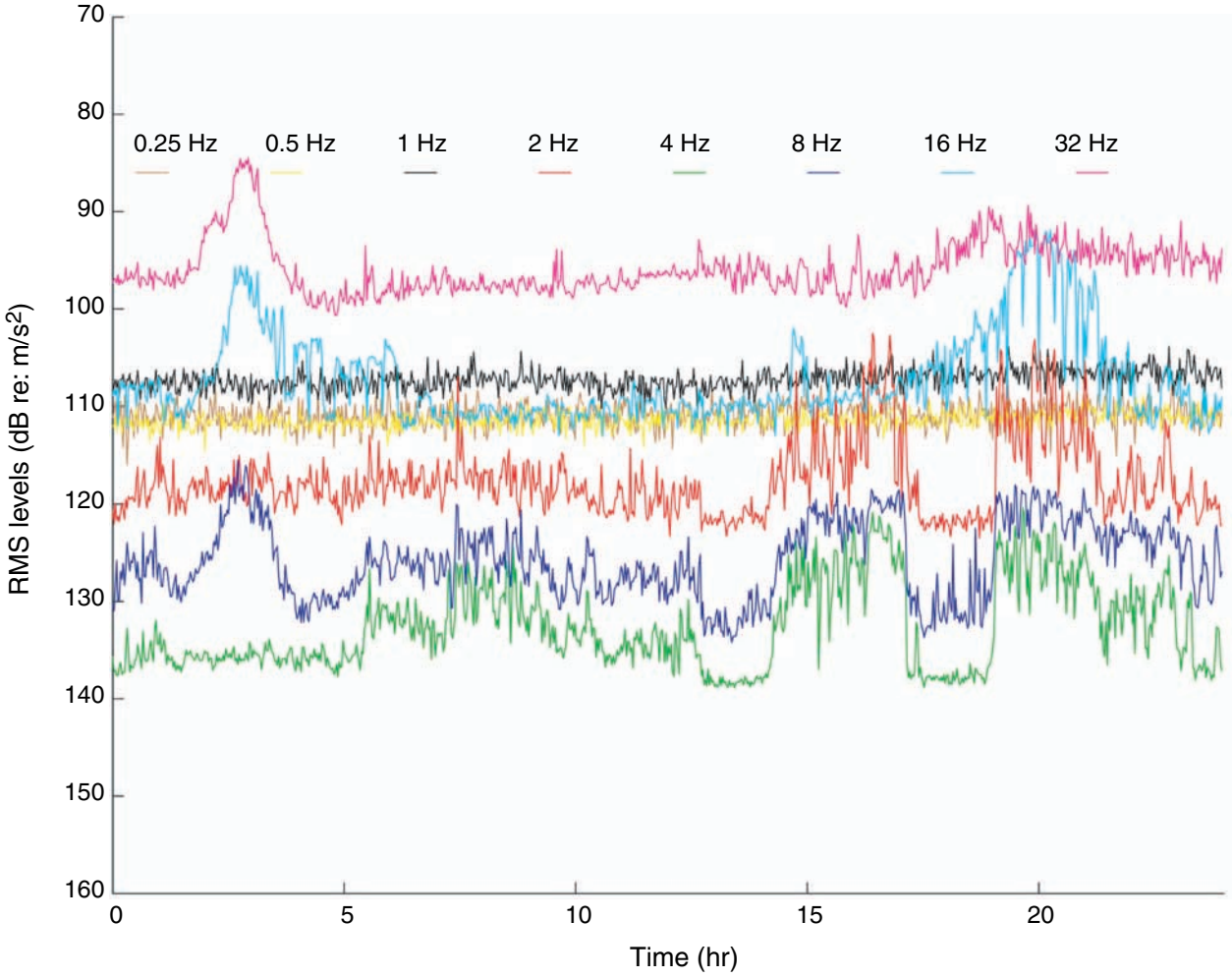

**Figure F43.** RMS energy levels in octave bands centered at the frequencies indicated for day 16 in 2002.

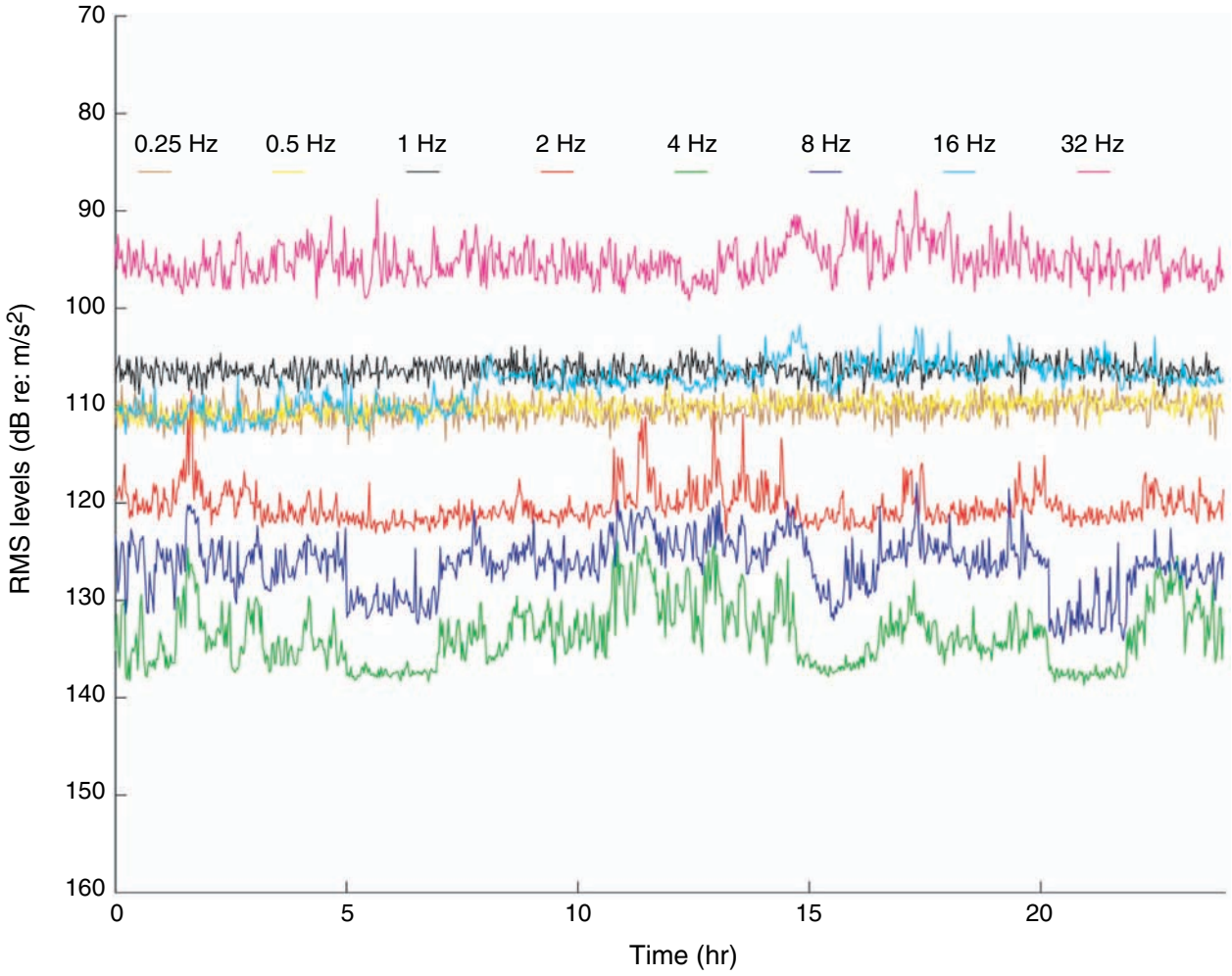

**Figure F44.** RMS energy levels in octave bands centered at the frequencies indicated for day 17 in 2002.

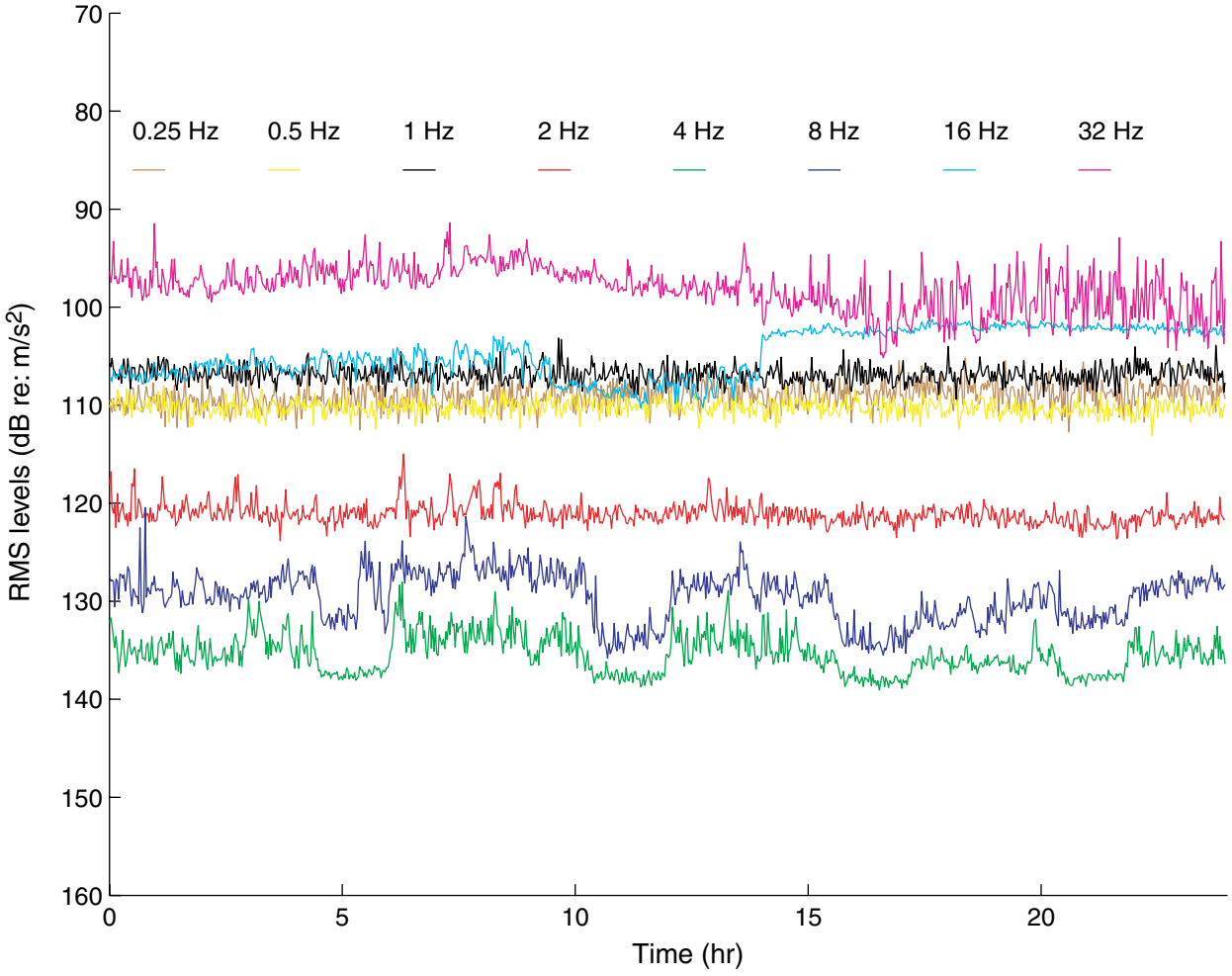

**Figure F45.** RMS energy levels in octave bands centered at the frequencies indicated for day 18 in 2002.

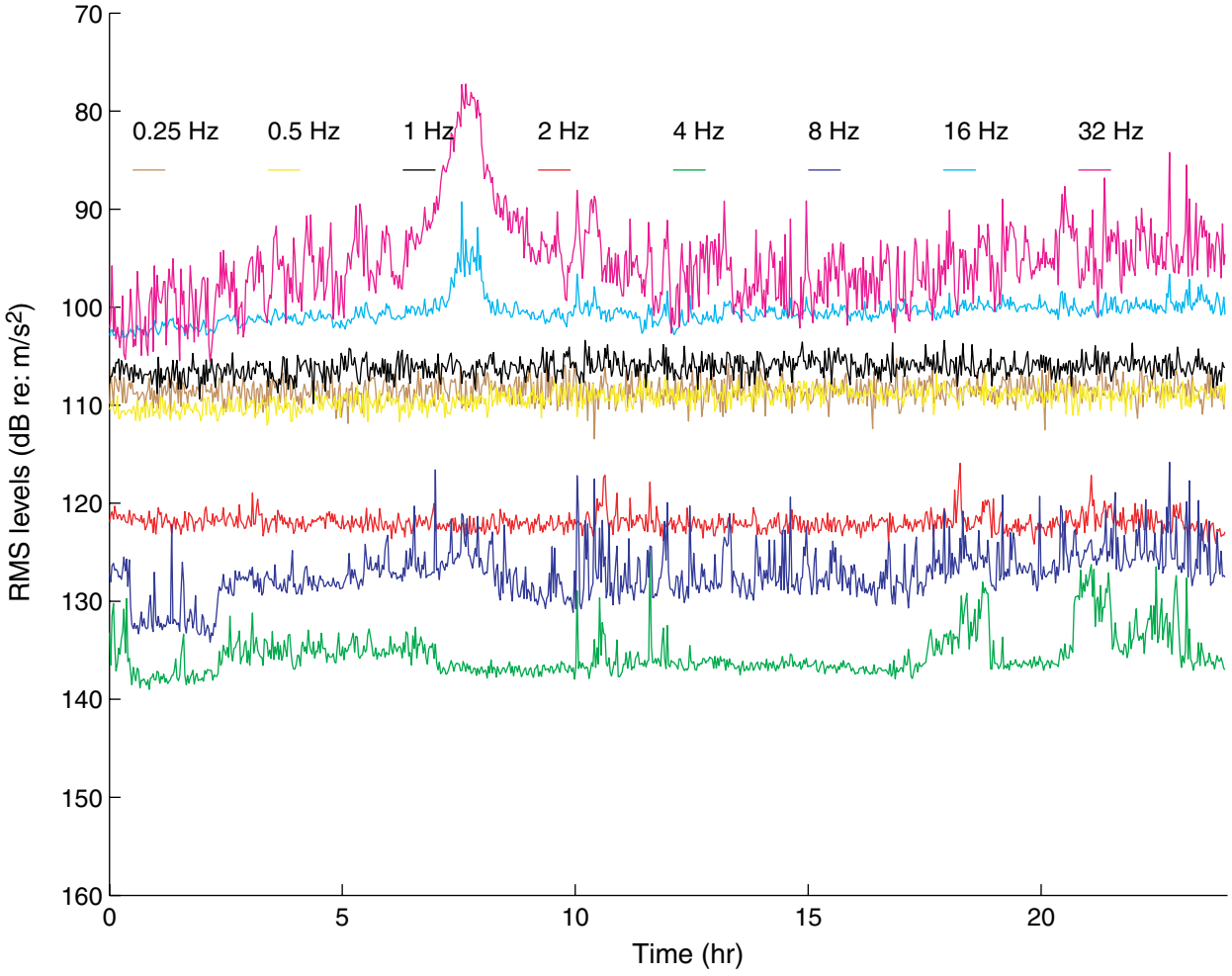

**Figure F46.** RMS energy levels in octave bands centered at the frequencies indicated for day 19 in 2002.

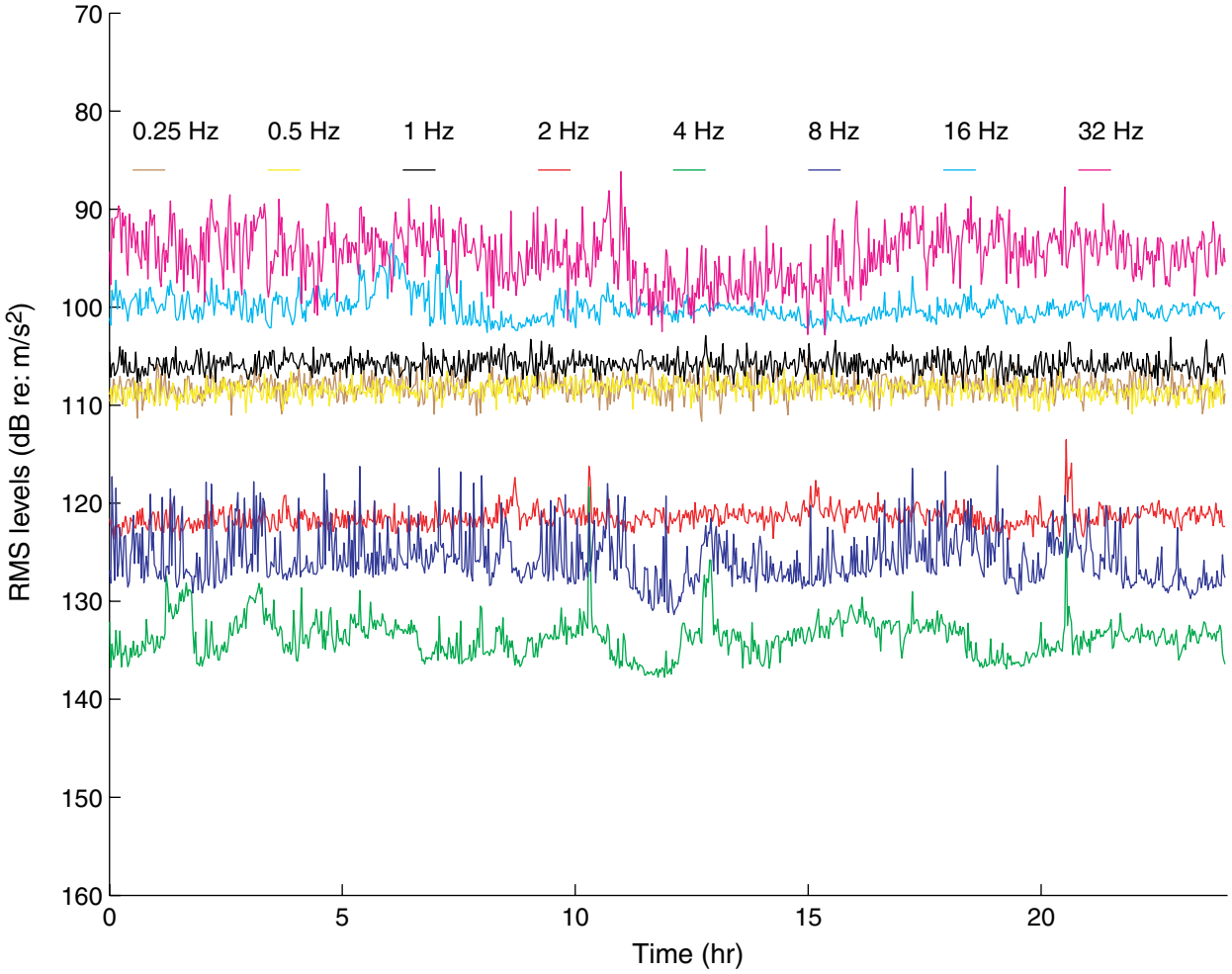

**Figure F47.** RMS energy levels in octave bands centered at the frequencies indicated for day 20 in 2002.

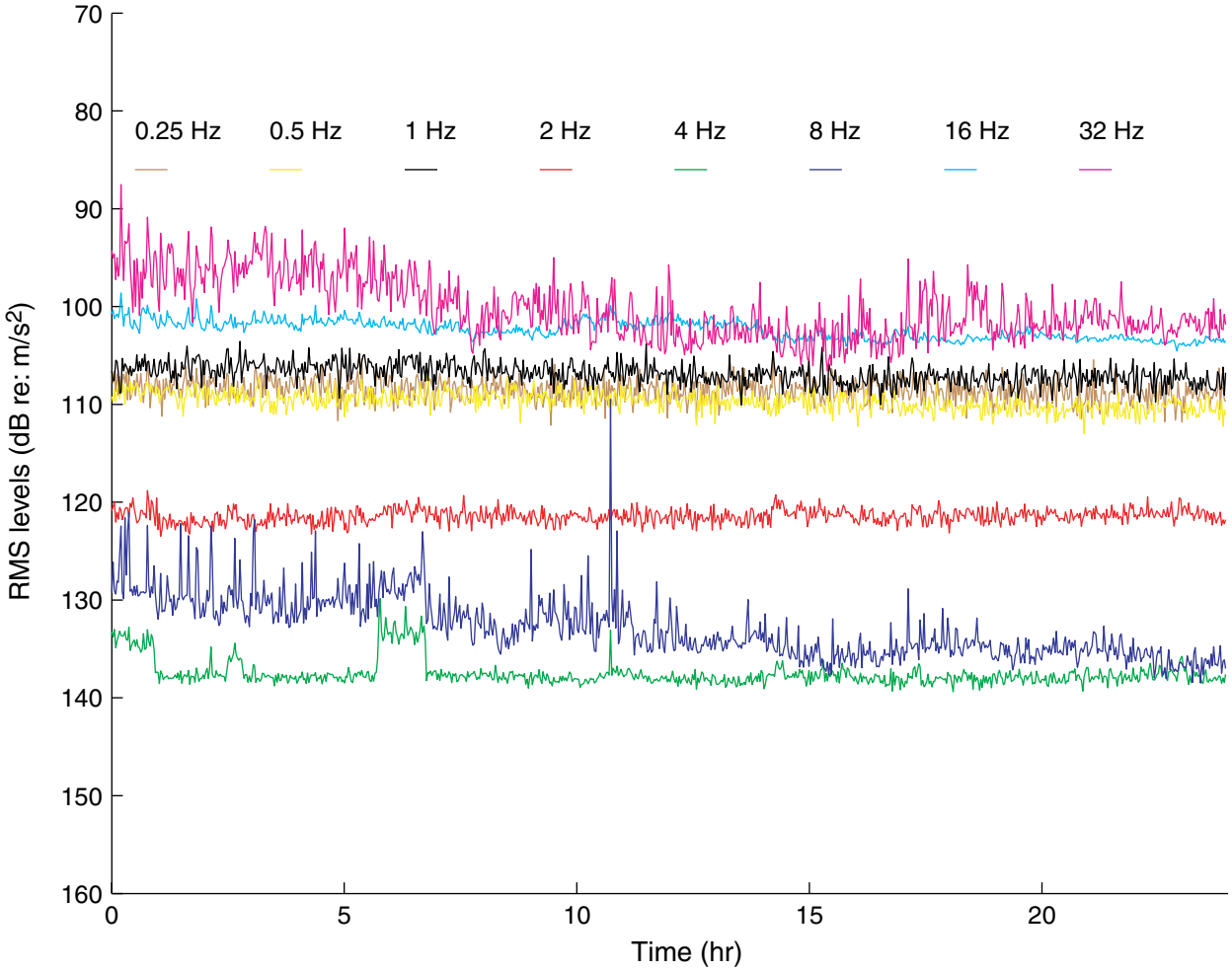

**Figure F48.** RMS energy levels in octave bands centered at the frequencies indicated for day 21 in 2002.

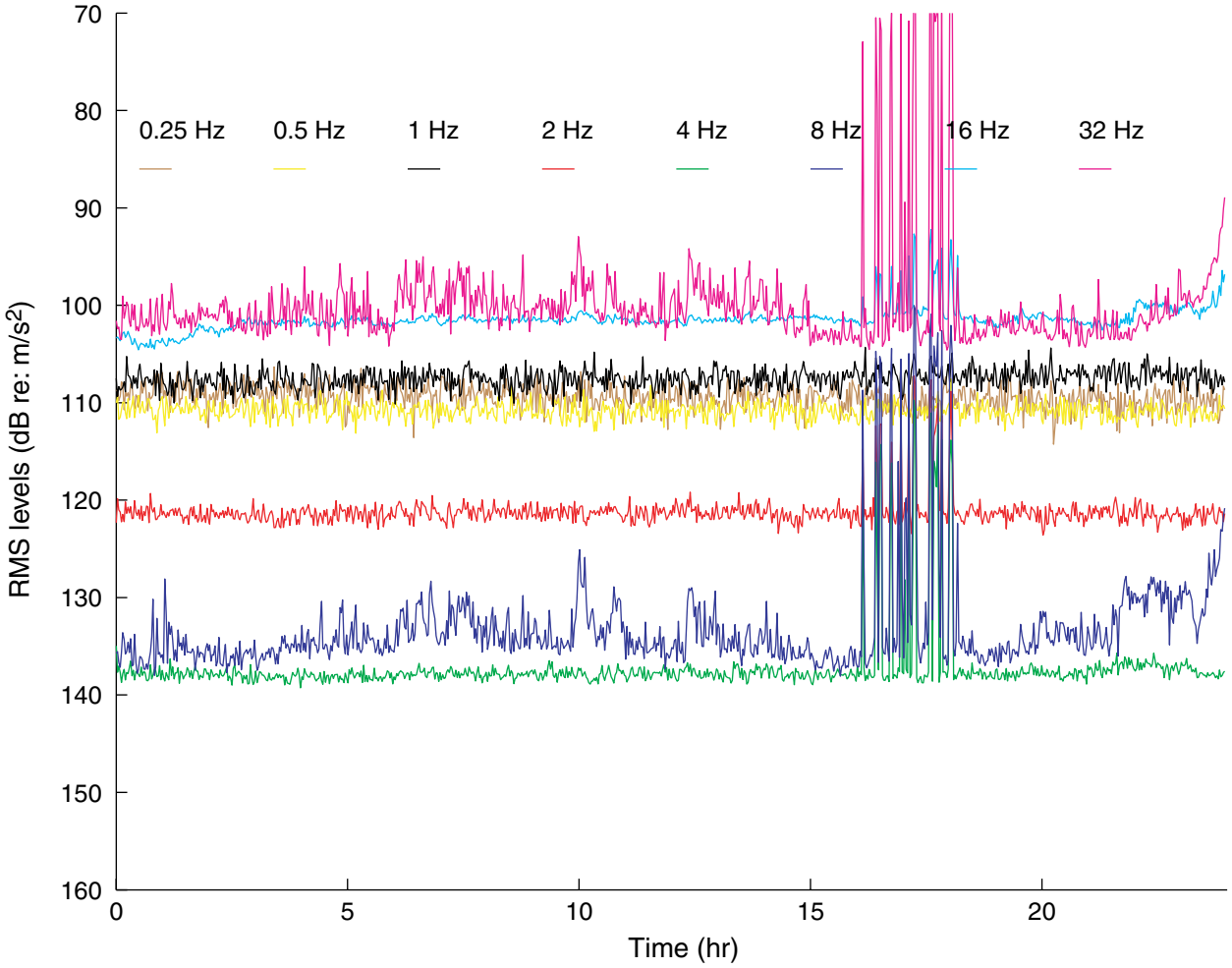

**Figure F49.** RMS energy levels in octave bands centered at the frequencies indicated for day 22 in 2002.

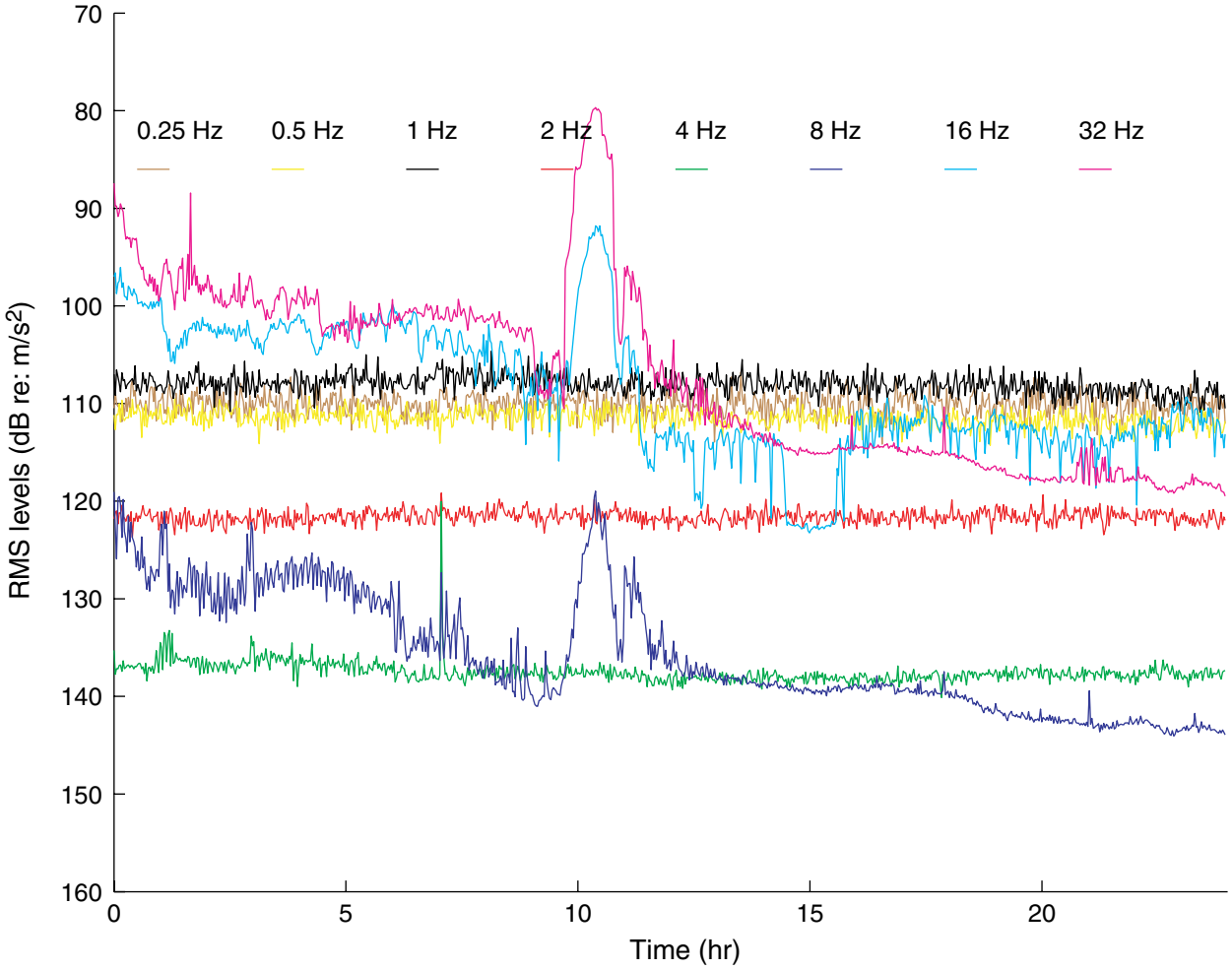

**Figure F50.** RMS energy levels in octave bands centered at the frequencies indicated for day 23 in 2002.

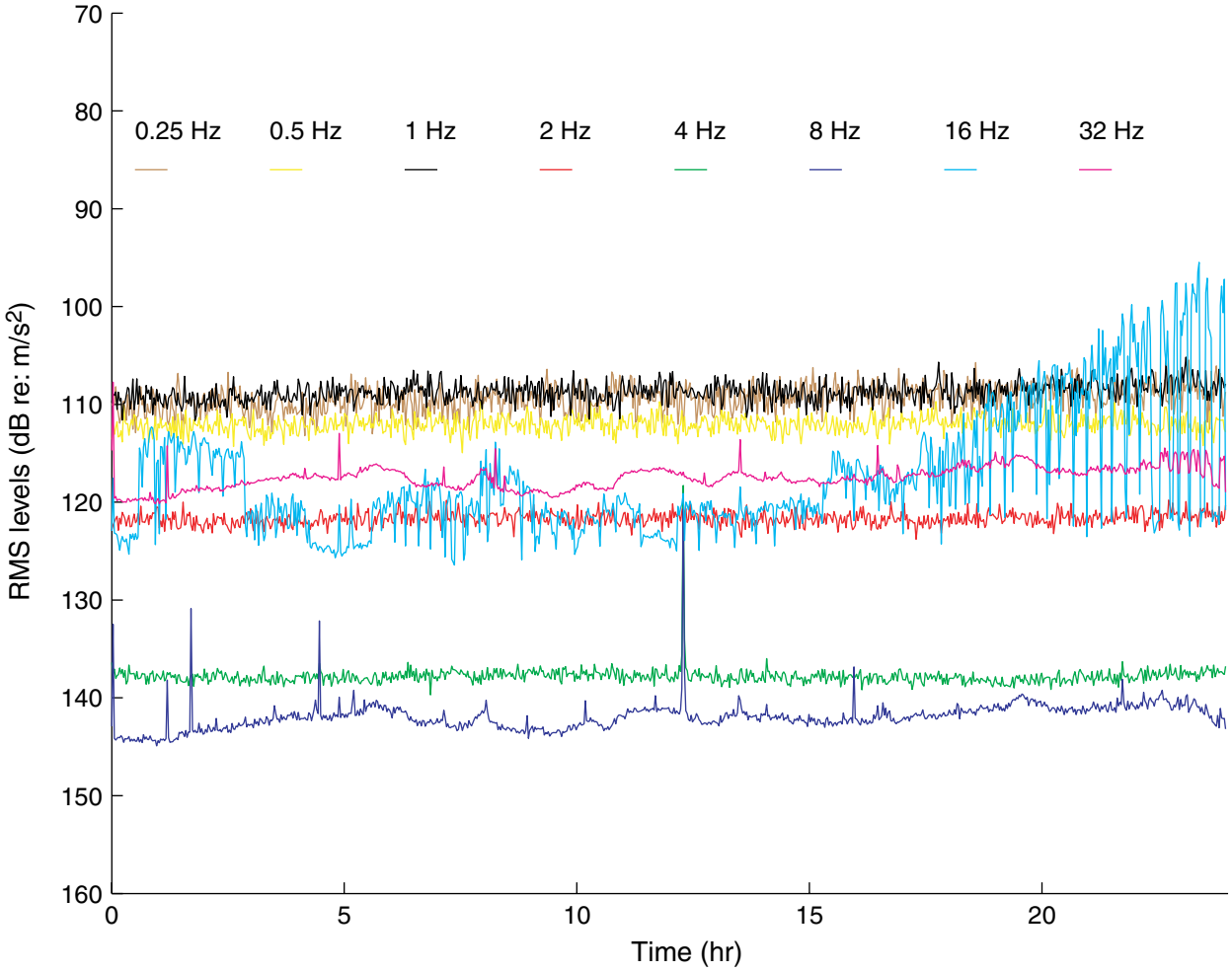

**Figure F51.** RMS energy levels in octave bands centered at the frequencies indicated for day 24 in 2002.

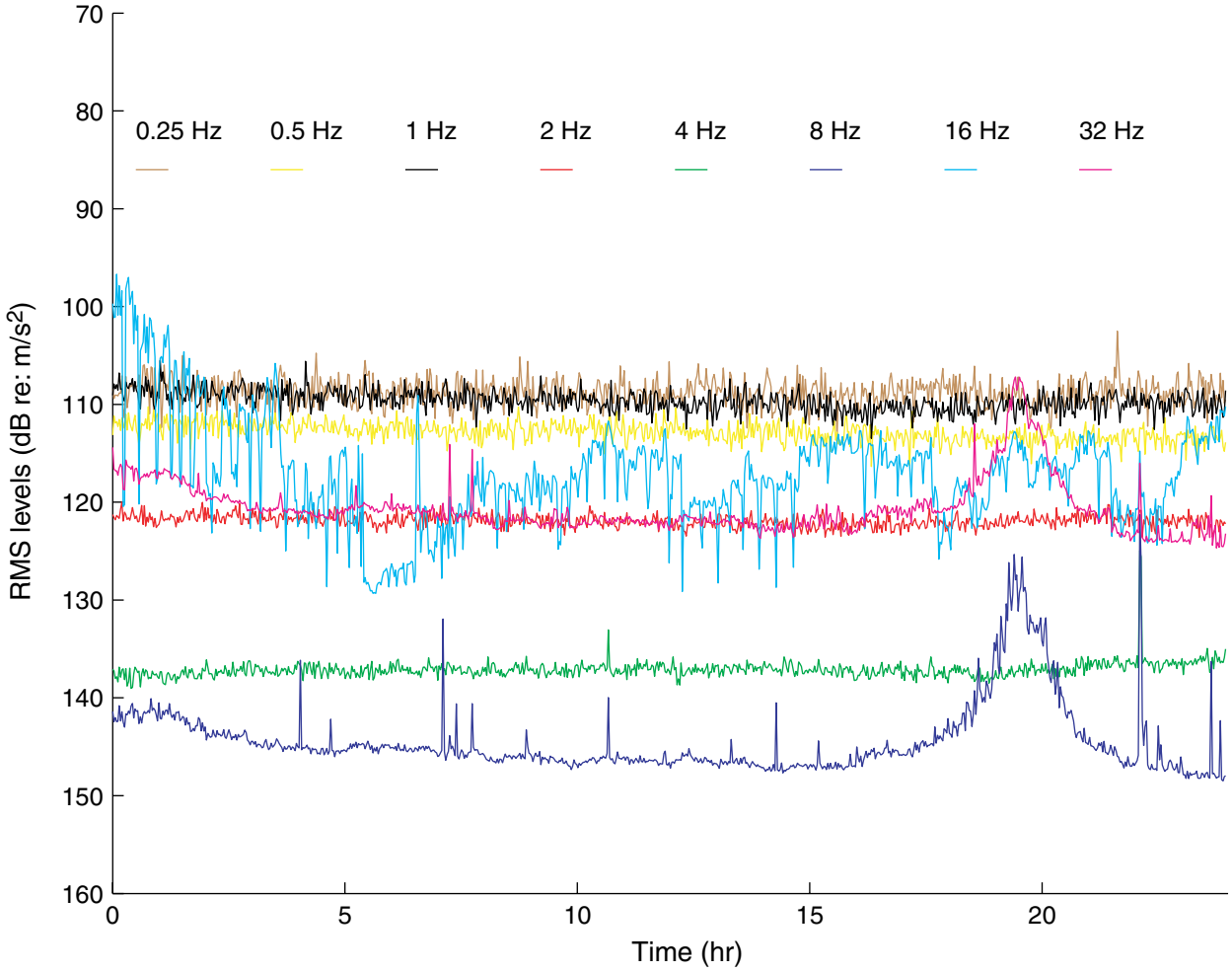

**Figure F52.** RMS energy levels in octave bands centered at the frequencies indicated for day 25 in 2002.

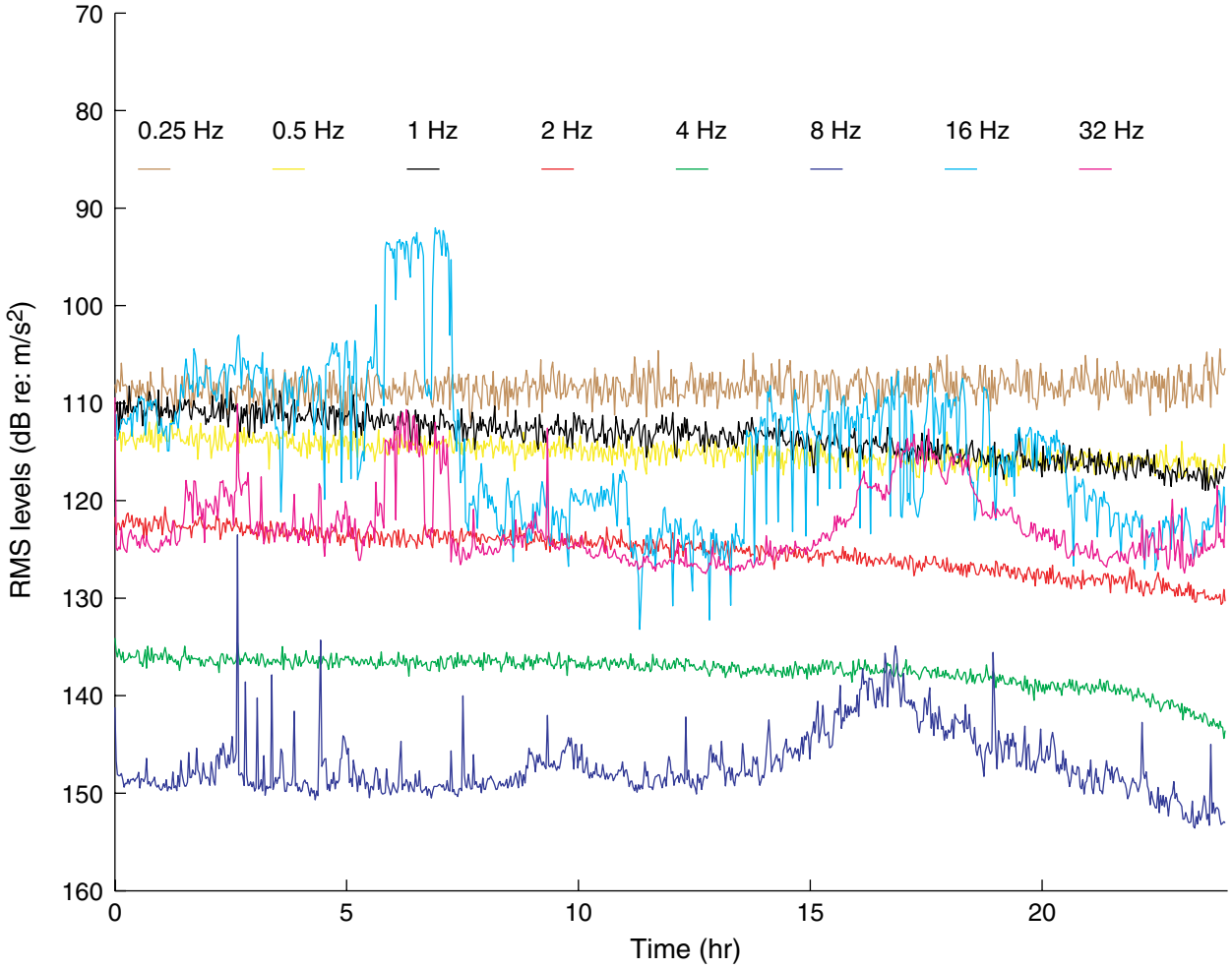

**Figure F53.** RMS energy levels in octave bands centered at the frequencies indicated for day 26 in 2002.

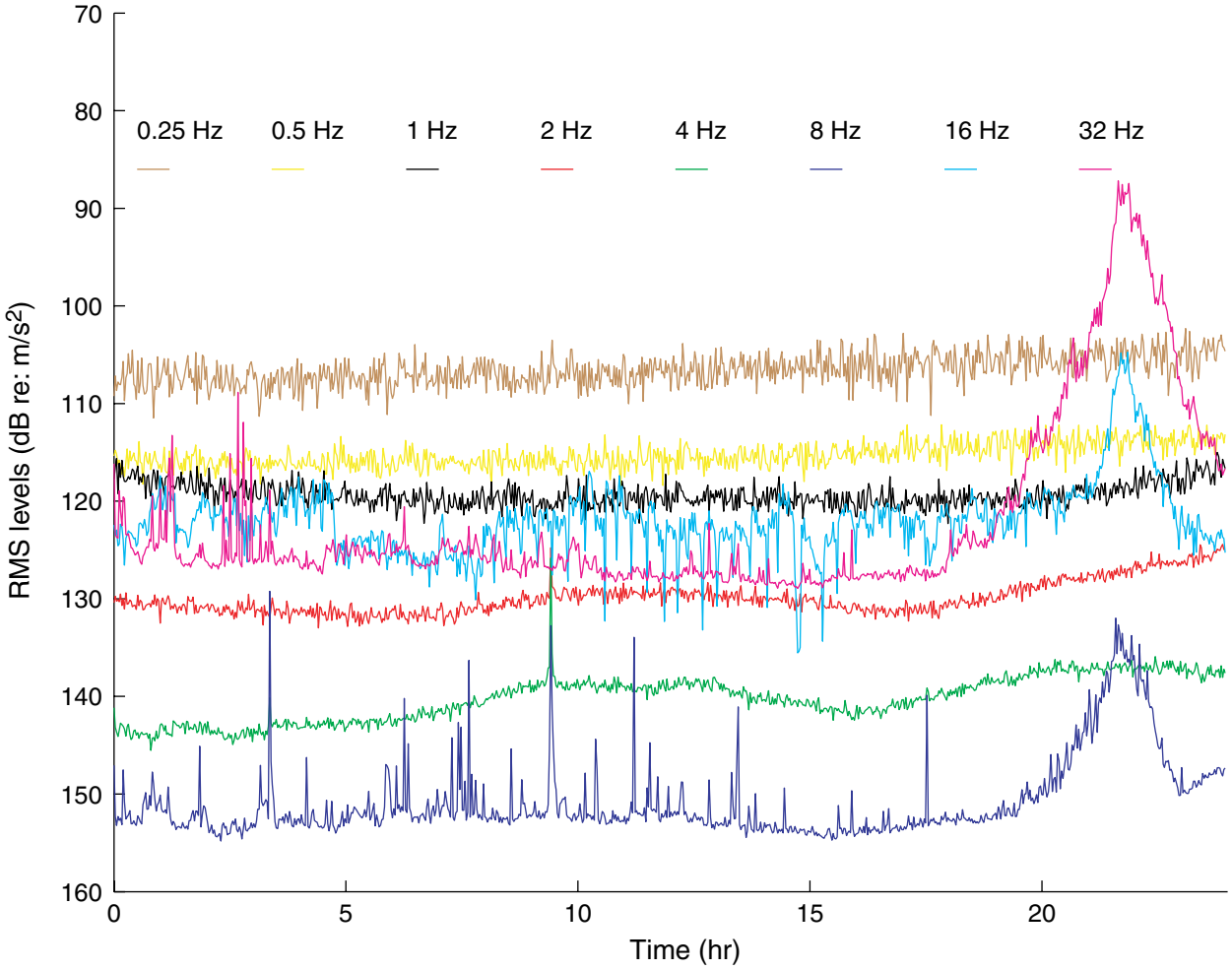

**Figure F54.** RMS energy levels in octave bands centered at the frequencies indicated for day 27 in 2002.

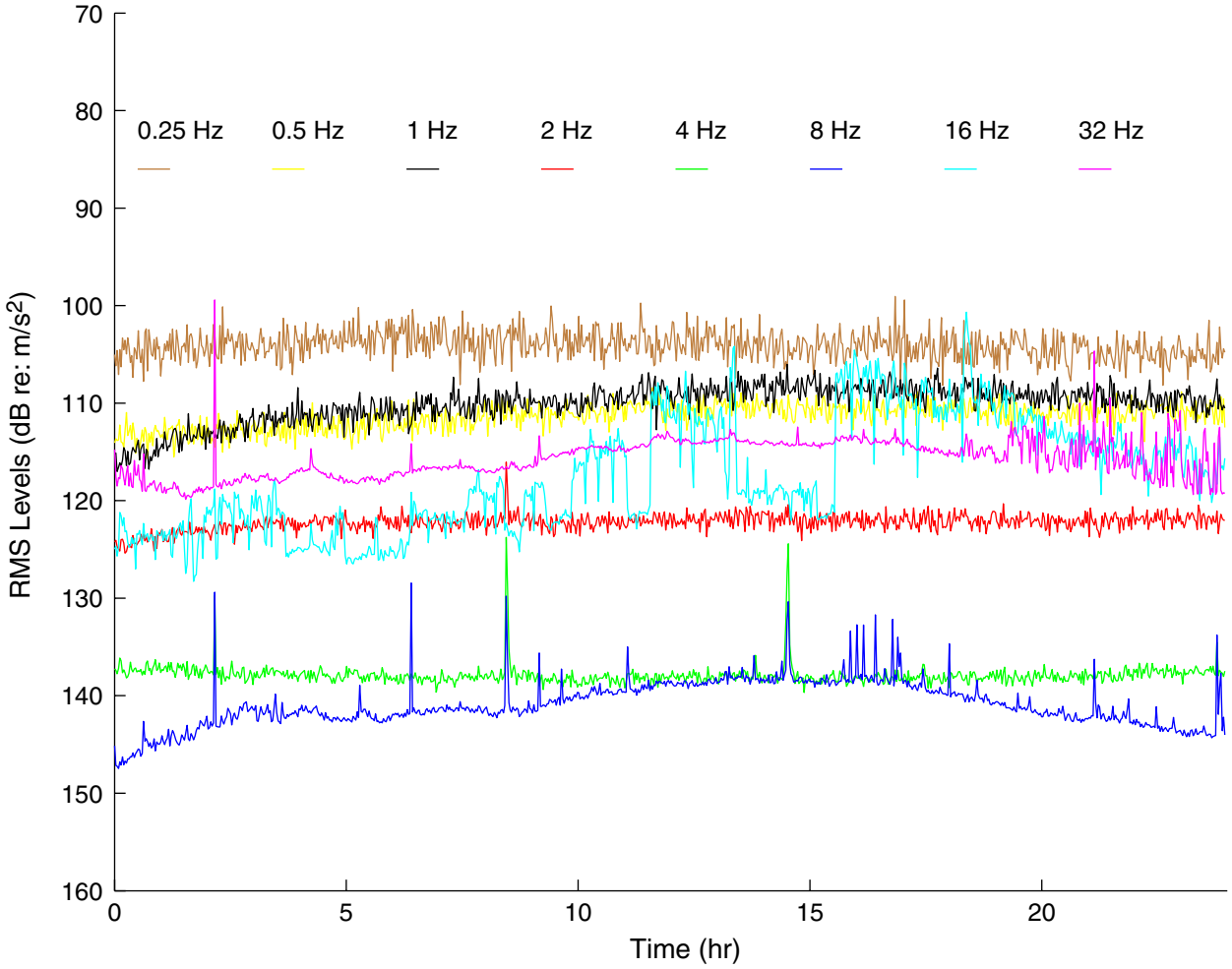

**Table T1.** Summary of channel identifiers for H2O seismic data (160 sps).

| Identifier | Sensor | Gain | Channel |
|---|---|---|---|
| HHZ | Guralp | High | Vertical |
| HH1 | Guralp | High | Horizontal 1 |
| HH2 | Guralp | High | Horizontal 2 |
| HLZ | Guralp | Low | Vertical |
| HL1 | Guralp | Low | Horizontal 1 |
| HL2 | Guralp | Low | Horizontal 2 |
| EHZ | Geophone | High | Vertical |
| EH1 | Geophone | High | Horizontal 1 |
| EH2 | Geophone | High | Horizontal 2 |
| ELZ | Geophone | Low | Vertical |
| EL1 | Geophone | Low | Horizontal 1 |
| EL2 | Geophone | Low | Horizontal 2 |